THE ELECTRON EMISSION CHARACTERISTICS OF ALUMINUM, MOLYBDENUM AND CARBON NANOTUBES STUDIED BY FIELD EMISSION AND PHOTOEMISSION

Edward Delarosa Sosa, B.A., B.S

Dissertation Prepared for the Degree of

DOCTOR OF PHILOSHOPY

UNIVERSITY OF NORTH TEXAS

December 2002

APPROVED:

David E Golden, Major Professor
Jeffry Kelber, Minor Professor
Bruce Gnade, Chair of the Department of Materials Science
Richard F Reidy III, Committee Member
Witold Brostow, Committee Member
C. Neal Tate, Dean of the Robert B Toulouse School of Graduate Studies

Sosa, Edward Delarosa, The Electron Emission Characteristics of Aluminum, Molybdenum and Carbon Nanotudes Studied by Field Emission and Photoemission. Doctor of Philosophy (Materials Science), December 2002, 147 pp., 9 tables, 56 illustrations, 88 references and titles.

The electron emission characteristics of aluminum, molybdenum and carbon nanotubes were studied. The experiments were setup to study the emission behavior as a function of temperature and exposure to oxygen. Changes in the surface work function as a result of thermal annealing were monitored with low energy ultra-violet photoelectron spectroscopy for flat samples while field emission energy distributions were used on tip samples. The change in the field emission from fabricated single tips exposed to oxygen while in operation was measured using simultaneous Fowler-Nordheim plots and electron energy distributions. From the results a mechanism for the degradation in the emission was concluded.

Thermal experiments on molybdenum and aluminum showed that these two materials can be reduced at elevated temperatures, while carbon nanotubes on the other hand show effects of oxidation. To purely reduce molybdenum a temperature in excess of 750 ºC is required. This temperature exceeds that allowed by current display device technology. Aluminum on the other hand shows reduction at a much lower temperature of at least 125 ºC; however, its extreme reactivity towards oxygen containing species produces re-oxidation. It is believed that this reduction is due to the outward diffusion of aluminum atoms through the oxide. Carbon nanotubes on the other hand show signs of

oxidation as they are heated above 700 ºC. In this case the elevated temperatures cause the opening of the end caps allowing the uptake of water.

Oxygen exposure experiments indicate that degradation in field emission is two-fold and is ultimately dependent on the emission current at which the tip is operated. At low emission currents the degradation is exclusively due to oxidation. At high emission currents ion bombardment results in the degradation of the emitter. In between the two extremes, molybdenum tips are capable of stable emission.

ACKNOWLEDGEMENTS

This work was supported by Motorola Flat Panel Display Division and the National Science Foundation through Grant No: DMR-905187.

I would like to thank Dr. David Golden for all his guidance and support throughout the course of my graduate studies. To Dr. Ikerionwu Akwani, Dr. John Bernhard, Dr. Ambrosio Rouse and Dr. Patrick Abbott, thank you for your friendships and useful discussions which assisted in the progression of this research. I would like to thank Dr. Babu Chalamala for providing an internship at the Motorola Flat Panel Display Division where a large knowledge of device issues was obtained. I would also like to thank Bobby Turner and Edward Walter for their exceptional machining of many of the components necessary in this research. Finally I would like to thank my parents and family for all their love and encouragement throughout my education.

TABLE OF CONTENTS

Page

LIST OF TABLES

Page

LIST OF ILLUSTRATIONS

Page

CHAPTER 1

INTRODUCTION

1.1 Issues

Field emission arrays (FEAs) have invoked large interest due to their prospective uses from high speed radio frequency devices to field emission flat panel displays [1,2]. The Spindt deposition process has enabled the production of molybdenum-based field emission arrays made with micron sized field emitters [3]. Figure 1 shows the arrangement and fabrication of a Spindt type field emission array [3]. The issue confronting emission devices is the stability of the emitting surface. Field emission is directly affected by both changes in the composition and structure of the emitting surface; therefore, oxidation and ion bombardment can be a major detriment to a field emitter. For these reasons people have investigated various emitter materials ranging from metals to semiconductors [4,5,6,7]. To try and understand the mechanism by which degradation occurs, emission from different materials in the presence of an oxidizing species would be of value. Furthermore, to ascertain an even better understanding of the degradation mechanism, simultaneous energy distributions of the emitted electrons and current voltage characteristics of emission while under the exposure of an oxidizing species would need to be acquired.

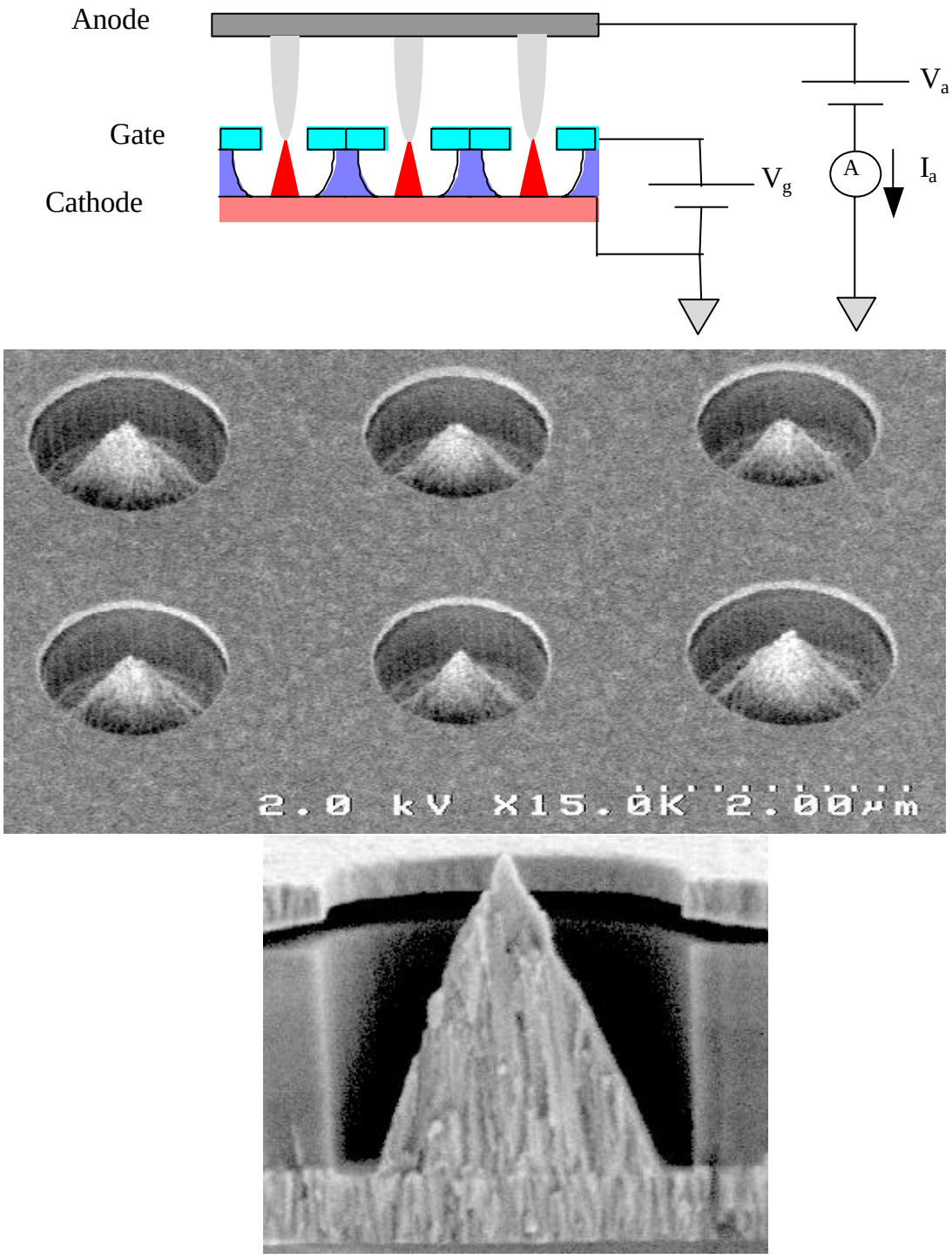

Figure 1.1 Electrical schematic and scanning electron micrographs of a Spindt type molybdenum field emission array.

1.2 Field Emitter Materials and their Properties

The ideal field emitting material should have good electrical, mechanical and chemical properties. The desired electrical properties would be high conduction and low work function. From the mechanical point, an emitter candidate would require high toughness and strength, so as to resist ion bombardment. As for the chemical properties of an emitter, the main criteria is resiliency to oxidation. Most metals meet the first two criteria; however, are susceptible to oxidation. To try to overcome these issues many researchers have investigated various metals and their carbon and oxygen complexes. The addition of carbon to various elements is known to increase the mechanical properties of materials (i.e. Fe and Si). For this reason, many have studied the emission properties of transition metal carbides [5,8]. It has also been observed that some metal carbides have drastically lower work functions than the parent metal [8]. The emission from metal oxides has also been investigated [9,10]. Here the objective is to have the oxide already present so that chemical interaction with any oxygen containing species is eliminated. Unfortunately neither of these two schemes has produced an effective FEA.

Molybdenum (Mo) has been the most commonly studied field emitting material. Its high melting point, high strength and low resistivity make it an ideal material. Molybdenum has a moderate work function of 4.6 eV. Furthermore, its deposition is easily achieved using standard semiconductor technology. The deposition of Mo has been accomplished with a high aspect ratio (ratio of base width to tip height) [11]. Unfortunately, Mo is known to oxidize readily in the presence of oxygen forming MoO_2 and MoO_3 [12,13,14]. Oxidation of Mo tips has been shown to be responsible for the

instability in Mo FEAs [15]. Therefore, in order for Mo to be used as a field emission material its oxidation must be limited, if not prevented

Carbon nanotubes have a unique geometry that makes them a favorable field emitting material. Their tubular structure provides a tip radius on the nanometer scale, which is far less than the average radius of a Spindt type Mo tip. This extreme sharpness will result in local field enhancement, thus a lower extracting voltage is to be expected. In addition to the extreme sharpness of nanotubes, the work function may also enhance the emission properties. Several groups have reported a wide range of values [16,17,18,19] for the work function of carbon nanotubes. These values were determined by field emission, X-ray photoelectron spectroscopy and ultraviolet photoelectron spectroscopy experiments. These reported work functions vary depending on whether the nanotubes are multi-walled (MWNT) or single-walled nanotubes (SWNT). The range of work function values for these nanotubes is large (from 1.3-8.2 eV). Moreover, in addition to their electrical properties, nanotubes also have good mechanical strength as well as chemical inertness. With all these properties taken into consideration carbon nanotubes could be a great emitter.

Aluminum is the most abundant metal in the earth's crust. It has a low melting point (660 ^{o}C) which makes it relatively easy to deposit by evaporation methods. The work function of polycrystalline aluminum is reported as 4.2 eV [20]. It oxidizes readily when exposed to oxygen; however, its oxide forms a self protective barrier which is usually about 30 Å in thickness. Although pure aluminum is very ductile, its oxide, alumina (Al_2O_3), is very hard. Oxidation of clean aluminum has been reported to lower

the work function below that of the clean metal [21,22,23,24]. The combination of greater hardness and lower work function would make aluminum well suited for field emission.

Physical Properties	**Aluminum**	**Carbon Nanotubes**	**Molybdenum**
Melting Point	660.45 °C	3802 °C	2623 °C
Crystal Structure	FCC	HCP	BCC
Electrical Resistance	2.709 μΩ·cm	5.1-8x10^{5}μΩ·cm(MW)[25] 30-100 μΩ·cm (SW)[26]	5.47 μΩ·cm
Work Function	4.28 eV	1.3-8.2 eV	4.6 eV
Tensile Strength		11-63 GPa	
Hardness (Knoop)	2-2.9		
Thermal Conductvity	2.37 W·cm$^-$1·K^{-1}	0.35-2.0 W·cm·K	1.38 W·cm^{-1}·K^{-1}
Common Oxides	Al_2O,Al_20_3, $Al(OH)_3$	CO, CO_2	MoO_2, MoO_3
ΔH_f^0 (oxide)	Al_2O(g) = -130 kJ/mol Al_2O_3 = -1675.7 kJ/mol	CO(g) = -110.525 kJ/mol CO_2(g) = -393.51 kJ/mol	MoO_2 = -588.9 kJ/mol MoO_3 = -745.1 kJ/mol
ΔG_f^0 (oxide)	Al_2O(g) = -159 kJ/mol Al_2O_3 = -1582.3 kJ/mol	CO(g) = -137.168 kJ/mol CO_2(g) = -394.36 kJ/mol	MoO_2 = -533 kJ/mol MoO_3 = -668 kJ/mol

Table1.1 Physical properties of Aluminum, Carbon Nanotubes and Molybdenum. Values obtained from the handbook of Chemistry and Physics.

1.3 Measurement of Surface Modification

Since field emission is a dynamic process that is strongly dependent on surface conditions, both chemical and structural modifications need to be closely monitored. In Fowler-Nordheim theory [27] of field emission from metals, the plot of ln (I/V^2) vs 1/V,

where I is emission current and V is the extracting voltage, gives a straight line. This type of plot is commonly known as a Fowler-Nordheim (FN) plot. The slope of this line is proportional to $b\Phi^{3/2}$, where b is a geometric parameter of tip sharpness and Φ is the surface work function. A change in the slope of the line thus indicate a change in one or both of these parameters. From this point of view, ion bombardment will affect the geometrical parameter, b, whereas, surface contamination will affect Φ. In order to determine the contribution of these two parameters to the emission stability, they must be independently measured.

Any chemical or physical interaction with the field emitter tip can drastically change the emission characteristics. By measuring the current-voltage characteristics and the energy distribution of field emitted electrons simultaneously, the factor responsible for emission degradation can be ascertained. The field emission energy distributions (FEED) can be used to directly monitor changes in the work function. In turn, the change in the work function can be attributed to any change in the slope of the Fowler-Nordheim plot. Furthermore, if the work function does not vary, but the FN slope does this would be a direct indication that modification of the tip geometry is taking place. Unfortunately, FEED does not give direct insight as to the chemical composition of the surface. So to identify the chemical species responsible for a change in the work function, some other technique must be employed.

X-ray photoelectron spectroscopy is a surface sensitive technique which can be used to detect monolayer coverage of contaminants. Each element in the periodic table has a unique set of electron energy levels, which act as a fingerprint. By measuring the

energy required to liberate an electron (binding energy) from any of these levels, elemental identification is possible. The surrounding environment has a pronounced affect on the electron energy levels of an atom, thereby causing a shift in the binding energy. This chemical shift can be used to identify the chemical makeup of a surface. Thus compounds of different stoichiometry will display different binding energies, which allows for chemical characterization. This tool provides the means for monitoring the chemical reactions at the tip surface.

Once the chemical species present is known, the work function of the species can be obtained by photoemission . Here low energy photons are used to eject electrons from the valence band (ultra-violet photoelectron spectroscopy, UPS). Ultra-violet (UV) photons are of sufficient energy to produce valence band emission. By using a monochromatic source of UV photons, the work function can be obtained through the Einstein photoelectric equation:

$$KE = h\nu - \Phi \qquad \text{eq. 1.1}$$

where KE is the kinetic energy of the photoelectron, $h\nu$ is the energy of the incident photon and ϕ is the work function. The kinetic energy of the electrons can be directly measured using an energy analyzer. UV photons can be provided using a mercury (Hg) discharge lamp or an argon (Ar) ion laser. Photons from the discharge lamp can be passed through a monochromator to isolate photons of particular energy. Frequency doubling of the fundamental line in the Ar laser can produce a monochromatic beam of photons with 5.41 eV energy. Both sources provide photons with sufficient energy to produce valence band photoemission from most metals. Once the work function of a

species can be identified by UPS, characterization of FEED curves can be achieved since both provide a measure of the surface work function.

1.4 Purpose of Investigation

To better understand the mechanism involved in field emission instability, a precise observation of the surface is required. The intention is to monitor the work function of the surface and the tip shape when a field emitter is operated in an oxygen ambient. This will be done by simultaneously measuring the current voltage characteristics and the energy distribution of field emitted electrons from a clean and oxidized surface. Furthermore, to determine the affects of operating conditions these experiments will be preformed with various emission currents. The materials to be studied are aluminum, carbon nanotubes and molybdenum.

References:

1. C.A. Spindt and I. Brodie, Adv. Electron. Electron Phys. **83**, 1, (1992).
2. I. Brodie and P.R. Schwoebel, Proc. IEEE **82**, 1006 (1992).
3. C.A. Spindt, J. Appl. Phys. **39**, 3504 (1968).
4. L. Richter and R. Gomer, Surf. Sci. **83**, 93 (1979).
5. W.A. Mackie, R.L. Hartman, M.A. Anderson and P.R. Davis, J. Vac. Sci. Technol. B **12**(2), 722 (1994).
6. S. Meassick and H. Champaign, J. Vac. Sci. Technol. B **14**(3), 1914 (1996).
7. G.L. Kellogg, Colloque de Physique **C8** 297 (1989).

8. A.A Rouse, J.M. Bernhard, E.D. Sosa and D.E. Golden, Appl. Phys. Lett. **76**, 2583 (2000).
9. J.M. Bernhard, A.A. Rouse, E.D. Sosa, B.E. Gnade, D.E. Golden, B.R. Chalamala, S. Aggarwal and R. Ramesh, Flat Planel Display and Sensors- Principles, Materials and Processes Symposium (MRS Symposium Proceedings) vol. 588, pp. 85 (2000).
10. Y.J. Yoon, D.S. Yoon, H.K. Baik, S.M. Lee, K.M. Song and S.J. Lee, J. Vac. Sci. Technol. B **18**(2), 972 (2000).
11. S. Itoh, T. Watanabe, K. Ohtsu, M. Taniguchi, S. Uzawa, J. Vac. Sci. Tech. B **13**, 487 (1995).
12. H.M. Kennett and A.E. Lee, Surf. Sci. **48**, 591 (1975).
13. E. Bauer and H. Poppa, Surf. Sci. **88**, 31 (1979).
14. S.I. Castañeda, I. Montero, J.M. Ripalda, N. Díaz, L. Galán and F. Rueda, J. Appl. Phys. **85**(12), 8415 (1999).
15. B.R. Chalamala, R.M. Wallace, B.E. Gnade, J.Vac. Sci. Technol. B, **16** (5), 2859 (1998).
16. P.G. Collins and A. Zettl, Phys. Rev. B **55**(15), 9391 (1997).
17. Yu.V. Gulyaev, N.I. Sinitsyn, G.V. Torgashov, Sh.T. Mevlyut, A.I.Zhbanov, Yu.F. Zakharchenko, Z.Ya. Kosakovskaya, L.A. Chernozatonskii, O.E. Glukhova and I.G. Torgashov, J. Vac. Sci. Technol. B **15**(2), 422 (1996).
18. H. Ago, Th. Kugler, F. Cacialli, K. Petritsch, R.H. Friend, W.R. Salaneck, Y. Ono, T.Yamabe and K. Tanaka, Synthetic Metals **103**, 2494 (1999).

19. O. Gröning, O.M. Küttel, Ch. Emmenegger, P. Gröning and L. Schlapbach, J. Vac. Sci. Technol. B **18**(2), 665 (2000).

20. Handbook of Chemistry and Physics, 73rd edition, CRC Press Inc., 2000 Corporate Blvd., N.W., Boca Raton, FL 33431.

21. T. Fort Jr. and R.L. Wells, Surf. Sci. **32**, 543 (1972).

22. V.K. Agarwala and T. Fort Jr., Surf. Sci. **45**, 470 (1974).

23. V.K. Agarwala and T. Fort Jr., Surf. Sci. **48**, 527 (1975).

24. P. Vinet, Nasa Technical Memorandum, **87079** (1985).

25. T.W. Ebbesen, H.J. Lezec, H. Hiura, J.W. Bennett, H.F. Ghaemi and T. Thio, Nature **382**, 54 (1996).

26. J.E. Fischer, H. Dai, A. Thess, R. Lee, N.M. Hanjani, D.L. Dehaas and R.E. Smalley, Phys. Rev. B **55**, R4921 (1997).

27. R.H. Fowler and L.W. Nordheim, Proc. Roy. Soc. London **A119**, 173 (1928).

CHAPTER 2

THEORY OF FIELD AND PHOTOEMISSION

2.1 Introduction

As stated in the previous chapter both compositional and structural changes can influence the stability of the field emission current. Compositional changes can include the formation of an oxide or adsorption of molecules, which can affect the surface work function as well as the conductivity. The major structural effects are the reduction in emitter tip sharpness or emitting sites due to ion bombardment. Ultra high vacuum conditions have been shown to increase FEAs lifetimes by three orders of magnitude [1]. However, in display packaging this condition is not possible due to device outgassing. Under poor vacuum conditions both ion sputtering and oxidation of the tip are likely to occur, thereby, producing decreased or unstable emission currents. In order to develop a clear picture of what is taking place at the emitter surface, a concise understanding of the theory of field emission is essential. In this chapter an overview of the theory of field and photoemission will be presented

2.2 Theory of Field Emission

Field emission is the tunneling of electrons from the valence band of a metal surface into vacuum, under the application of a high electric field. To develop the theory of field emission, we first consider the metal surface in the absence of an electric field.

Inside the metal an electron sees a constant potential in accord with the free electron theory of metals. At 0K, an energy which is equal to the work function must be supplied for an electron to escape into the vacuum level. When the electron leaves the metal, it will leave behind an induced positive charge in the metal. From classical electrostatics this electron will experience an attractive force due to this induced positive charge, known as the image force. On the vacuum side of the metal-vacuum interface the potential energy of the electron will be given by:

$$V(x) = E_F + \Phi - e^2/4x \qquad \text{(eq. 2.1)}$$

where E_F is the Fermi energy of the electron in the metal, Φ is the work function and $-e^2/4x$ is the image force [2]. When an electric field is applied, the potential is further reduced by an amount $-eF_ox$, thus the potential becomes:

$$V(x) = E_F + \Phi - e^2/4x - eF_ox \qquad x > x_c \qquad \text{(eq.2.2)}$$

$$V(x) = 0 \qquad x < x_c$$

where x_c is the distance from the cathode to the bottom of the conduction band and is equal to $3.6/(E_F+\Phi)$. Therefore the presence of an electric field reduces the barrier width by an amount $-eF_ox$ which facilitates tunneling, as can be seen in figure 2.1.

2.3 Fowler-Nordheim Equation of Field Emission

Here we will construct a simplified equation describing the electron emission from a metal surface. The number of electrons impinging on the surface barrier with normal energy between W and W + dW is given by

$$N(W,T)dW = \left(\frac{mdW}{2p^2\hbar^3}\right)\int_W^\infty f(E)dE$$

$$= (mk_B T/2\pi^2 \hbar^3)\ln[1 + \exp(-W\text{-}E_F/k_B T)]dW \qquad \text{(eq 2.3)}$$

where m is the mass of the electron, k_B is the Boltzman constant, $\hbar$ is Plank's constant, W is the energy of electrons normal to the surface, E_F is the Fermi energy and T the temperature.There is a certain probability D(W) that the electrons impinging on the surface will be transmitted through the surface potential barrier. The current density, number of electrons emitted per unit area per unit time, is given by:

$$J(F,T) = e\int_0^\infty N(W,T)D(W)dW \qquad \text{(eq. 2.4)}$$

where T is temperature and F is applied field. The general expression for the emitted current density is:

$$J(F,T) = e\int_0^\infty N(W,T)D(W,F)dW$$

$$= \frac{emk_B T}{2\hbar^3 p^2}\{\int_0^{w_1} \frac{\ln\{1+\exp[-W - E_F)/k_B T\}dW}{1+\exp[Q(W)]}$$

$$+ \int_{w_1}^\infty \ln[1+\exp(-W - E_F)/k_B T]dW\ \} \qquad \text{(eq. 2.6)}$$

using the fact that D(W,F) is the transmission coefficient for the potential barrier and is equal to $\{1+\exp[Q(W)]\}^{-1}$, and N(W,T) is given by equation 2.3. At sufficiently low temperatures the term N(W,T) diminishes rapidly for $W>E_F$ and the calculated D(W,F) terms diminishes rapidly for $W<E_F$. Under these conditions the second integral becomes negligible and the first integral vanishes except in the vicinity of Fermi level [3]. After evaluation, the resultant expression becomes:

$$J(F,T) = \frac{e^3F^2}{16p^2\hbar\Phi t^2(y_\circ)} \frac{pc_\circ k_B T}{\sin(pc_\circ k_B T)} \exp\left[-\frac{4}{3e}\left(\frac{2m}{\hbar^2}\right)^{1/2} n(y_\circ)\frac{\Phi^{3/2}}{F}\right] \qquad \text{(eq. 2.7)}$$

where $t(y_o)$ and $v(y_o)$ are the Nordheim elliptic functions, Φ is the work function and F is the applied field. At very low temperatures $\pi C_o k_B T << 1$ eq. 2.7 reduces to

$$J(F) = \frac{1.537 \times 10^{10} F^2}{\Phi t^2(3.79F^{1/2}/\Phi)} \exp\left[(-0.683\Phi^{3/2}/F)v(3.79F^{1/2}/\Phi)\right] \ A/cm^2$$

$$= A'F^2 \exp\left[-B\Phi^{3/2}/F\right] \qquad \text{(eq. 2.8)}$$

which is the well known Fowler-Nordheim equation of field emission [3].

2.4 Fowler-Nordheim Plot

In order to extract some physical information from the above equation, it must be expressed in terms of measurable quantities. Since by definition the current density is expressed as current per unit area, and the field (F) can be expressed in terms of the applied voltage (V) and a geometrical factor (β) which is defined as the field enhancement factor, the above equation can be simplified. Thus substituting the following equations

$$I = JA \qquad \text{(eq. 2.9)}$$

$$F = \beta V \qquad \text{(eq. 2.10)}$$

Eq. 2.8 can be simplified as

$$I = aV^2\exp(-b\Phi^{3/2}/V) \qquad \text{(eq. 2.11)}$$

where a and b are, for practical purposes, constants [4]. By dividing both sides by V^2 and taking the logarithm of both sides, equation 2.11 can be written as

$$\ln(I/V^2) = \ln a - b\Phi^{3/2}/V \qquad \text{(eq.2.12)}$$

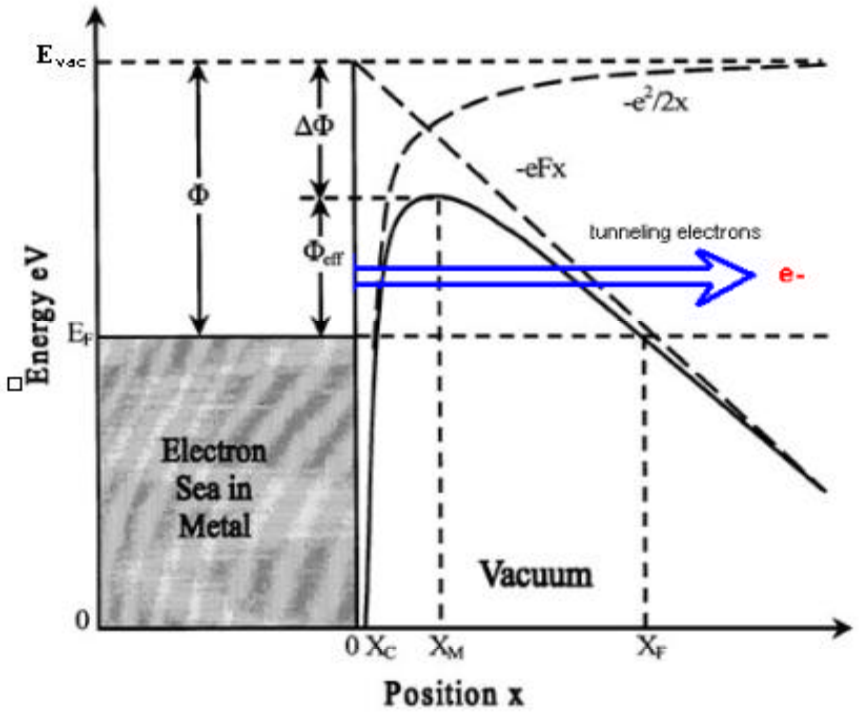

Figure 2.1 Potential energy diagram of electrons tunneling from a metal surface under the application of an electrical field. Here E_F is the Fermi level and E_{vac} is the energy of the vacuum level.

which has the form of the equation of a line. If one plots ln (I/V^2) versus 1/V, one gets a straight line whose slope is $-b\Phi^{3/2}$, and intercept is ln a. This type of plot is known as a Fowler-Nordheim plot. A change in the slope of the line indicates either a change in the work function or in the geometry of the tip. In this manner, it can be seen that the change in the work function or shape of the tip cannot be independently isolated. However, by simultaneously measuring the current-voltage characteristic and the total energy distributions of emitted electrons, these two quantities can be isolated.

2.5 Total Energy Distributions

Unlike measuring the total current, a total energy distribution (TED) contains more information related to the inherent properties of the emitter, as well as, to the basic tunneling process [5]. Henderson and coworkers were the first to actually measure the energy distributions of field emitted electrons showing that these electrons do originate near the Fermi level [6]. Their use of a retarding potential analyzer produced half-widths in the energy distribution that were too large. Müller and Young re-measured the energy distributions using a spherical retarding potential analyzer and obtained widths one-third as wide [7]. Using a free electron gas model,Young [8] was able to derive a theoretical interpretation of the total energy distribution of field emitted electrons, which was in very good agreement with experimental observations.

The TED is the product of the transmission probability factor and the Fermi-Dirac distribution function. An elaborate derivation for the emitted electron density will not be given here, but is derived from eq. 2.4. The net result is that the energy dependence of the total energy distribution , J(E), is given by

$$J(E) = \frac{BF}{\Phi^{1/2} t(w)} \exp\left(\frac{E - E_F}{d}\right) \frac{1}{1 + \exp[(E - E_F)/k_B T]} \qquad \text{eq. 2.14}$$

with

$$B \approx 1.58 \times 10^{10} \exp\left[\frac{-6.85 \times 10^7 \, n(w) \Phi^{3/2}}{F}\right] \qquad \text{eq. 2.15}$$

and

$$\frac{1}{d} \approx 1.025 \, \frac{t(w) \Phi^{1/2}}{F} \qquad \text{eq. 2.16}$$

with all terms as defined in the previous section. The maximum in the energy distribution relative to E_F occurs for

$$E_{max} = -k_B T \ln\left(\frac{d}{k_B T} - 1\right) \qquad \text{eq. 2.17}$$

and the half-width at T = 0 K is given [2,8]by

$$\Delta E(0) = d \ln 2 \qquad \text{eq. 2.18}$$

The shape of the distribution curve of field emitted electrons is that of an exponentially modified Gaussian. The shape of the energy distribution is influenced by the sharply increasing transmission function and the sharply decreasing Fermi-Dirac function as the energy increases above E_F [9]. Several characteristics of TED's [2]should be pointed out . The high energy slope is mostly temperature dependent while the low energy slope is mostly field dependent. These are shown graphically in figures 2.2 and 2.3. At a temperature T* (the inversion temperature) = $d/2k_B$ the average number of field emitted electrons under E_F is equal to those coming from over the Fermi level and $E_{max} = E_F$. For $T<T^*$, most of the field emitted electrons are under E_F and $E_{max} < E_F$. For $T>T^*$

there are more electrons emitted with energy higher than E_F and the maximum in the energy distribution is over the Fermi level. Furthermore the leading edge of the TED is smeared out not only by thermal effects but by instrumental resolution as well [5]. Regardless of the shape of the energy curve, the inflection point defines the work function. Thus the energy curve can be used to monitor modifications to the tip surface due to contaminants.

Field emission energy distributions are an effective way to study the electronic states of individual atoms or molecules that are absorbed on the emitter surface. They can also be used for identifying the presence of surface states at energies near E_F [10,11]. Much work has been done on the effects of absorbed atoms as well as the effects of oxidation on the distribution of emitted electrons [5,12,13 14].

2.6 Photoemission

Photoemission from a solid surface is the ejection of an electron from the solid as a result of the interaction of a photon and an atom in the solid. This process, known as the photoelectric effect, was first described by Einstein [15]. In his description, if a photon with energy $h\nu$ interacts with an atom, an electron can be ejected from the atom with a specific kinetic energy (KE) defined by

$$KE = h\nu - \Phi \qquad \text{eq. 2.19}$$

where Φ (the work function) is the energy required to liberate the electron. From equation 2.19, it is evident that any electron whose binding energy is less than the energy of the photon can be ejected. These ejected electrons (photoelectrons) can originate from either inner core levels or the valence band. Since every atom has its unique set of

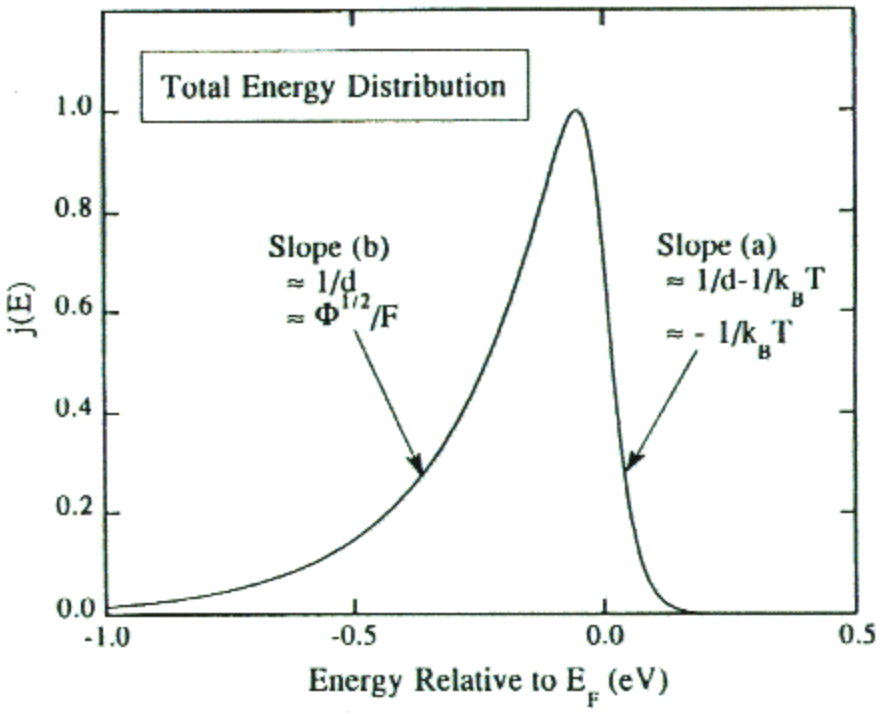

Figure 2.2 Plot of a total energy distribution depicting the field and temperature dependence on the slopes of the distribution (taken from reference 9).

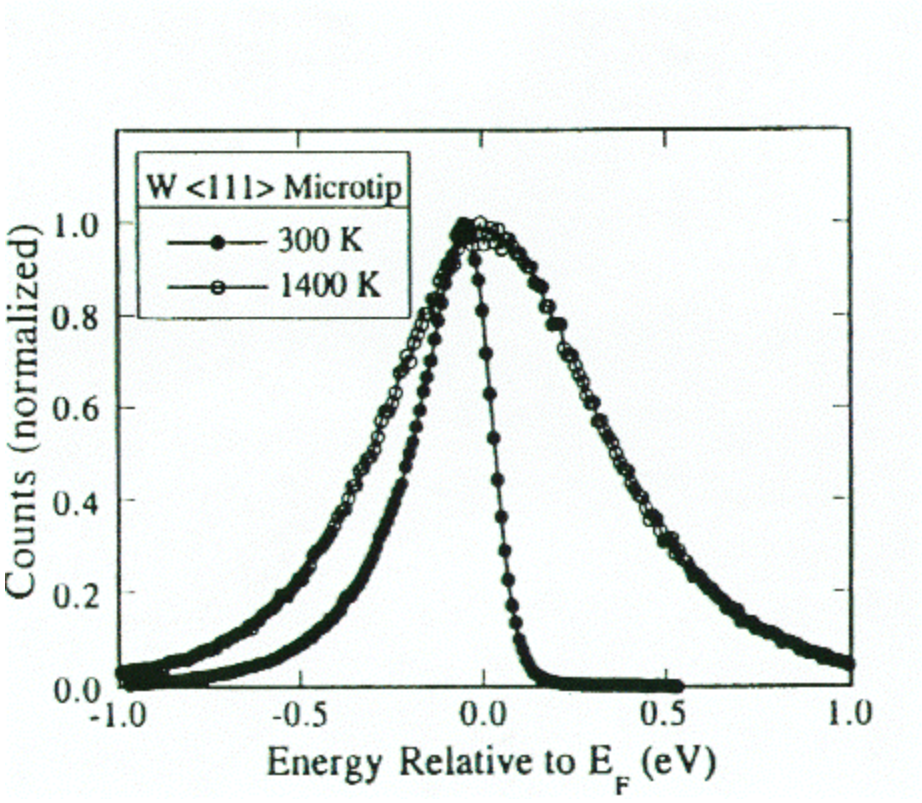

Figure 2.3 TED of a W microtip showing the increase in the energy spread with increasing temperature (taken from reference 9).

energy levels, photoemission can be used as a tool for elemental characterization.

Photoemission can be used to resolve features of the band structure as well as to examine contamination of the surface. To better understand how these types of information are observed in photoemission, band diagrams are helpful. Figure 2.4 shows the band diagrams of a metal and semiconductor. In solids the energy levels of individual atoms mix forming energy bands. The terms describing these energy bands are as follow. The highest occupied band is the valence band, where (E_V) is the maximum energy level of this band. The lowest unoccupied band is the conduction band, where (E_C) is the minimum energy level of this band. The separation between the valence and conduction band is the energy gap (E_g). The energy level of a free electron with zero kinetic energy is the vacuum level (E_{vac}). The Fermi level (E_F) is the energy of the least bound electrons in the solid at absolute zero temperature. The work function (ϕ) is the difference between the vacuum level and the Fermi level. Finally, the electron affinity (χ) is the separation between E_C and E_{vac}, and can have a positive or negative value depending on the position of the vacumm level relative to the conduction band minimum. All of these can influence the valence band photoemission spectra.

For a clean metal, the valence band maximum and the conduction band minimum coincide. The Fermi level for a clean metal is located at the top of the valence band. The work function for a clean metal then is merely a measure of the Fermi level relative to the vacuum level. The work functions of most materials fall in the range of 3-5 eV.

For semiconductors the term threshold energy is more commonly used. The threshold energy is the minimum photon energy required to excite an electron from the highest occupied energy level into the vacuum level. In semiconductors, the highest occupied level is the vacuum level, which is not necessarily the Fermi level as can be seen in figure 2.4. The threshold energy (E_T) is thus defined as:

$$E_T = \chi + E_g \qquad \text{eg. 2.21}$$

For a doped semiconductor, the Fermi level position can be near the valence edge for a p-type semiconductor and near the conduction edge for a n-type semiconductor. Whether it lies above or below depends on the degree of doping. In either case an additional term ξ must be added to the threshold energy.

$$E_T = \chi + E_g + \xi \qquad \text{eg. 2.22}$$

For heavily doped p-type semiconductors the Fermi level lies below the valence edge and ξ_p is positive, whereas, for heavily doped n-type semiconductors the Fermi level lies above the conduction edge and takes on a negative value. It is evident that the evaluation of the work function from photoemission is straight-forward for a metal or conductor in comparison to semiconductors, in which the width of the band gap and the degree of doping affect the photoemission characteristics.

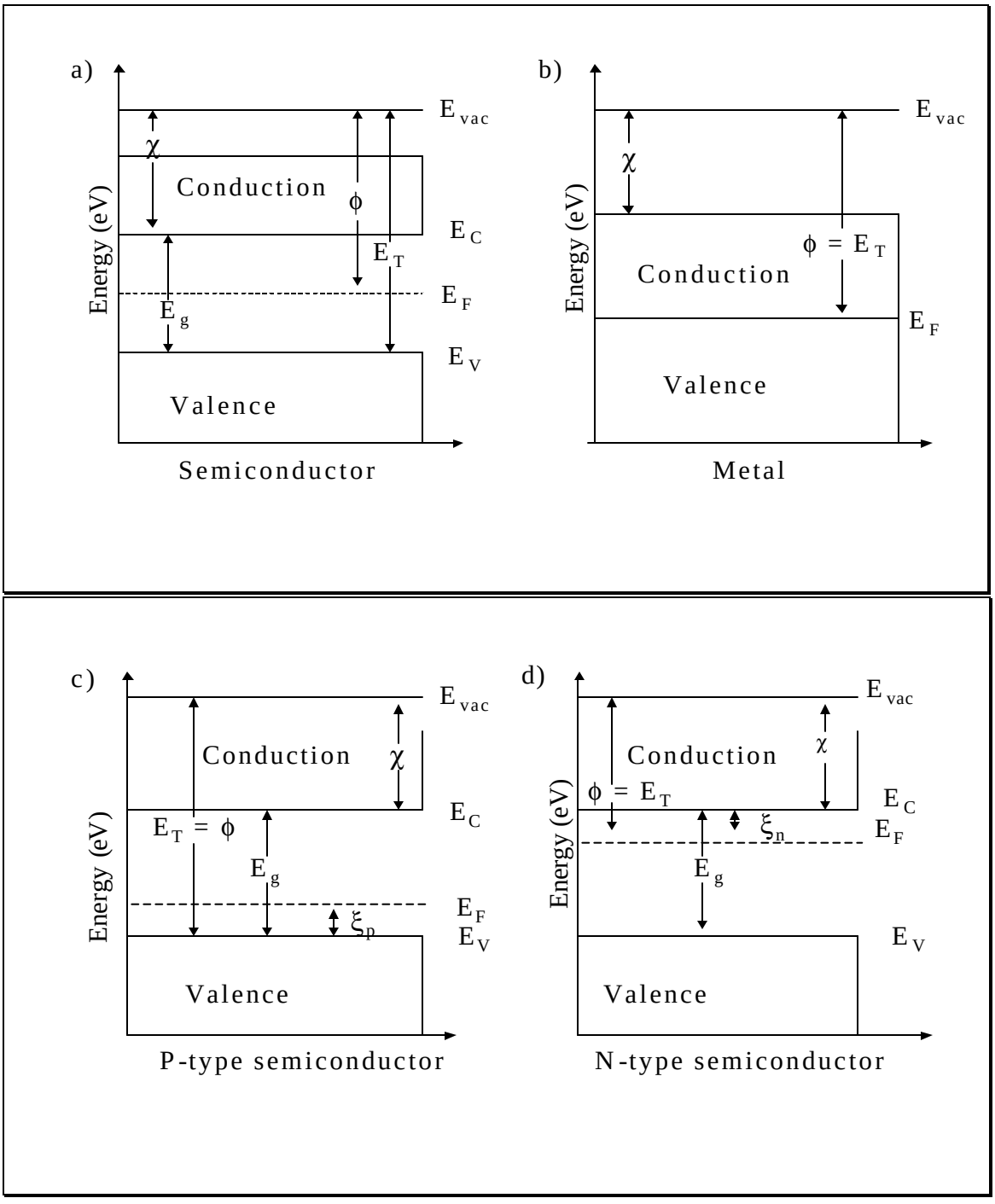

Figure 2.4 Energy band diagrams for a a) semiconductor, b)metal, c) p-type semiconductor and d) n-type semiconductor.

References:

1. B.R. Chalamala, R.M. Wallace and B.E. Gnade, J. Vac. Sci. Technol. B, **16**, 2866 (1998).
2. V. T. Binh, N. Garcia, S. T. Purcell, Advances in Imaging and Electron Physics, **95**, 74 (1996).
3. A. Modinos, *Field, Thermionic and Secondary Electron Emission Spectroscopy*, Plenum Press, New York, 1-18 (1984).
4. I. Brodie and R. Schwoebel, Proceeding of the IEEE, **82**, 1006 (1994).
5. J. W. Gadzuk and E.W. Plummer, Rev. Modern Phys. **45**, 487 (1973).
6. J.E Henderson and R.E. Badgley, Phys. Rev. **38**, 590 (1931).
7. R. D. Young and E. W. Müller, Phys. Rev. **113**, 115 (1959).
8. R. D. Young, Phys. Rev. **113**, 110 (1959).
9. S. Mogren and R. Reifenberger, Surf. Sci. **254**, 169 (1991).
10. L.W. Swanson, L.C. Crouser, Phys. Rev. Lett. **16**, 389 (1966).
11. E.W. Plummer, J.W. Gadzuk, Phys. Rev. Lett. **25**,1493 (1970).
12. E.W. Plummer and R.D. Young, Phys. Rev. B., **1**, 2088 (1970).
13. C. Lea and R. Gomer, J. Chem. Phys. **54**, 3349 (1971).
14. L. Richter and R. Gomer, Surf. Sci. **83**, 93 (1979).
15. A. Einstein, Annalen der Physik, **17**, 132 (1905).

CHAPTER 3

INSTRUMENTATION AND TECHNIQUES

3.1 Introduction

In this chapter a thorough description of the instrumentation used for the investigation of the emission characteristics of aluminum, molybdenum and carbon nanotubes will be presented. After fabrication of tips or flat samples, they were imaged under a scanning electron microscope (SEM). X-ray diffraction (XRD) was done on flat samples to determine the predominant crystal faces. The emission studies were done in two independent chambers. The first chamber was used to measure the field emission energy distributions (FEED) spectra and I-V curves from single tip emitters. The second chamber was used to measure the photoemitted electrons from both tips and flat samples. Both FEED spectra and photoemission spectra allowed the direct measurement of the work function for the materials in question.

Field emission experiments provided I-V curves and energy distributions. FEED spectra were obtained from single tips in a gated diode configuration. The distribution curves were obtained at a particular emission current of interest. The emitted electrons were focused and analyzed with a simulated spherical energy analyzer [1]. I-V curves were obtained by sweeping the extracting anode voltage while measuring the emission current at the tip. Emission experiments were conducted under oxygen exposure at

various emission currents. The resultant Fowler-Nordheim (FN) plots and energy distributions were then used to extract information on the emission behavior, i.e. change in work function or tip shape.

Photoemission experiments consisted of X-ray photoelectron spectroscopy (XPS) and ultra-violet photoelectron spectroscopy (UPS). XPS was used to characterize the chemical composition of the surface as a function of tip processing and thermal treatments. UPS was used to independently measure the work function as a function of absorbed species and thermal treatments. Both sets of spectra were obtained in a VG Scientific ESCA lab MK II photoelectron spectrometer (VG Scientific LTD, West Sussex, England, www.thermo.com). A dual Al-Mg anode was used as a source of X-rays with characteristic energies of 1486.6 (Al) and 1248.8 (Mg) for XPS. The excitation source for UPS was a Coherent Innova® 90C FreD™ Argon ion laser (Coherent Inc., Santa Clara, CA, www.cohr.com) equipped with a frequency doubling crystal. This laser can provide multiple single lines of emission. The possible lines that could be obtained are 488, 458, 351, 244 and 229nm. For this study the 229nm line was used, whose corresponding energy is 5.41eV, an energy sufficient to probe most work functions. XPS is thus used to monitor the chemical species present, and UPS determines the corresponding work functions, which in turn, can be used to corroborate field emission data.

In addition both chambers had the capability of thermal heat treatment. In the FEED chamber this was accomplished by passing current through a tungsten filament to which the emitter was spot welded. The resistive heating was monitored by a

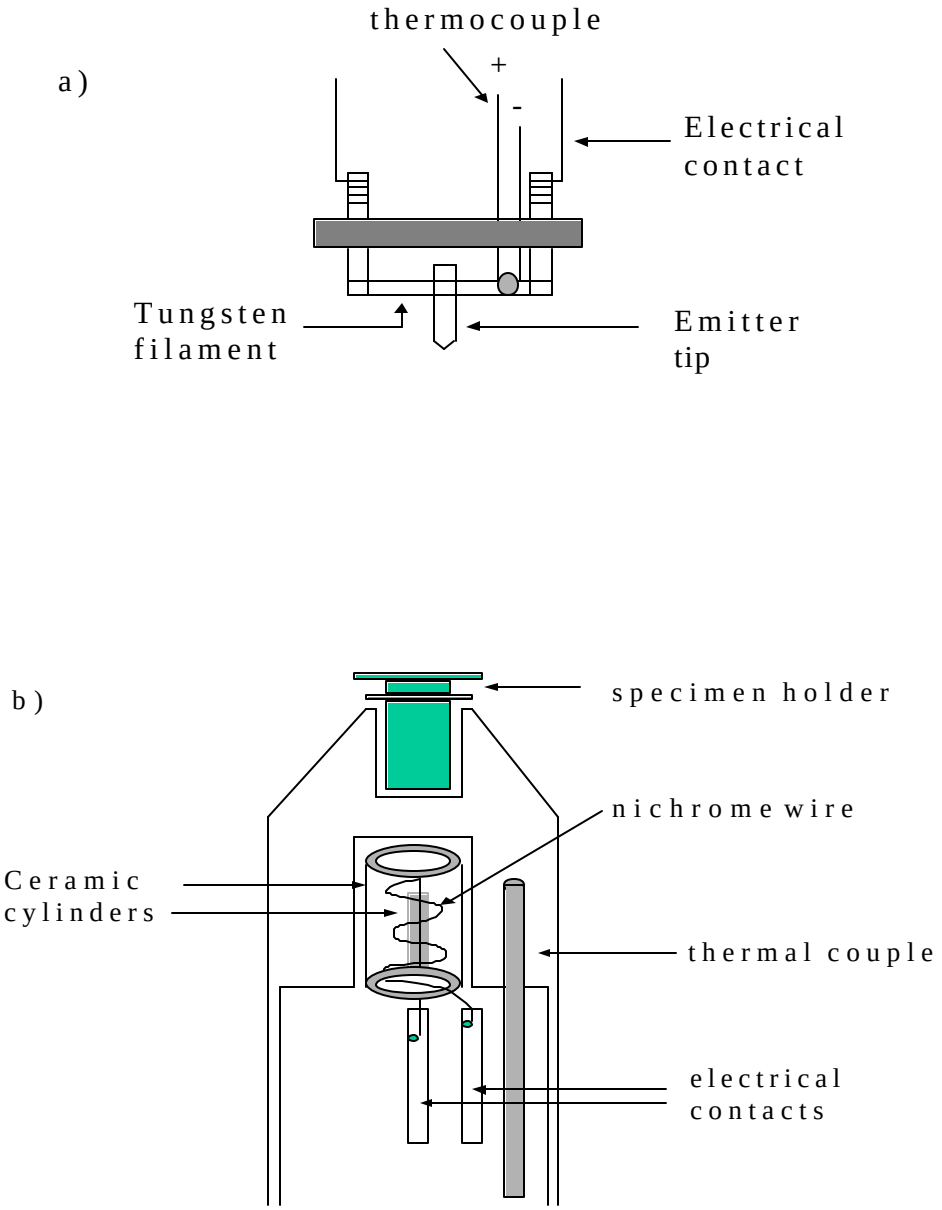

Figure 3.1 Diagram of the heating elements for the FEED and VG ESCA a) spot welded tip and thermocouple on a tungsten filament b) specimen heater probe.

Alumel/Chromel (NiCr/NiAl) type K thermal couple spot-welded onto the filament. The VG chamber consisted of a processing chamber located between the introduction chamber and the main analysis chamber. A gate valve is located on each side of thisprocessing chamber so as to isolate it from the other two chambers. The specimen heater probe is located in this processing chamber and has the ability to anneal the sample up to 900 °C. It consists of a stainless steel block in which the sample peg rests. The block is resistively heated via a nichrome wire. The probe contains an electronic thermometer which allows temperatures in the range –200 °C to +1200 °C to be measured with a Chromel/Alumel thermocouple [2]. Heating can provide a means of phase transformation and surface cleansing via desorption of gases, both of which are of interest in this study.

To monitor the gaseous species desorbed from the surface during heating both chambers had a residual gas analyzer (RGA) mounted onto them. The RGA and corresponding software was a commercially purchased RGA from Stanford Research Systems (Stanford Research Systems, Sunnyvale, CA, www.directindustry.com) [3]. The software allows various modes of operation. Only two of the modes were used in this research. In one mode the pressure is tracked as a function of the atomic mass of the gaseous species. In the other mode the pressure is monitored as a function of time for defined species. In this mode, the RGA allows continuos tracking of up to 10 species at any particular time. The first mode offers the advantage of detecting desorbed species when it is unknown what exactly will desorb from the sample. In either case, residual gas analysis allows the study of adsorption and desorption processes.

3.2 Sample Preparation

All flat samples were prepared on Mo foil. The Mo foil purchased from Alfa Aesar was of 99.95% purity (metal basis) and 0.1 mm (0.004 in) thick. The foils were cut into 1cm x 1cm pieces. Aluminum flat samples were made by tightly wrapping Al wire around the Mo foil. The Al wire used was also purchased from Alfa Aesar. The diameter of the wire was 0.5mm (0.02in) and was 99.9998% (metal basis). Nanotube samples were prepared by pressing SWNT mats onto the Mo sheet. Tubes were purchased from two sources. The first set were acquired from Materials and Electrochemical Research Corporation (MER corporation, Tuscon, AZ, www.mercorp.com) and the second set were acquired from Tubes at Rice (Carbon Nanotechnologies Inc., Houston, TX, www.cnanotech.com).

Emitter tips were fabricated either by chemical or electrochemical etching. Molybdenum tips were formed from Mo wire 0.5mm diameter (0.02in) and 99.98% (metal basis). Wire strips of 2-3" were cut and electrochemically etched in an 8% wt. NaOH aqueous solution. The Mo wire was positively biased with +10V, while –10V was applied to a stainless steal rod. After etching the tips were immersed in a HF solution to remove any oxide formed from the hydroxide solution. Aluminum tips were formed by chemical etching in a 25% HNO_3, 15% HF aqueous solution. Again tips were submerged in HF solution to remove any thick oxide formation. Nanotube tips were made by pressing the nanotubes onto a Mo tip. All tips were viewed under the SEM to examine coverage and sharpness.

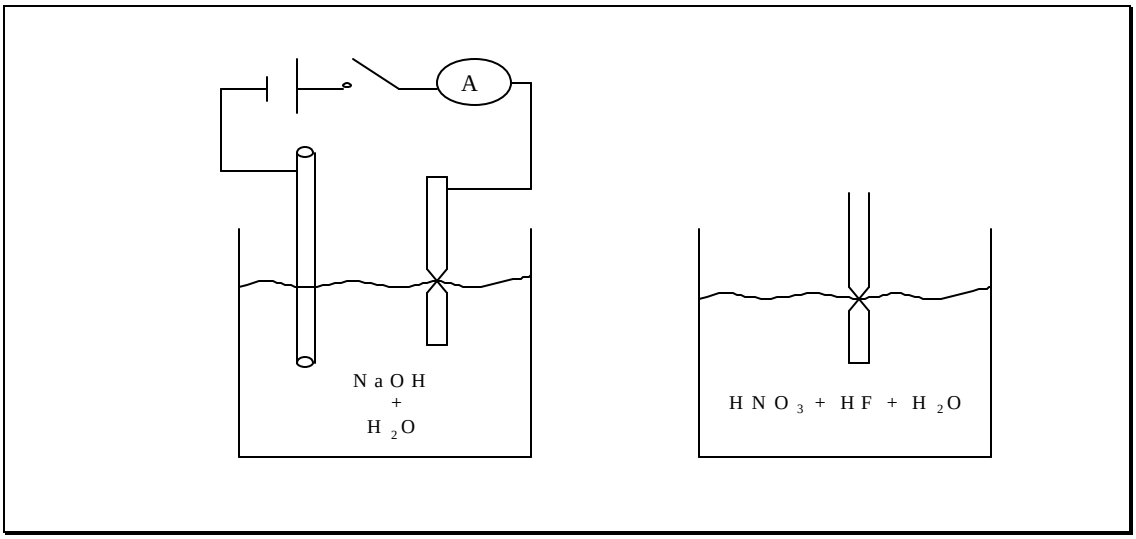

Figure 3.2 Apparatus for tip etching. Mo tips are electrochemically etched in a glass beaker containing a NaOH solution. Al tips are chemically etched in a plastic container containing an aqueous solution of nitric and hydrofluoric acids.

3.3 Scanning Electron Microscopy

In order to observe the degree of sharpness and coverage, a JEOL model JMS- T300 Scanning Electron Microscope (JEOL USA Inc., Peabody MA, www.jeol.com) was used. The microscope is composed of five parts: an electron source, a focusing column, a sample stage, a detector and an imaging control unit. The system is evacuated to an operating pressure of 10^{-4} Pa by a 420 L/sec oil diffusion pump containing a water-cooled baffle and a 100 L/min oil rotary pump. The electron source is a hairpin tungsten filament, which produces electrons by thermionic emission. A high voltage anode (5-25 kV) then accelerates these electrons into a dual section-focusing column composed of

magnetic lenses. The electrons are focused onto the sample stage with a diameter of less than a micron. The electrons incident on the sample produce a substantial amount of secondary electrons, which are collected at a positively biased detector. The detector is composed of a scintillator and a photomultiplier tube. The secondary electrons impinge on the scintillator producing photons which are proportional to the number of electrons striking the scintillator. The photons pass through a photomultplier tube generating an electrical signal proportional to the number of photons. The signal is received at the physical imaging unit containing two cathode ray tube (CRT) screens. One CRT screen is comprised of a long-lived phosphorescent screen used for direct viewing. The other CRT is comprised of a short-lived phosphorescent screen used for taking micrographs with Polaroid film. Images are obtained by varying the brightness, contrast and stigmation control knobs on the imaging unit.

Tips and flat samples were loaded onto a holder where they are held in place with conductive double-sided adhesive carbon tape. The system was vented to air and samples were loaded. After pumping down to the operating pressure the accelerating voltage was applied (15 or 20 kV for samples examined in this study). The filament current was increased to 0.4A, the current required to obtain an image. The brightness, contrast, magnifaction and stigmation were adjusted until a high quality image was achieved. Images were captured on Polaroid #55 film with exposure times of 60 and 90 seconds.

Figure 3.3 JEOL model JMS-T300 Scanning Electron Microscope. The microscope was used to inspect the quality of tip etching.

3.4. Photoelectron Spectroscopy

The experimental system used for photoelectron studies was a VG ESCA lab MKII spectrometer. The system is a commercial stainless steel ultra high vacuum chamber intended for surface analysis. The system is shown in figure 4 and consists of a three chamber apparatus. The first chamber, an introduction chamber, is isolated by a load lock valve and can be brought up to atmospheric pressure to introduce the sample. It is individually pumped by a 150L/s turbomolecular pump. The second chamber is a 6" diameter spherical six-way cross, which is used as a processing chamber. It is comprised of 5- 4" ports and 9-2½" ports. Attached is a temperature heating probe and a SRS 300 AMU RGA unit. A 360 L/s turbomolecular pump and a titanium sublimation pump, both of which are separately attached to a 4-way cross, pump the chamber. The chamber is located between the introduction chamber and the main analysis chamber and is isolated by two gate valves situated on both side of the chamber.

The analysis chamber is large spherical chamber of approximately 300mm diameter. The system is equipped with two imaging sources, four electron excitation sources, an Argon ion sputter gun and a 200 AMU RGA unit. The system is held at a base pressure of $1x10^{-9}$ torr or better by a combination of a 450 L/s Varian Ion Pump and a Varian tri-filament Titanium Sublimation Pump with liquid nitrogen cold trap. Once a sample is introduced, it is transported into the analysis chamber by two linear motion transfer arms and two wobble sticks. The sample is placed on a holding stage located in the center of the chamber and positioned by a XYZ and theta manipulator. A CCD camera is used to position the sample at the focusing center. The chamber is also fitted

with an SEM allowing imaging of micron size areas. Once the sample is finely positioned, it can be irradiated by a number of excitation sources. A LEG 200 electron gun can supply 10 kV electrons which can be used for SEM imaging or Auger spectroscopy. A retractable Al/Mg dual anode operated at 15 kV provides X-rays for XPS analysis. A Specs Helium (He) plasma discharge source (SPECS Scientific Instruments, Inc., Sarasota, FL, www.specs.com) can provide UV photons of 21.2eV (He I) or 40.2eV (He II) energy. These sources are maintained in a UHV environment to reduce contamination of the elements (detectors, electron filaments, etc..). For low energy photons a Coherent Ar ion laser located externally to the UHV chamber is used. The laser rests on an aluminum table located above and behind the spectrometer. The laser beam is deflected through a fused silica window port by two mirrors positioned on gimbal mounts. All sources are oriented toward the center of the chamber and can be used for photo-excitation. Data acquisition is accomplished with HP-VEE graphics software from a Pentium PC. The VEE program records the data in an ASCII format and controls all voltages to the various elements in the analyzer of the spectrometer.

The main component of the photoelectron spectrometer is the energy analyzer, which is the large dome in figure 3.4. The analyzer of the VG system is a 152.5mm radius hemispherical analyzer. A schematic representation is shown in figure 3.5. The analyzer acts as a narrow pass filter allowing only electrons with an energy E = HV, where V is the potential difference between the inner and outer hemispheres and H is a constant determined by the physical measurements of the analyzer, to be deflected through to the detector [2]. Electrons are transmitted from a grounded sample to the

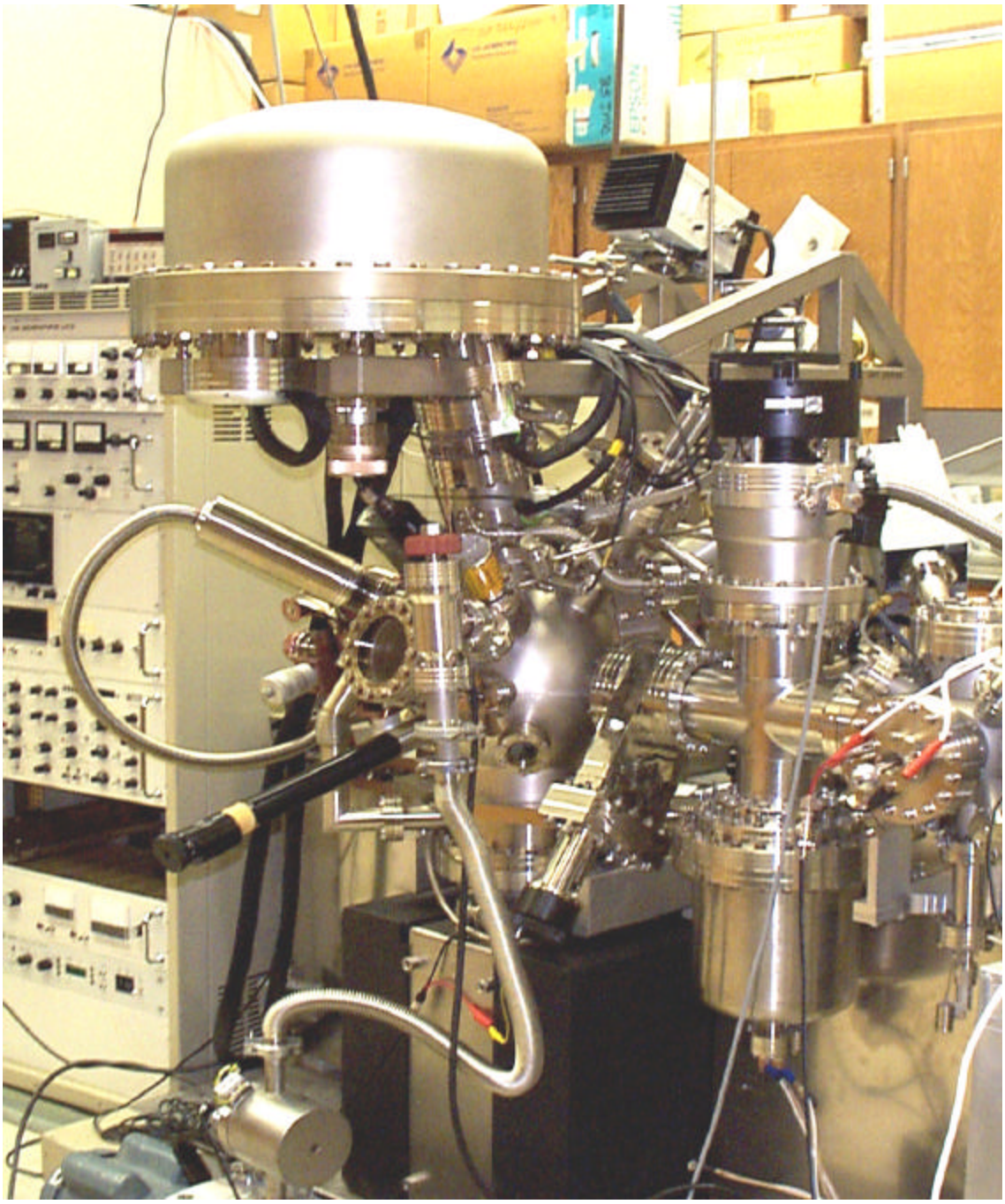

Figure 3.4 A VG Scientific ESCA lab MK II photoelectron spectrometer equipped with electron gun, Ar ion sputter gun, RGA, UV lamp and X-ray source. The system was used to measure the work functions as a function of surface composition.

analyzer by electrostatic lens. Prior to entering the analyzer, the electrons are retarded in energy by an amount R, which is the center point of the analyzer and is determined by the pass energy. The analyzer maybe operated in either of two modes, the constant analyzer energy (CAE) mode or the constant retard ratio (CRR) mode. In the CAE mode, HV is constant during a spectral run. In the CRR mode the ratio of the kinetic to the pass energy is constant. As with any analyzer there is a finite resolution to the spectrometer. The resolution (ΔE) of the analyzer is given by the following equation

$$\frac{\Delta E}{E} = \frac{\Delta r}{2R_0} + \alpha^2 = \text{constant} \qquad \text{eq. 3.2}$$

where R_0 is the mean radius of the hemispheres, Δr is the slit width of both entrance and exit slits, α is the half angle of admission of electrons and E is the full width at half maximum (FWHM) of the recorded peak. In the CAE mode ΔE is fixed and E is the pass energy setting, while in the CRR mode E is not constant and increases with increasing kinetic energy.

3.4.1 X-ray Photoelectron Spectroscopy

XPS is one of the most commonly used surface science techniques due to its ability to probe only 10-100Å of the surface [4]. Because it uses low energy X-rays, it provides a non-destructive means of both elemental and chemical analysis. X-rays are generated from a dual Al/Mg anode and impinge on the sample surface. These X-rays interact with the atoms of the solid and cause the emission of electrons via the photoelectric effect.

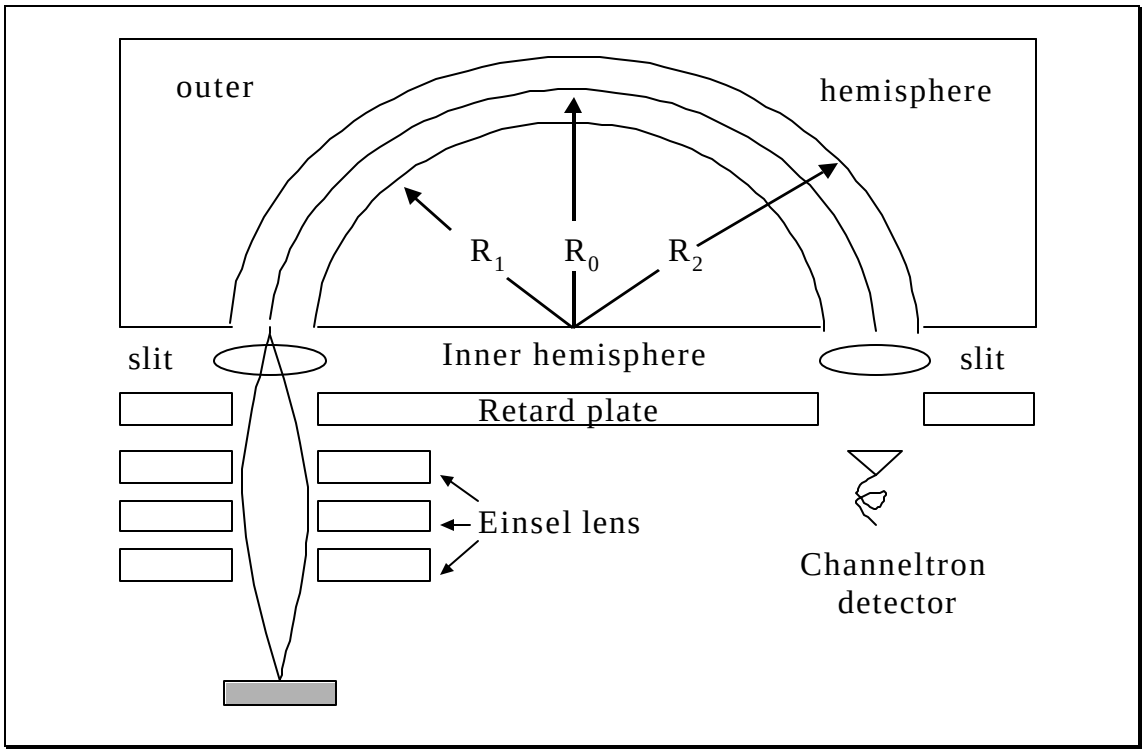

Figure 3.5 Simulated schematic of the VG hemispherical energy analyzer. Here R_1,R_o and R_2 are the radii of the inner sphere, the beam path and outer sphere.

The kinetic energy of the emitted photoelectrons is given by

$$E_{kinetic} = h\nu - E_{binding} \qquad \text{eg. 3.1}$$

where $h\nu$ is the energy of the photon and $E_{binding}$ is the binding energy of the electron.

The non-radiative Auger process also emits electrons. In the Auger process an electron from a higher energy level descends into the vacant core level and imparts energy to a higher energy electron, which is then emitted (the Auger electron). Unlike the

photoelectron, the kinetic energy of Auger electron is independent of the photon energy. The emitted electrons are energetically characterized with an electrostatic deflection energy analyzer composed of two concentric hemispherical plates.

The emission spectra are displayed as a plot of the intensity of electrons emitted versus the electron binding energy. The most intense photoelectron lines are usually relatively symmetric and are typically the narrowest lines observed in the spectra [5]. Pure metals can exhibit asymmetric photoelectron lines due to coupling with conduction electrons. Auger lines are groups of lines that are typically broader and asymmetric. The width of all lines in the spectra is the direct contribution of the natural line width of the element, the line width of the X-ray and the instrumental resolution. The chemical environment has a direct influence on the position of the spectral lines. Chemical shifts can be on the order of a few tenths of a volt to several volts. The shape and position of spectral lines provide information of the chemical composition.

All XPS spectra were obtained under the CAE mode. Both the Al and Mg anodes were used as excitation sources, depending on the sample. The pass energy was varied depending on the type of scan. Two types of scans were performed for all samples. First a survey scan was run in order to obtain information as to all possible contaminants present. Survey scans were obtained with pass energy of 10eV, corresponding to a resolution of 0.8eV, and an energy step of 0.5eV. The other type of scan was a local region scan concentrated on the highest intensity elemental peak of interest. For these scans an energy step of 0.1eV and a pass energy of 5eV (0.4eV resolution) were used. Energy calibration of the XPS system was done by using a silver sample and calibrating

with respect to the position of the Ag 3d peak. This procedure was used prior to and after heating of the sample in order to determine oxidation-reduction properties and their effects on the work functions.

3.4.2 Ultraviolet Photoelectron Spectroscopy

The principles of UPS are the same as XPS with the only difference being that only valence electrons can be emitted in UPS because lower energy photons are used. Since only the valence electrons are excited UPS provides a direct method of measuring the work functions of the material provided that it is lower than the photon energy. It can also be used to identify surface states within the band gap, as well as, direct and indirect emission processes [6,7]. Direct and indirect processes are observed by varying the energy of the UV photon. For a direct transition the kinetic energy of the emitted electron will shift by an amount equal to the change in photon energy. On the other hand, for an indirect process the kinetic energy of the emitted electron will not change when the photon energy is varied. In this study UPS was used to corroborate the work function measured by field emission and to measure the change in the work function as a function of annealing.

UPS spectroscopy was also accomplished in the VG spectrometer with a slight modification to provide better resolution. The conventional 362 power supply unit of the VG spectrometer was found to have an inherent 200mV noise ripple due to the vacuum electronics inside it. An external low energy power supply unit was built to replace the commercial VG power supply unit. The unit was driven with a 16 bit DAC from a HP 75000 mainframe that has an output of 0-10 volts. The low energy system has an

effective gain of 3 thereby transforming the 0-10 volts to 0-30 volts. A dual low bias current precision Op amp (type Op-297) serves as the input stage. A differential amplifier configuration is used to minimize ground loops and a unity gain amplifier is used for proper signal phasing. A high voltage FET-input Op amp accomplishes the voltage gain of 3, which serves to provide the signal for the output amplifiers. A series of parallel resistors are configured such that the inner and outer hemispheres, along with the analyzer plate, have the correct ratio of output voltages. A Pa-85 high voltage amp is used as the lens output amplifier and is configured by a set of resistors to have a gain of +6.12. This low energy system provides higher resolution measurement of electrons with 0-30eV of kinetic energy.

The ultraviolet source for UPS was an Innova® 90C FreD™ Ion Laser (figure 6). The laser can be operated with either of two types of wavelength selectors, one a multi-line the other a single line [8]. The laser itself is comprised of essentially four components: a laser head, a power supply, a water-cooling system and a hand held controller. In the laser head the active medium is a plasma of ionized gas contained in a low pressure tube. Passing a DC current through the gas inside the tube produces stimulated emission. The plasma tube is positioned inside an optical cavity consisting of two dielectrically coated laser mirrors. The laser in whole uses a four-mirror cavity in which two end mirrors are located at the front and rear ends of the head. The other two mirrors are folding mirrors used to focus the beam on a beta-barium borate (BBO) crystal. The crystal has very low absorption for fundamental wavelengths in the visible and near-infrared spectrum, a relatively high non-linear coefficient and is transparent

down to 200nm. The crystal itself allows second harmonic generation (SHG) of the fundamental wavelength. In the SHG mode the fundamental wavelength generates in the BBO crystal a non-linear polarization, which radiates at twice the frequency of the fundamental, yet maintaining the same phase relationship. It is this frequency doubling which permits the obtainment of the 229nm line.

Electrical power drawn from a 3-phase power line is conditioned by the power supply and used to operate the plasma tube. The power supply uses a 3-phase rectifier and LC filter to provide DC current for the tube and magnet used to confine the plasma. In order to minimize the optical noise on the output beam a linear passbank regulates the current. The laser system is controlled by firmware located on the control board inside the power supply, which is accessed by either a remote control module or a RS-232c interface. The compact remote control module features push-button control of all operating parameters. The status and operations are displayed on a 2-line, 16 character LCD.

UPS was performed on wire tips as well as flat samples which were also subjected to annealing. All spectra were obtained using the 229nm (5.41eV) line from the Ar^+ Laser. Samples were grounded and run with pass energy of 0.25eV (20meV resolution). UPS spectra are Gaussian in shape and are fitted with the Peakfit program [9] to identify the individual peak positions. All samples were heated to various temperatures to either remove absorbed species or observe oxidation-reduction reactions. The effect of these two phenomena on the measured work function was monitored with UPS. The UPS data

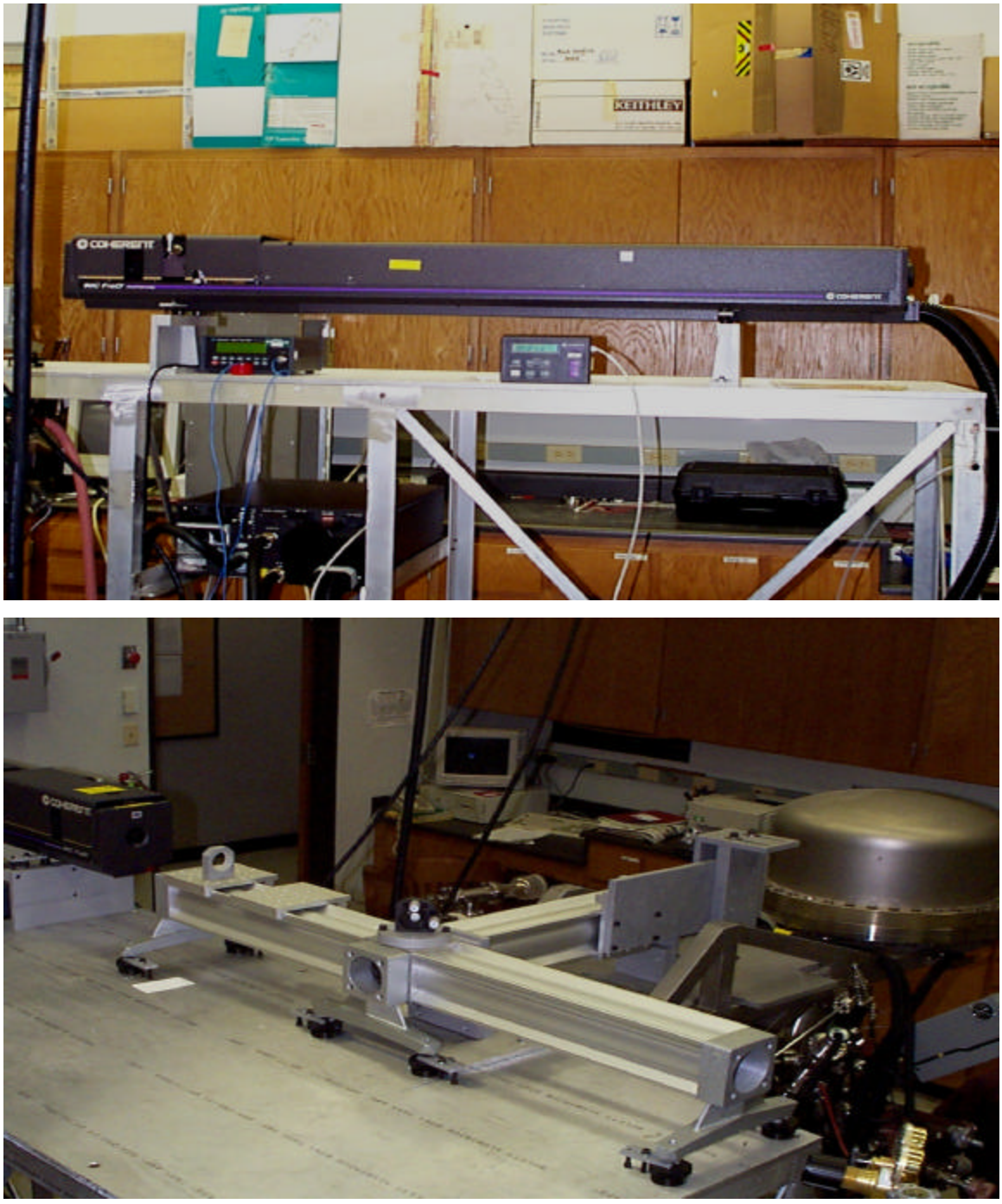

Figure 3. 6 Innova 90C FreD Ion Laser used for low energy UPS. Laser head (top) and gimbal mounted mirrors (bottom) provide 229 nm photons to be reflected through a sapphire window port located on the back of the VG spectrometer.

were then used to corroborate field emission studies in which similar experiments were preformed.

3.5 Field Emission Spectroscopy and Fowler-Nordheim Plots

Field emission was used to determine the effects of oxygen exposure and thermal annealing on the emission characteristics of emitter tips. The current-voltage measurements and energy distributions were measured in situ. By monitoring these simultaneously, any degradation could be attributed to either a change in the work function or geometry of the tip.

Field emission experiments were conducted in the stainless steel chamber depicted in figure 3.7. The chamber itself is an 8" conflat 4-way cross with two additional 2 3/4" ports located 180° relative to each other and 90° relative to the four 8" ports. A 360 L/s turbo pump and a 300 L/s Varian Starcell ion pump located opposite to each other pump the system. The turbo pump is isolated from the cross by an 8" right angle gate valve. In addition, a sapphire sealed variable leak valve attached to the cross allows the introduction of gases for dosing experiments. Typical base pressure of the system is ~ 1 x 10^{-9} torr as measured by a glass encapsulated ion gauge. A SRS 200 AMU RGA is used to measure the partial pressure of residual gases. Finally the two major components of the system are a motor driven manipulator and a simulated spherical energy analyzer located opposite to each other.

The manipulator is a Huntington MPM-600-RM. It is a high precision XYZ and Theta motor driven UHV manipulator with a maximum position resolution of 2 microns. It isattached to the camber via a 6" conflat flange. Six MHV feedthroughs located

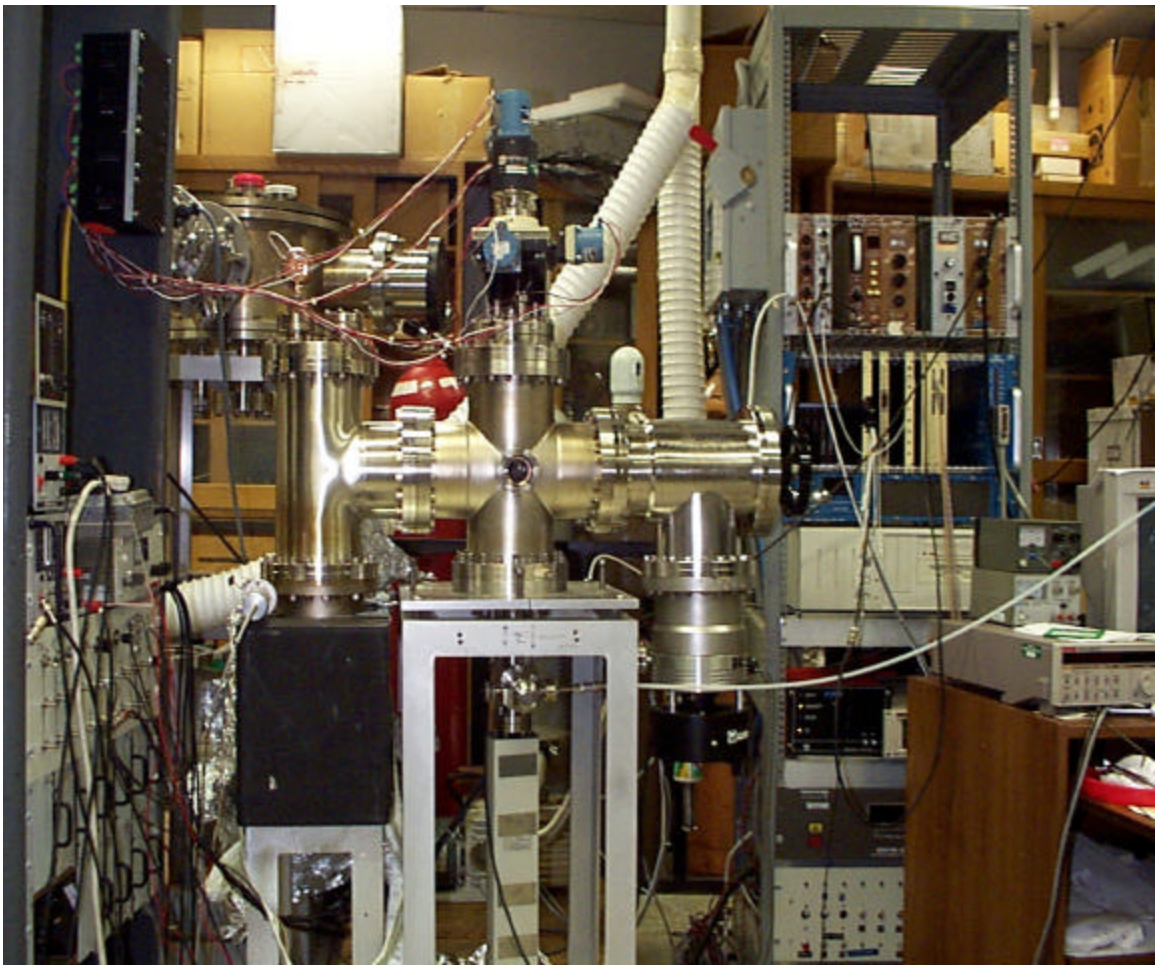

Figure 3.7 Field emission chamber. Both FEED and I-V measurements of tips are measured in this system. Huntington manipulator is located on top of the 4-way cross, while the energy analyzer is mounted on the bottom of the cross.

on the flange provide electrical contact to the tips. Up to four tips may be loaded at any particular time. A set of four stepper motors are used to position the tips, each is controlled by RS-232 serial ASCII commands that are typed into a hand held unit.

A view port located in the front of the system allows the tip to be coarsely positioned over the anode. Another view port is located at the bottom of the UHV cross where a laser is positioned. The laser beam passes through the view port, through an opening in the energy analyzer and lens system and finally through a probe hole in the anode. The laser illuminates the emitter tip when it positioned directly over the probe hole. Once over the hole an initial distribution is obtained to aid in the fine positioning of the tip. The extraction voltage is fixed and the energy analyzer is set at a particular energy corresponding to the center of the distribution. The tip is finely positioned by moving the tip until the detected signal is maximized and the emission current is optimized. The field emitted electrons can then be analyzed by the analyzer.

The analyzer system consists of an extraction aperture, a collimated lens system and a simulated hemispherical energy analyzer. The analyzer is mounted to the bottom of the cross. All parts are made of oxygen free (OFHC) copper and are supported on a ground mounting plate which is connected to a 6" conflat flange by four threaded rods. The plate has two openings that are aligned with the entrance and exit apertures of the energy analyzer. The extraction aperture is a small 0.012" hole located in the center of the anode. The electrons that pass through the hole are then focused by a set of four collimated electrostatic lenses. The diameter of the lenses decrease from the anode to the analyzer entrance so as to minimize inelastic interaction of the electrons with the surface

of the lenses as well as provide good focusing and throughput [10]. The extraction anode and lens system are located above the mounting plate while the analyzer is located below.

The energy analyzer is a simulated 180° spherical spectrometer as reported by Jost in 1979 [11]. It is composed of a base plate containing both entrance and exit slits, a cylindrically shaped inner and outer electrode that are made from wire mesh and are supported by two half disk plates, and lastly two half disk auxiliary electrodes located between the inner and outer electrodes. The dimensions of all parts can be found elsewhere [1]. By applying the correct voltages to the auxiliary electrodes, relative to the inner and outer electrodes, the electric fields of a true hemispherical analyzer are replicated. Jost defined a parameter, p, which is a ratio of the voltage difference on the analyzers' electrodes.

$$p = \frac{(V_{aux} - V_{outer})}{(V_{inner} - V_{outer})} \qquad \text{eq. 3.2}$$

If p = 0.4, the electric fields in the analyzer imitate that of a hemispherical analyzer with the field falling off as $1/r^2$. On the other hand, if p = 0.76 a cylindrical analyzer is imitated with the field falling as 1/r. From equation 3.2 with p = 0.4, rearrangement gives

$$V_{aux} = 0.4(\Delta V) + V_{outer} \qquad \text{eq 3.3}$$

Where $\Delta V = V_{inner} - V_{outer}$ and is greater than zero for negative charge energy analysis since the inner electrode is more positively biased. The correct biased is accomplished when ΔV is 40% above the outer sphere voltage and 60% below the inner sphere voltage. For this particular analyzer the base plate (retarding plate) is at the same potential as the

auxiliary plates. The following equations derived by Kuyatt and Simpson [12] determine this situation.

$$\Delta V = V_o \left(\frac{R_2}{R_1} - \frac{R_1}{R_2} \right) \; ; \Delta V = V_o(1.0) \qquad \text{eq. 3.4}$$

$$V_{inner} = V_o[3 - 2(R_o/R_1)] \; ; \; V_{inner} = 0.4V_o \qquad \text{eq. 3.5}$$

$$V_{outer} = V_o[3 - 2(R_o/R_2)] \; ; \; V_{outer} = 1.4V_o \qquad \text{eq. 3.6}$$

Here ΔV is the potential difference between the inner and outer spheres, V_o is the kinetic energy of the electrons traveling through the analyzer, and R_1, R_o, R_2 are the respective radii of the inner sphere, beam path and outer sphere. In the particular case of measuring electrons from a source of zero voltage reference, V_o is also the potential placed on the base plate (V_R). Substituting the above equations for V_{inner} and V_{outer} into equation 3.2 the following is obtained.

$$V_{aux} = V_o = V_R \qquad \text{eq. 3.7}$$

Kuyatt and Simpson have calculated the energy resolution and determined it to be a ratio between the diameters of the entrance and exit slits and the beam path ($2R_o$). Therefore the resolution for our spectrometer is

$$\frac{\Delta E}{E} = \frac{w}{2R_0} = \frac{1}{13} \qquad \text{eq 3.8}$$

where ΔE is the full width half maximum (FWHM) of the energy distribution and E is the pass energy. Energy spectra were obtained in the CAE mode as described in the previous section on photoelectron spectroscopy.

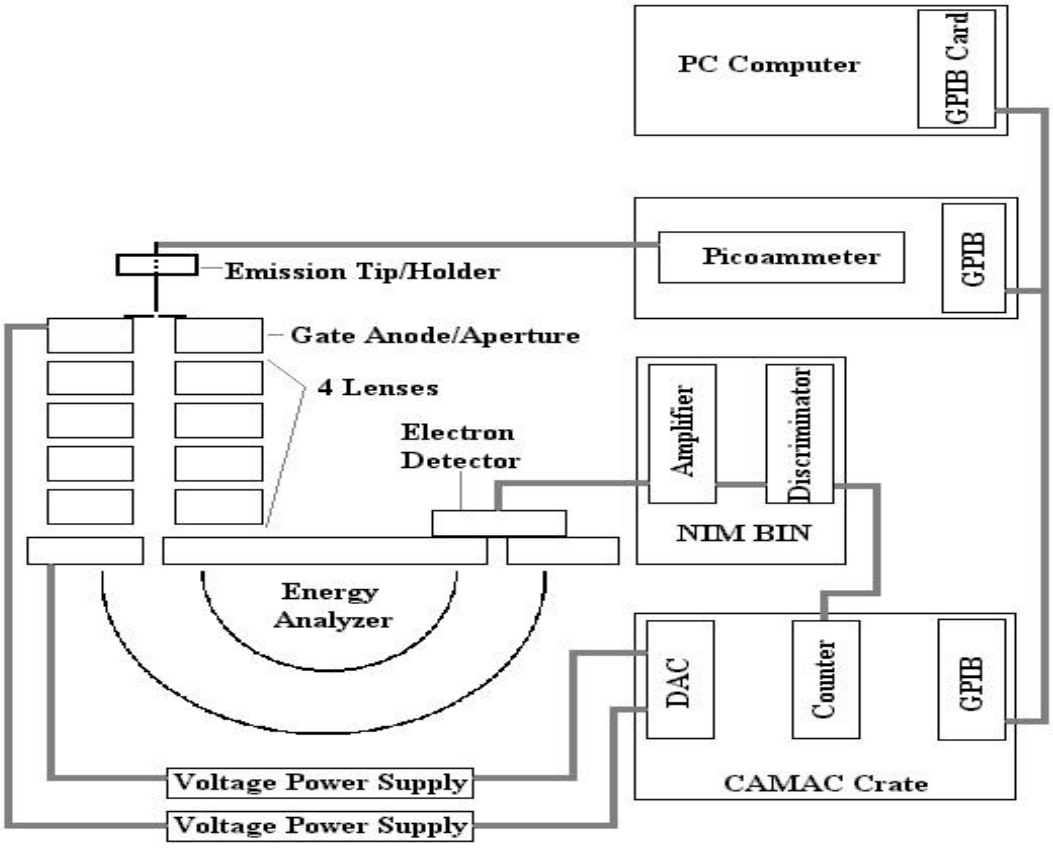

Figure 3.8 Configuration of the data acquisition system of the FEED chamber. The PC software allows the anode voltage to be stepped and the retard voltage on the base plate to be sweep by interfacing with a CAMAC crate.

The data acquisition configuration is shown in figure 3.8. It consists of a PC with HP-VEE graphics software, a CAMAC crate and a Keithly 486 picoammeter. The crate and the picoammeter are connected by a GPIB interface. The picoammeter is connected between the emitter tip and a power supply, which places a –90V on the tip; thus, the emission current is read from the tip. The CAMAC crate sends out two DAC voltages to power supplies, which step the voltages on the anode and base plate. One DAC voltage goes to an Ortec 3 kV power supply that provides the anode voltage, the other DAC voltage goes to a 100V power supply that steps the base plate so as to scan the electron energies. The electrons passing through the analyzer are detected by a set of channel plate detectors, and their pulse is received at the CAMAC crate.

Energy distributions (FEED) were obtained prior to I-V curves to avoid any desorption or sputtering effects of high emission currents associated with the higher anode voltages of the I-V sweeps. The distributions were acquired by setting the anode voltage to a fixed value so that a particular current (usually 1nA or less) is maintained. The pass energy is set at 5 eV and the energy is scanned from 80-90 eV (kinetic energy) at a step of 0.1 eV. The signal is counted for 1 second at each energy step of a scan and the energy spectra usually consists of 5 scans depending on the signal to noise ratio. I-V curves were obtained after FEEDs . In this case the analyzer is held constant (not swept) while the anode voltage is stepped over a range of voltages. The measured emission current at each particular voltage during a sweep is the averaged value of three data points. The resultant I-V curve is the compilation of 5 individual sweeps; therefore, each point on the I-V curves is actually an average of 15 data points. This procedure was

followed after exposing tips to oxygen and heating to monitor the changes occurring at the tip surface.

References:

1. J.M. Bernhard, A.A. Rouse, E.D. Sosa, D.E. Golden. Rev. Sci. Instrum., **70**, 3299 (1999).
2. VG ESCA lab MK II Operations Manual, VG Scientific Limited, 1985.
3. Stanford Research Systems, Inc. 1290-D Reamwood Avenue, Sunnyvale, CA 94089.
4. D. Briggs, M.P. Seah, *Practical Surface Analysis*, John Wiley & Sons, Ltd., New York 1983.
5. Handbook of X-ray Photoelectron Spectroscopy. Perkin-Elmer Corporation, Physical Electronics Division. 6509 Flying Cloud Drive. Eden Prairie, Minnesota 55344.
6. A.A. Rouse, J.B. Bernhard, E.D. Sosa, D.E. Golden. Appl. Phys. Lett. **75**, 1999.
7. I.A. Akwani, E.D. Sosa, J.Bernhard, S.C. Lim, R.E. Stallcup II, J.M.Perez, D.E. Golden. Mat. Res. Soc. Symp. Proc. **509**, 1998.
8. Operators Manuel Innova® 90C FreD™ Ion Laser, Coherent, Inc. Laser Group, 5100 Patrick Henry Drive, Santa Clara, CA 95054.
9. Peakfit, SPSS, Inc., 444 North Michigan Avenue, Chicago, IL 60611.
10. J.M. Bernhard, PhD. Thesis, University of North Texas 1999.
11. K. Jost, J. Phys., **E12**, 1006 (1979).
12. C.E Kuyatt and J.A. Simpson, Rev. Sci. Instrum., **38**,1 (1967).

CHAPTER 4

EMISSION CHARACTERISTICS OF MOLYBDENUM

4.1 Introduction

In this chapter the experimental results of both field and photoemission from molybdenum (Mo) surfaces will be presented. X-ray diffraction (XRD) and X-ray photoelectron spectroscopy (XPS) were used to examine the resultant structure and chemical composition of Mo surfaces after the etch process. Both ultra-violet photoelectron spectroscopy (UPS) and field emission electron spectroscopy (FEES) were used to measure the work functions of Mo and its oxides. XPS and UPS monitored changes in the composition and work functions of the Mo surface during thermal annealing. Field emission energy spectroscopy was used to examine any variation in the field emission properties as a result of annealing and exposures to oxygen. The effect of oxygen exposure on Mo field emitter tips was the main emphasis of this work.

4.2 Sample Preparation and Characterization

Flat samples were made by cutting a $1cm^2$ square of 0.1mm (0.004in) thick Mo foil which was 99.95% Mo. The $1cm^2$ Mo foil was then subjected to the similar etching condition of Mo tips. The foil was biased with +10V while submerged in the tip etching solution for a period of 1 minute in order to form any oxides that may form on tips when etched. XRD, XPS and UPS were used to characterize these samples. Mo tips were

made from 0.5mm (0.02in) diameter wire etched in an 8% by weight NaOH or KOH aqueous solution as described in chapter 3. After etching was complete the tip was rinsed with distilled water followed by a HF rinse. Tips were viewed under SEM to observe the degree and quality of etching. Tips used for field emission were the spot welded onto a tungsten filament as described in chapter 3. Tips on which XPS was preformed were mounted upright on a standard VG sample peg in which a small hole was bored down the center. Tips were heated on the VG heater stage and changes in the chemical composition were monitored by XPS.

In general, tips formed with NaOH were etched more rapidly than those with KOH. However, those etched in NaOH were more oxidized than those in KOH as was indicated by shifting in the field emission energy distribution (FEED) spectra to higher binding energies. This can be explained by the greater ionic strength(conductivity) of the KOH solution, which facilitates ion migration through solution. For this reason only tips etched with NaOH were used for field emission experiments. As stated previously, tips were viewed under an SEM to determined the quality and degree of etching. The sharpness of tips varied from tenths of a micron to hundredths of microns, but only those with sharpness of a micron or less were used in field emission experiments. The degree of oxidation could be observed in the smoothness of the tip as well as in the color of the tip after etching. Tips that were heavily oxidized visibly appeared black and showed spalling or cracking in the SEM, where large platelets of oxide were highly visible as can be seen in figure 1. Similar morphology has been observed on Mo tips coated with iridium oxide, in which Ir is first deposited and then thermally oxidized at elevated

temperatures [1]. Regardless of the smoothness, all tips showed signs of oxidation in FEED and XPS spectra due to Mo reactivity to atmospheric oxygen.

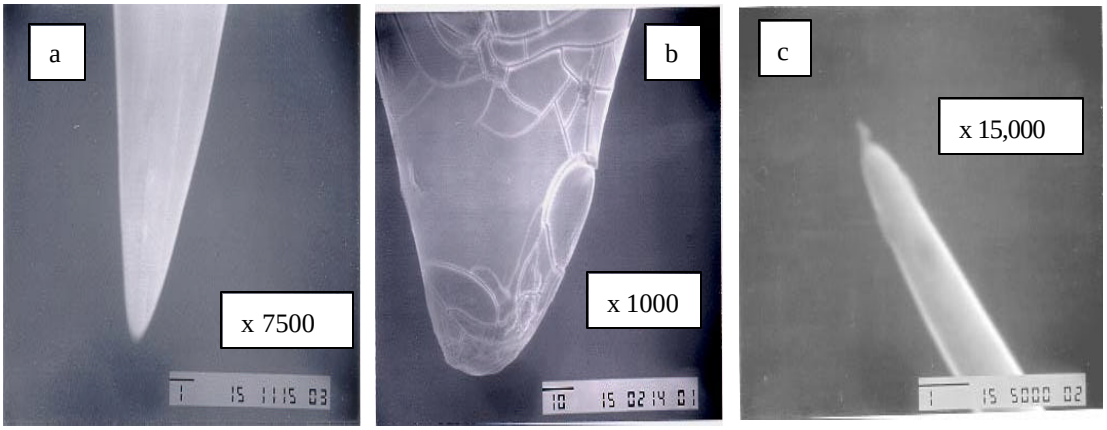

Figure 4.1 SEM micrographs of etched molybdenum tips: a) smooth tip with little oxidation b) heavily oxidized tip and c) a sharp tip.

XRD was performed on two individual pieces of Mo foil as shown in figure 4.2. One of the pieces was plain Mo foil as purchased, while the other piece was foil that had been processed in a similar manner to etched tips. It is evident that the peaks at 2θ values of 11.75°, 12.35°, 58.8°, 73.8° and 116.1° are present in both spectra. From PDF file # 42-1120 of the XRD database, the peaks at 58.8°, 73.8° and 116.1° correspond to the (2 0 0), (2 1 1) and (2 2 2) planes of Mo. The peaks at 11.75° and 12.35° are more difficult to assign since no database files with 2θ values below 20° exist for Mo. Several database

files for the oxides of Mo existed which contained values in close proximity to these values. In addition, these peaks show a slight increase in their intensity when the foil is subjected to etching conditions. For these reasons it is believed that these two peaks correspond to oxides of Mo, possibly MoO_2 and/or MoO_3. Another feature that is evident is the appearance and disappearance of several peaks when the foil is processed. Three new peaks arise due to the etch process. The peaks at 19.55° and 20.9° are attributed to the (2 0 0) and (10 4 0) planes of MoO_3, while the peak at 18.85° is a result of the (-1 0 1) plane of MoO_2. The peaks at 40.75°, 101.6° and 132.8° associated with the (1 1 0), (3 1 0) and (3 2 1) planes of Mo vanish as a result of the processing. This is explained by the fact that they are of low intensity and thus the formation of a oxide layer (1-10μm) causes the signal to be masked. The formation of a thin oxide is also supported by the fact that the three new peaks are also of low intensity. This low intensity however makes the identification of the contributing oxide somewhat difficult. To properly classify the oxide present a more sensitive technique is required.

Since XPS is a more surface sensitive technique it can be used to detect the presence of a thin oxide layer. In addition to the detection of an oxide layer, it can provide a direct identification of the type of oxide present. The interaction of oxygen with Mo will cause a change in the oxidation state of Mo. This change in the oxidation state causes the photoelectrons from the Mo 3d state to be shifted to higher binding energy due to reconfiguration of the electron energy levels within the atom. By measuring the position of the Mo 3d peak, the composition of any oxide present can be evaluated. For these reasons, XPS was performed on both tip and flat samples.

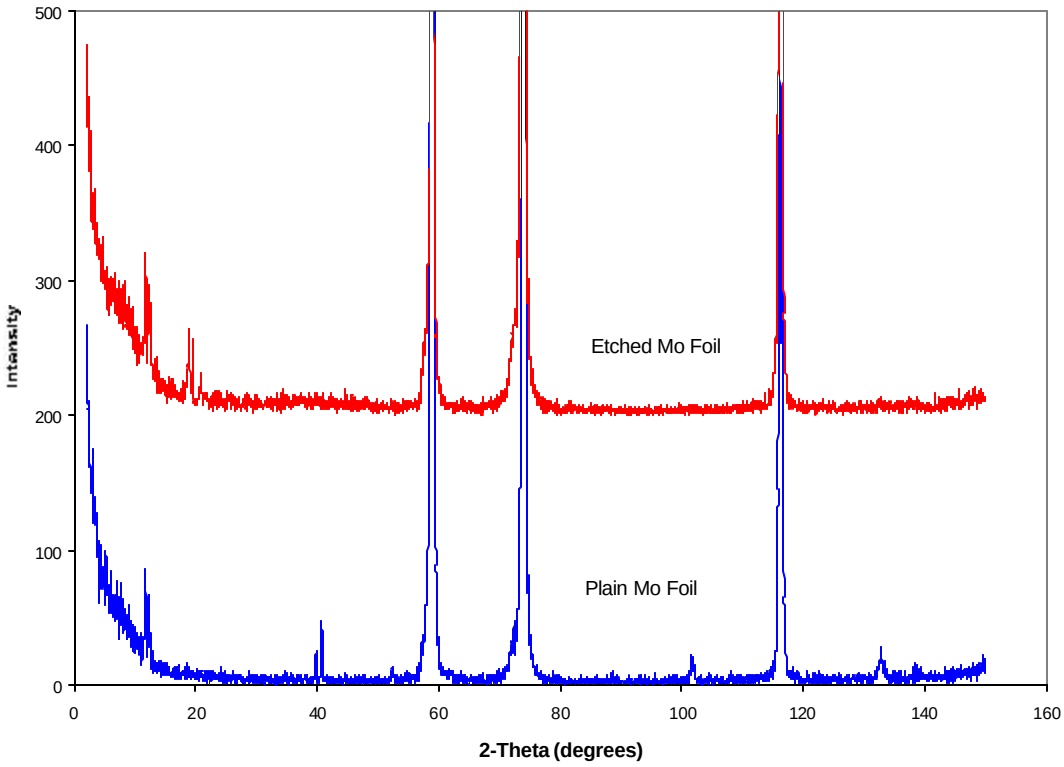

Figure 4.2 XRD pattern of as purchased Mo foil and Mo foil processed in NaOH etching solution.

The XPS spectra of the Mo 3d peak for Mo foils is shown in Figure 4.3. The typical Mo 3d peak consists of a doublet as a result of spin orbit coupling. The doublet peaks are assigned to the Mo $3d_{3/2}$ and the Mo $3d_{5/2}$ states. According to the handbook of X-ray photoelectron spectroscopy [2], approximately 3eV splits the doublet, and the corresponding binding energies of Mo, MoO_2 and MoO_3 are 227.7, 229.3 and 232.7eV. It is clearly evident that the spectrum of the two foils consists of three peaks. In the spectra of the non-processed foil the peak centers are located at binding energies of

228, 232.6 and 236eV. The peak at 228eV is attributed to $3d_{3/2}$ of Mo and that at 236eV is from the $3d_{5/2}$ of MoO_3. The peak at 232.6eV is a combination of the Mo $3d_{5/2}$ and the MoO_3 $3d_{3/2}$. The processed foil has its peaks located at binding energies of 230.8, 232.8, 234 and 236eV. The low energy peak is due to the $3d_{5/2}$ of MoO_2, while the high energy peak is from the $3d_{3/2}$ MoO_3. The center peak is a combination of the MoO_2 $3d_{3/2}$ and the MoO_3 $3d_{5/2}$.

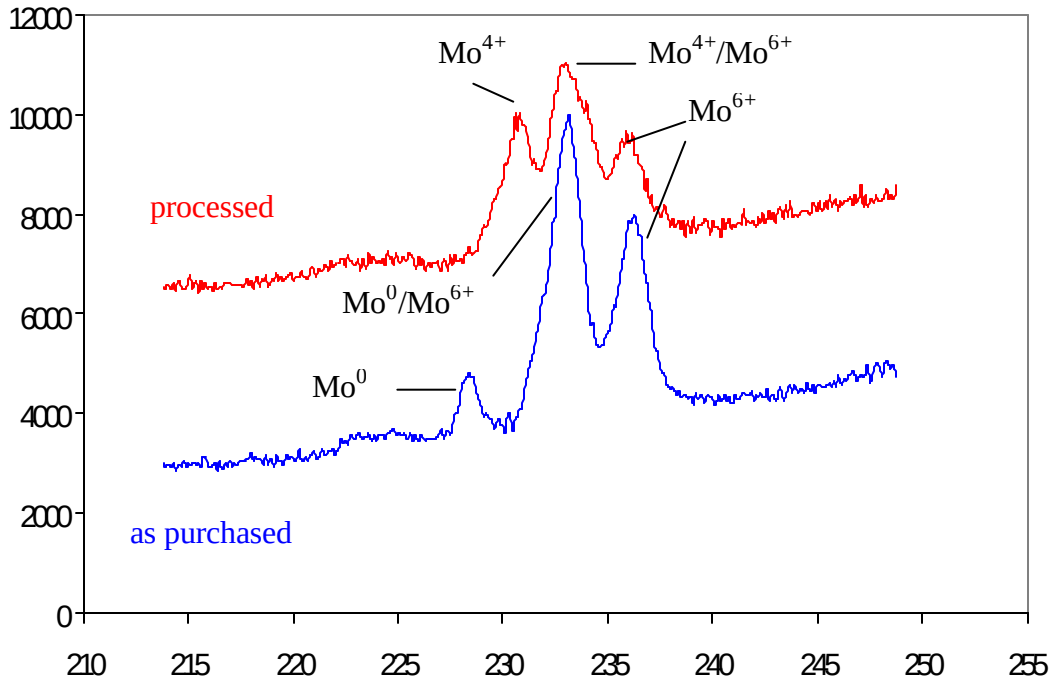

Figure 4.3 XPS of Mo foil showing the difference in oxides present in a processed and non-processed foil.

The major differences in the two spectra are the existence of a Mo peak in the non-processed foil and that of a MoO_2 peak in the processed foil. The Mo peak in the non-processed foil would indicate that the oxide thickness is thin due to the sensitivity of XPS, which probes up to 100Å [3]. The lower free energy of formation (ΔG_f^o) of MoO_3 (-668 kJ/mol compared to –533 kJ/mol for MoO_2) would suggest that MoO_3 will form more readily than MoO_2, thus supporting the fact that only MoO_3 is present in the non-processed foil. In oxidation studies it has been shown that MoO_2 can be present when the thickness of oxide layer is between 0.6 and 0.8nm [4]. The oxide film is optically visible in the processed foil as a black film indicating a much thicker oxide. The formation of MoO_2 is therefore enhanced by the electrochemical etch process.

4.3 Effects of Temperature on the Emission Characteristics of Molybdenum

In order to obtain cleaner field emission display (FED) devices they are often outgassed by heating the array to several hundred degrees centigrade to clean the components of the display device. Due to the components on which arrays are processed, this temperature does not exceed 500 °C [5,6]. To study the consequences of such a procedure, both Mo foil and tip samples were heated to temperatures ranging from 150-800 °C. The chemical composition was monitored after each annealing by XPS, which indicated any oxidation or reduction of the surface. Both UPS and FEES monitored changes in the work function due to annealing. The desorption of any chemical species was tracked by an RGA mass spectrometer.

Molybdenum is known to exist as various complexes such as hydroxides, oxides and suboxides [7]. In order to determine whether annealing of Mo emitters improves the

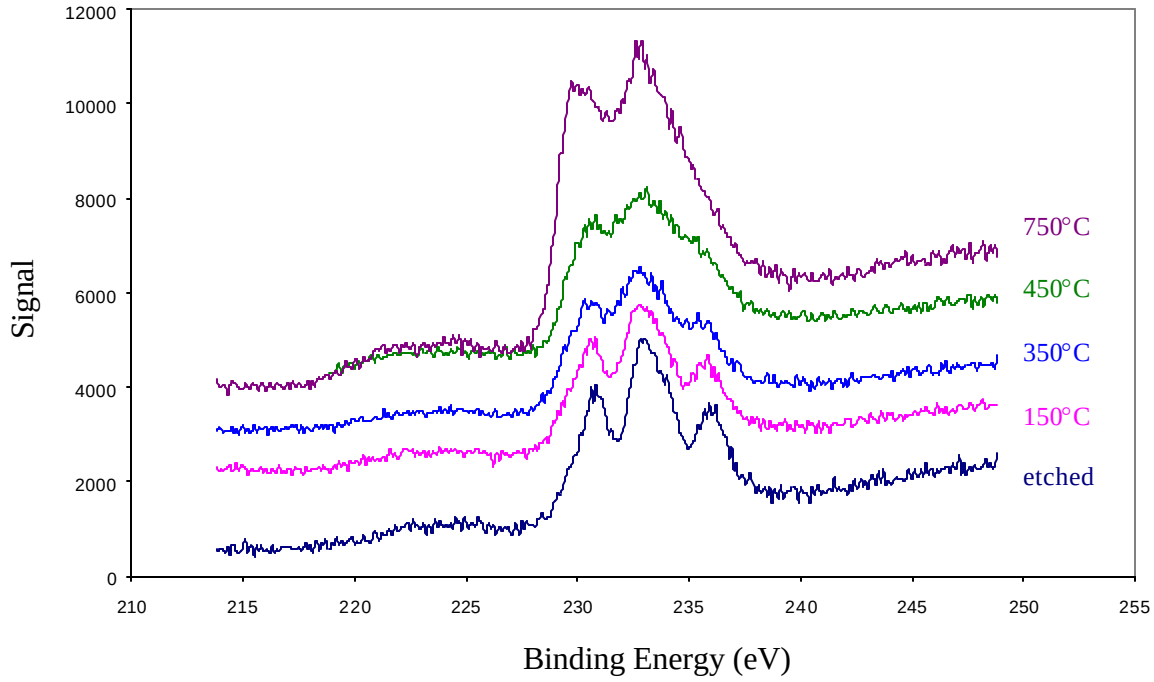

Figure 4.4 XPS of heavily oxidized Mo foil heated at various temperatures. MoO_3 is seen to decompose between 350 and 450 °C, while MoO_2 can exist up to 750 °C.

emission behavior, XPS, UPS and FEEDs were conducted on flat and tip samples at various temperatures and were allowed to cool to room temperature prior to data analysis. Figure 4.4 is a XPS spectrum of a Mo foil which was processed through the typical etch cycle and heated at temperatures ranging from 150-750 °C on the VG heater stage located in the processing chamber. Figure 4.5 is a corresponding Mo tip that was etched and heated through a range of 150-450 °C also on the VG heater stage. In the case of the Mo tip, MoO_2 is not evident in the preliminary scan. The MoO_2 was most likely removed by

the HF rinse, and the MoO_3 formed readily during the transfer process upon air exposure. Nevertheless, in both cases MoO_3 exists and is converted to MoO_2 as the temperature is increased from 350 °C to 450 °C as is seen by the reduction of the MoO_3 $3d_{5/2}$ peak . The reduction of MoO_3 to MoO_2 occurs at temperatures ranging from as low as 360 °C to as high as 550 °C depending on the amount present [8]. MoO_2 is the more thermodynamically stable at elevated temperatures and can exist up to 900 °C [9]. As can be seen in figure 4.4, MoO_2 still exists even after annealing at 750 °C for a period of

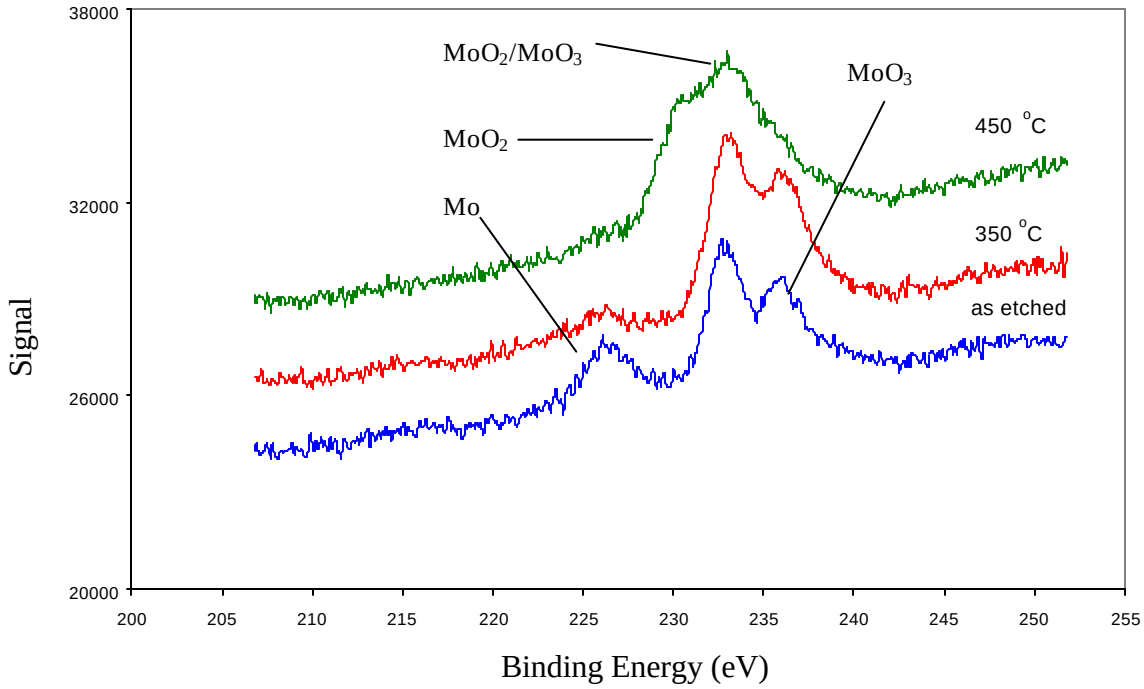

Figure 4.5 XPS of an etched Mo tip heated to a maximum of 450 °C, the temperature to which array devices can be heated to.

3 hours indicating its stability at higher temperature. Unfortunately the VG heater stage could not be operated above 750 °C in these experiments due to rupturing of the heating element. However previous work on Mo_2C films shows that MoO_2 is removed at temperatures between 825 and 900 °C [10]. Thus at temperatures allowed by display components Mo cathodes will suffer due to the predominant existence of a higher work function oxide, MoO_2 .

The variation in the work function of Mo foils as they were heated was detected using Ultra-violet Photoelectron Spectroscopy (UPS). UPS was performed sequentially after XPS was done. UPS data were acquired using 5.41eV photons from a Coherent Ar^+ Laser as described in chapter 3. All spectra were obtained using a pass energy of 0.25eV and a slit width of 6mm resulting in a resolution of 20meV. The data was recorded over 10 scans with 10meV steps over a kinetic energy range of 0-3eV. UPS results are shown in figure 4.6 for temperatures of 25, 150, 350, 450 and 750 °C. Figure 4.7 is a corresponding peak fitting of the UPS energy spectrum for the oxidized Mo foil heated to 750 °C for a duration of 3 hours. It is evident from figure 4.6 than the signal intensity increases with increasing temperature. The signal to noise ratio also improved with temperature. The increase in signal and the improved signal to noise ratio can be explained by greater conductivity of the sample as the oxide is removed as will be shown in the field emission section. All energy spectra could be fitted with three Gaussian peaks with energies corresponding to work functions of 4.8, 4.6 and 4.3eV. The 4.6eV work function is attributed to Mo while the other two values are most likely due to surface contamination due to either the oxides of Mo or absorbed species on the foil.

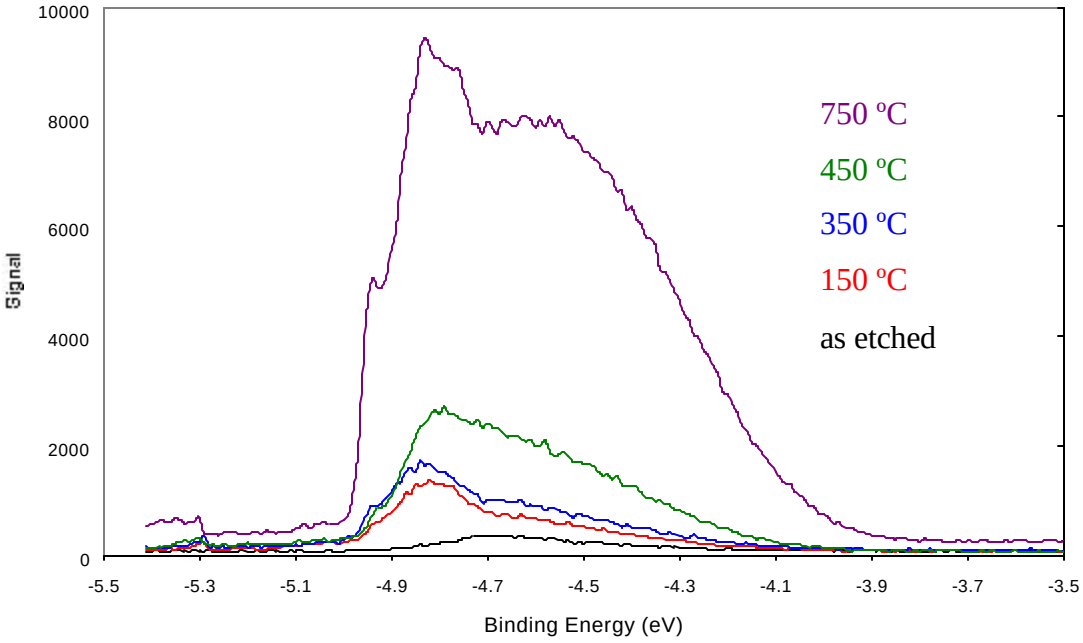

Figure 4.6 UPS spectra of oxidized Mo foil at various temperatures using 5.41eV photons from a Coherent 90C FreD™ Argon ion laser.

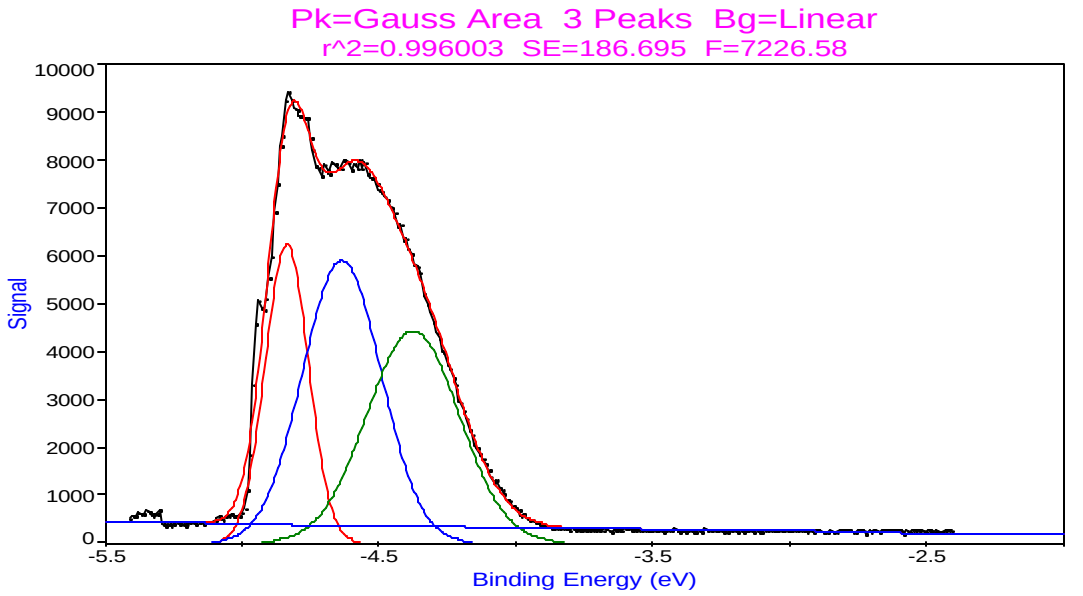

Figure 4.7 Peak fitted UPS energy spectrum for Mo foil heated to 750 °C for a period of 3 hours. Peak centers are located at –4.3, -4.58 and -4.83eV.

RGA analysis shows that H_2^+, OH^+, H_2O^+ and CO_2^+ are the major desorbing species which is seen in figure 4.8. Apparently 750 °C is not enough to fully decompose the oxide completely.

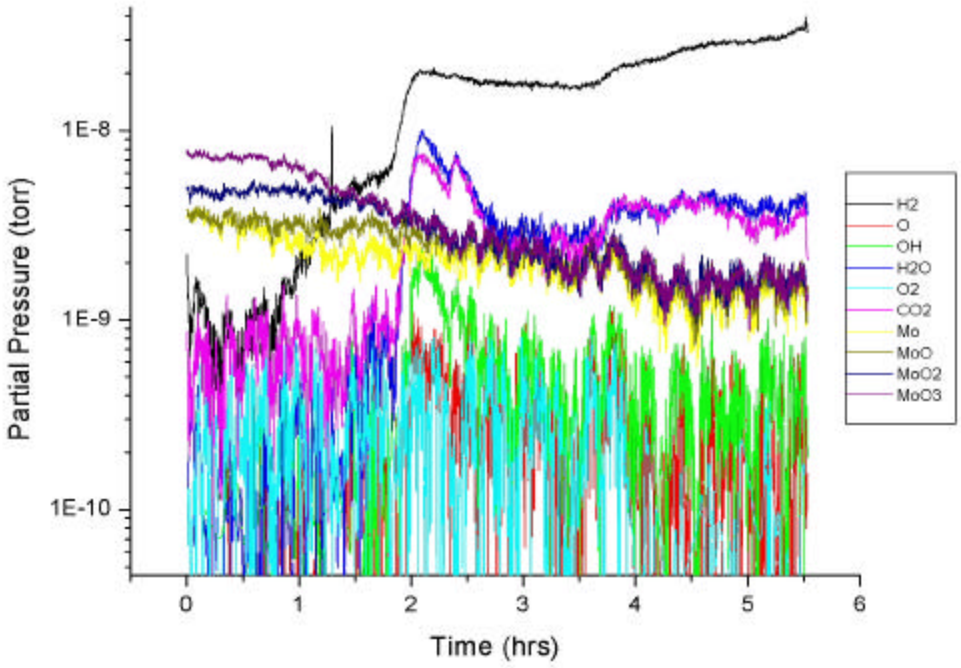

Figure 4.8 RGA of oxidized Mo foil heated to 450 °C for ~ 3 hours.

Field emission from oxidized tips was also preformed as a function of heating in order to observe the effects of oxide formation on the emission characteristics. All FEED spectra was run with a pass energy of 5eV and a step size of 0.1eV generally over a kinetic energy range of 10eV. The individual Mo tip was heated at elevated temperatures of 350, 450, 550 and 800 °C while measuring the energy distribution after each thermal treatment. The energy distribution of a single tip subjected to these temperatures is shown in figure 4.9. A common observation was the shifting of the distribution to higher binding energies when the tip was highly oxidized. The tip used in figure 4.9 had an initial binding energy of greater than –10eV. The shifting is attributed to a charge build up across the surface of the oxide layer due to the nonconductive nature of the oxide. The electrons thus require more energy to overcome the surface barrier resulting in a lower kinetic energy of field emitted electrons. As the oxide is removed the distribution moves to lower binding energies. Therefore, the first effect an oxide layer has is to cause an apparent continous increase in the work function as the oxide thickness progresses.

The distribution after heating to 350 °C was fitted with three Exponentially Modified Gaussian (EMG) peaks, whose inflection points correspond to work functions of –7.52, -6.65 and –5.57eV. When heated to 450 °C the peaks shift to energies of –6.32, -5.69 and -4.54eV. These three peaks can be assigned to MoO_2, Mo and MoO_3, whose work functions are in the vicinity of 5.3, 4.6 and 3.5eV as have been reported [11,12,13,14]. The energy separation in these work function values of the two oxides of Mo with respect to the pure metal is 0.7 and 1.1eV respectively. The work function of Mo is known to initially decrease and then increase when the Mo surface is gradually

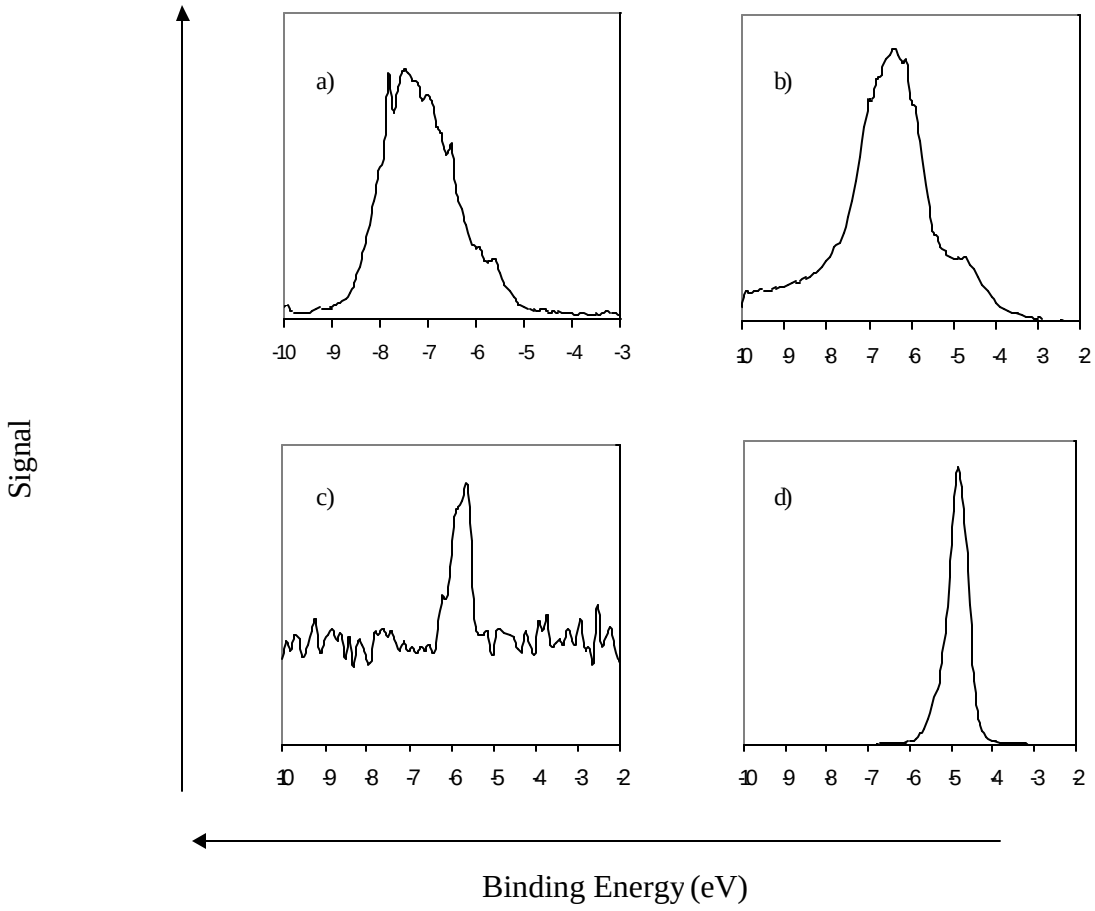

Figure 4.9 Field emission energy distributions (FEED) of a Mo single tip heated to temperatures of a) 350 °C, b) 450 °C, c) 550 °C and d) 800 °C. The distributions shift to lower binding energies and the widths become narrower as the tip is reduced to clean Mo.

oxidized [15,16,17]. The above work functions are separated by an average value of 0.75 and 1.11eV which are in good agreement to the above separations. This would indicate that these peaks are consistent with MoO_2 and MoO_3 and the shifting to lower energy results from the reduction of the oxide layer thickness due to reduced charging.

Next, when the tip is heated to 550 °C the energy distribution reduces to one peak with a work function of 5.8eV. This can be interpreted as the total oxidation of the Mo and the reduction or desorption of MoO_3 to MoO_2 which has been reported to occur over a temperature range of 300-555 °C, previously stated in the XPS section. It has also been reported that 500 °C is the temperature at which it is no longer thermodynamically stable for MoO_3 to exist in the absence of oxygen [18]. Finally, when the tip is heated to 900 °C the tip is reduced to the pure Mo metal as is seen in the distribution. The distribution can be fitted well with only one EMG which has an inflection point at 4.61 eV. This in excellent agreement with the work function of polycrystalline Mo taken as 4.6eV [19]. This data would thereby indicate that 450 °C would not be sufficient to provide cleaner Mo array devices.

4.4 Stability of Clean Molybdenum Field Emitters Exposed to Oxygen

Field emission from molybdenum emitters has been shown to degrade over time when exposed to oxygen or poor vacuum conditions [20,21]. The general consensus is that the failure mechanism involves the oxidation or sputtering of the emission tip. However most experiments have been conducted under voltage regulation; that is, the voltage is varied to produce a limited current. In order to determine which mechanism contributes to the degradation, Mo single microtips were exposed to oxygen during

operation while closely monitoring the current-voltage properties and the distribution of emitted electrons as the current was varied. These measurements were then used to conclude as to which mechanism affected the emission degradation.

Prior to exposing Mo field emitters to oxygen gas, the tip was cleaned by heating to ~ 900°C until an energy distribution of pure Mo was obtained. Tips were then exposed to research grade oxygen (O_2) while the tip was in operation. Oxygen was introduced through a variable leak valve and the pressure was measured with an ion gauge. On O_2 introduction, the pressure was increased to $1x10^{-7}$ torr for a successive time duration amounting to dosages of 1,10,100,500 and 1000 Langmuirs (L). Exposure experiments were conducted over an emission current ranging from ~1pA to 5nA. The current was operated in a DC mode. The emission was set at the desired current and allowed to stabilize (less than 5% change). O_2 was then introduced and the extraction voltage was unchanged during the exposure. After exposure the emission was shut off while the system was pumped down to 10^{-9} torr. Energy distributions were obtained first at the current at which the exposure occurred, followed by an I-V sweep. Energy distributions were run with a pass energy of 5eV and a step size of 0.1eV over a kinetic energy range of 10-15V. All resulting FEED curves were fitted with EMG peaks using a peak fit program. Changes in the work function and the slopes of the resulting FN plots were then used to draw conclusions as to any mode of tip degradation.

The initial exposure experiments were done with 1nA emission current. Shown in figure 4.10 are the FEED and Fowler-Nordheim (FN) plots for a clean Mo tip exposed up to 1000L. All FEED curves could be fitted with only one EMG giving an average work

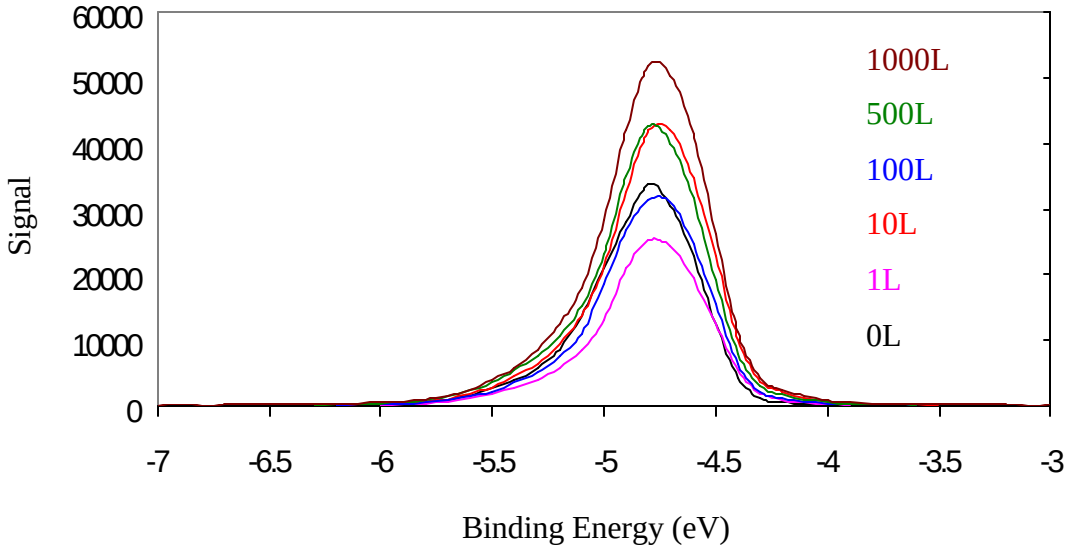

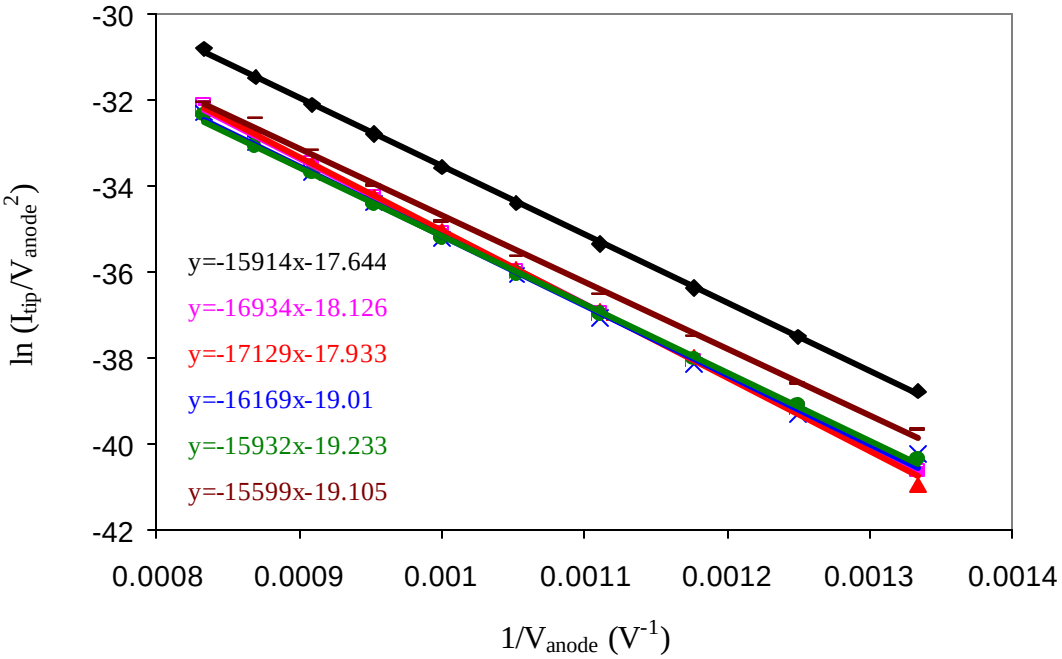

Figure 4.10 FEED and Fowler-Nordheim plots of clean Mo single tip exposed to O_2 at 1nA emission current.

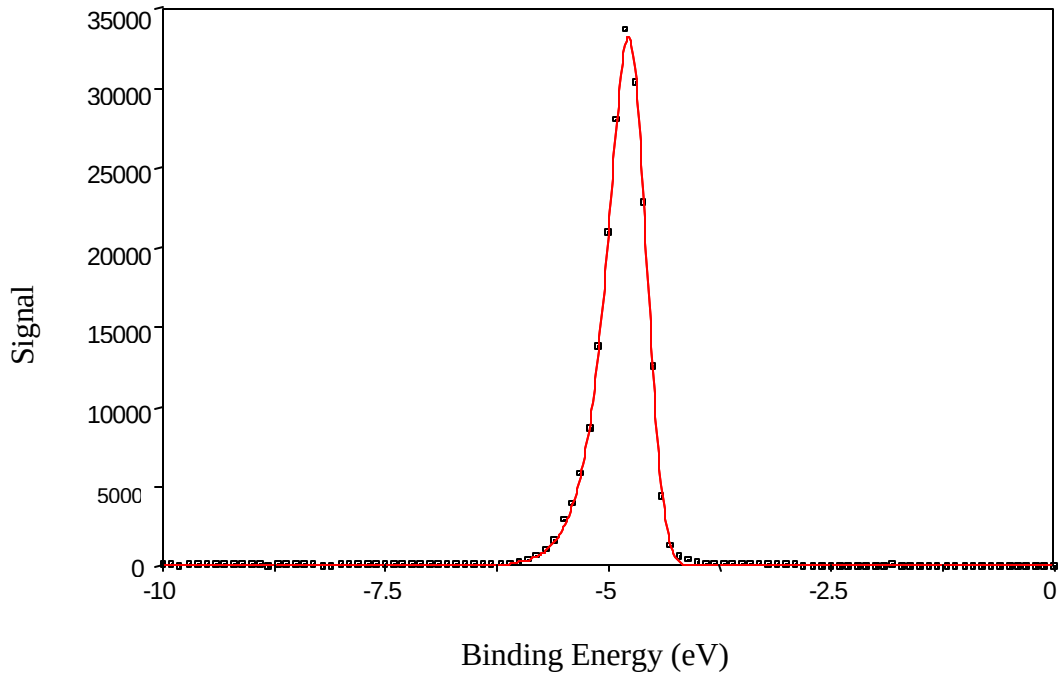

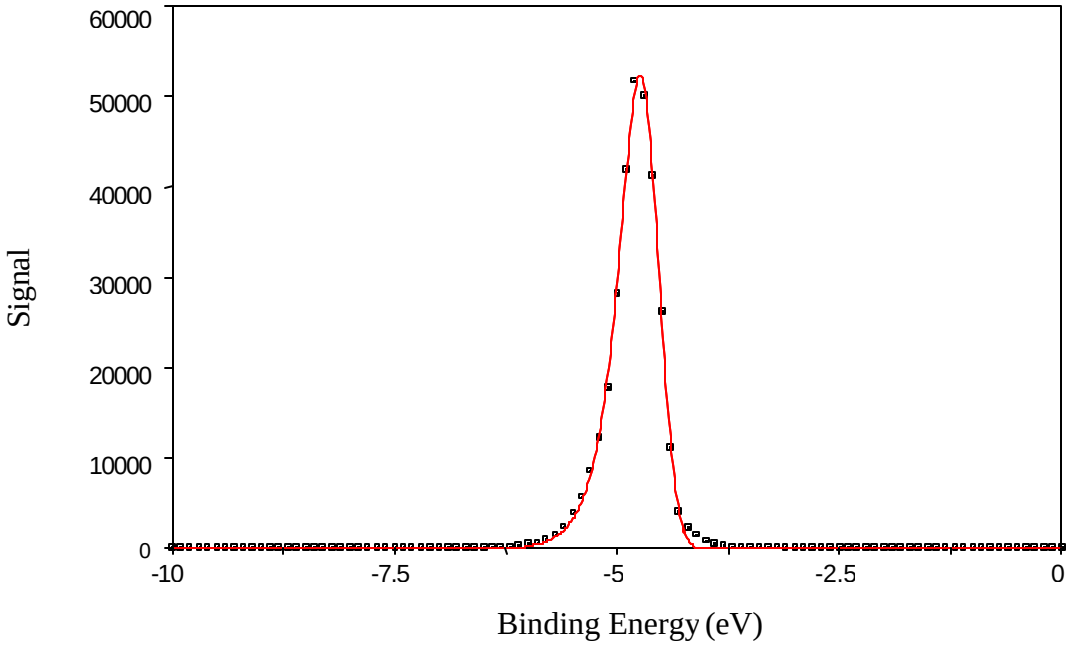

Figure 4.11 Peak fitted FEED curves for Mo single tip prior to O_2 exposure and after 1000L O_2 exposure at 1nA emission current.

function of 4.61eV. the fitted FEED curves of a clean Mo tip before and after exposure to 1000L of O_2 is shown in figure 4.11. Furthermore, the slopes of the FN plots showed no consistent change, with the largest difference being only 6.4%. To verify that the data results were conclusive three additional trials with different tips were conducted. All four trials indicated similar behavior, of which the first trial and the trial with the largest variation are listed in table 4.1. Both trials indicate that no significant effects on the emission behavior of the Mo tip occur under this emission current.

Increasing the emission current to 5nA while exposing the Mo tip to O_2 produced changes in the behavior of both FEED and FN plots. The resulting FEED and FN plots for this exposure are shown in figure 4.12. As the tip is continuously exposed to O_2 the intensity of the FEED signal continuously decreases until no signal is observed after 500L O_2. The work function only increases by 5% from 4.61eV to 4.85eV. On the other hand, the FN plots show large variations in the slopes and large deviations in the emission data points from the best fit lines. After 500L O_2, exposure the slope increases by 129% with respect to the slope of the Mo tip prior to O_2 exposures. Furthermore, after 1000L O_2, exposure irreversible damage occurs such that tip emission is not recoverable (FEED could not be retained even by increasing the extraction voltage). Oxidation of the emitter tip does not support the observed results since the thermal data showed that the degree of oxidation was noticeable by the degree of shifting in the energy spectrum. In this, case the FEED curves shift slightly while the signal intensity diminishes rapidly. In addition, the drastic change in the FN slopes can not be attributed to a work function change, which changes by only 5%. Finally the operating voltage

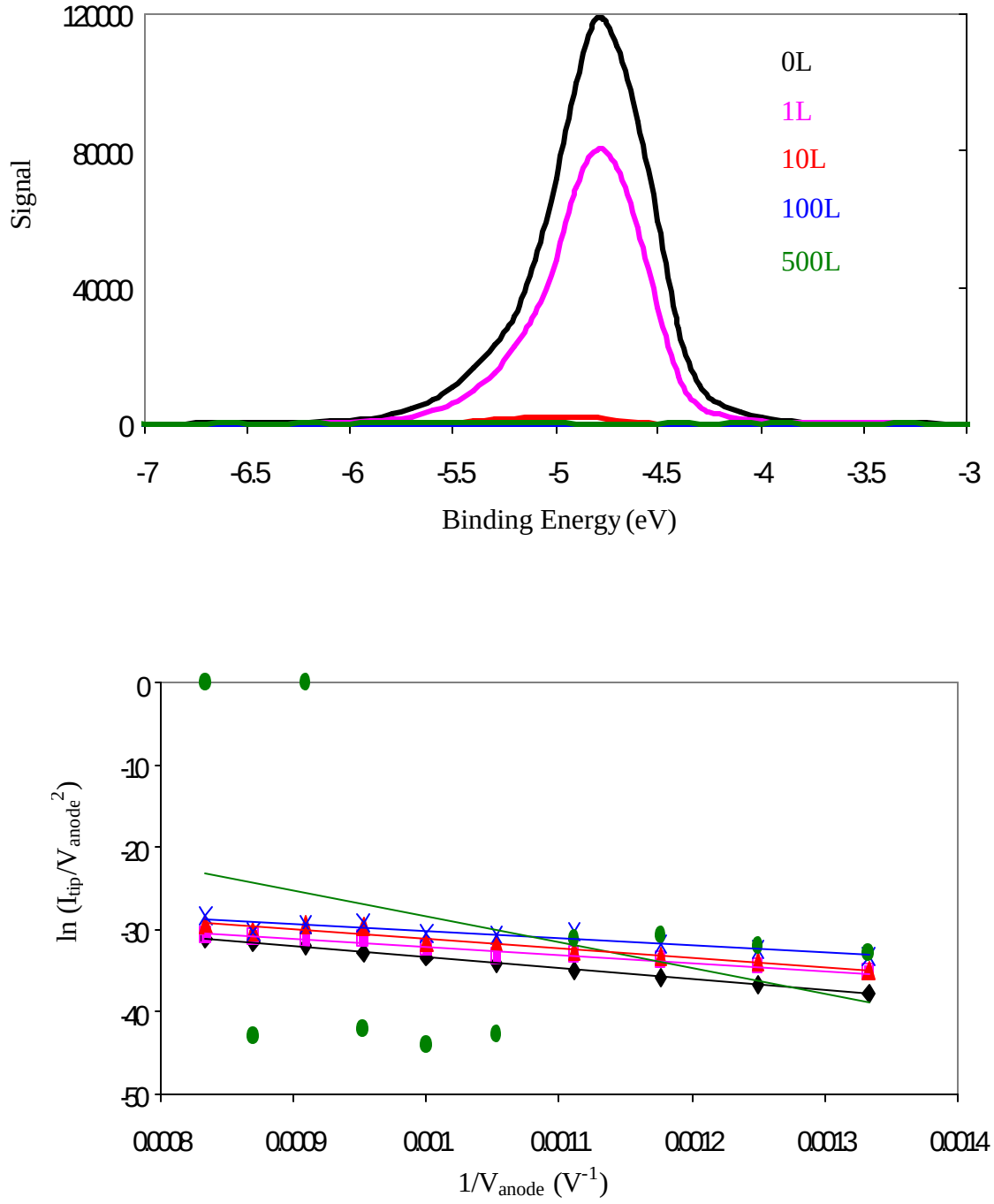

Figure 4.12 FEED and Fowler-Nordheim plots of Mo single tip exposed to O_2 at 5nA emission current.

produce 5nA emission sequentially decreases with O_2 exposure until failure occurred for which a slight work function increase would contradict, since an increase in the work function would require an increase in the field strength. These results support a sputter induced damage mechanism where the tip is gradually sharpened to the point of total ablation.

Emission experiments were also conducted with 10pA emission during oxygen exposure, and the results are listed in table 4.1. Much like the emission experiments conducted with 1nA emission, both the FEED and FN plots showed practically no variation. The emission current was therefore lowered to 1pA. At this current significant variations became noticeable upon further dosing. Figure 4.13 shows the FEED and FN plots obtained at this current level and the values of work functions and FN slopes are listed in table 4.1 for two distinct trials. Figure 4.14 shows a curve fit of a Mo tip exposed to 1000L O2. Both trials indicate similar features, the appearance of new peaks in the FEED and the fluctuations in the slopes of the FN plots. In the first trial the percent change in the slope is consistent with, and varies accordingly with, the change in the average work function. In the second trial the average work function does not change as much due to the contribution of a higher work function oxide. This oxide probably is produced by ion bombardment reduction of MoO_3 to MoO_2. The changes in the slopes do not vary consistently with the average work function, but this is most likely due to the scattering of some of the data points from which the linear fits are obtained. In any case, the fluctuations in the slopes and more importantly the appearance of new peaks in the FEED spectra are supportive of an oxide formation, which results in the instability of the

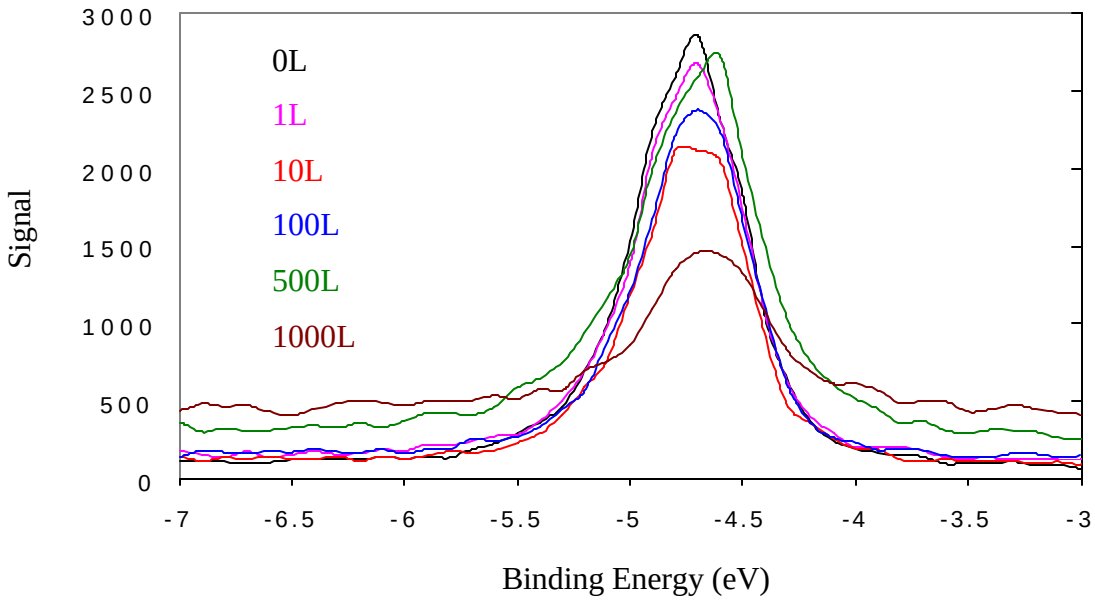

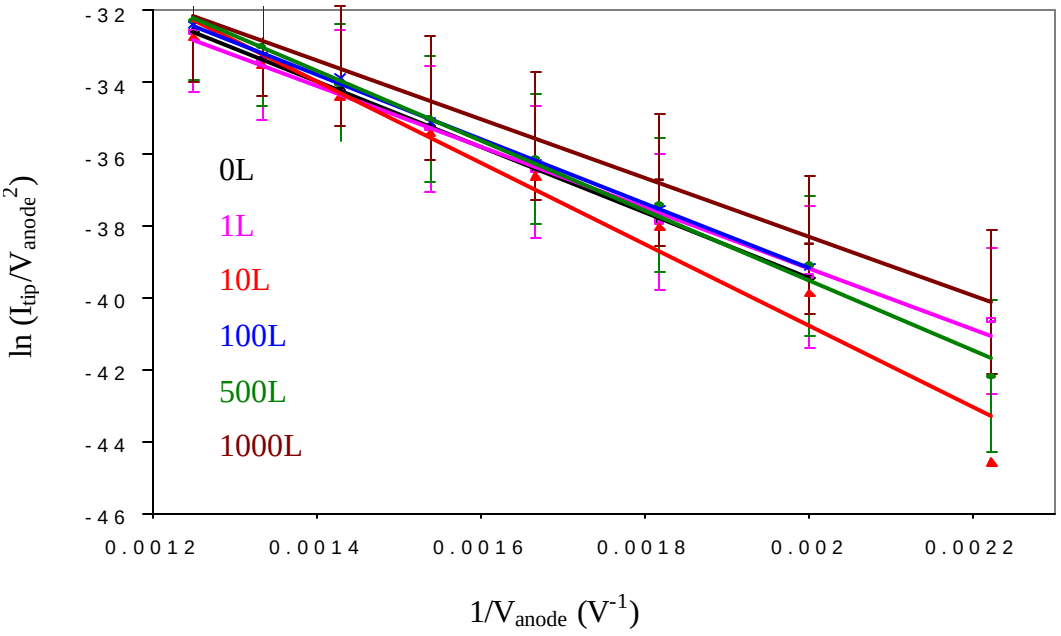

Figure 4.13 FEED and Fowler-Nordheim plots of clean Mo tip exposed to O_2 at 1pA emission current. Error bars on F-N plot represent a 5% error.

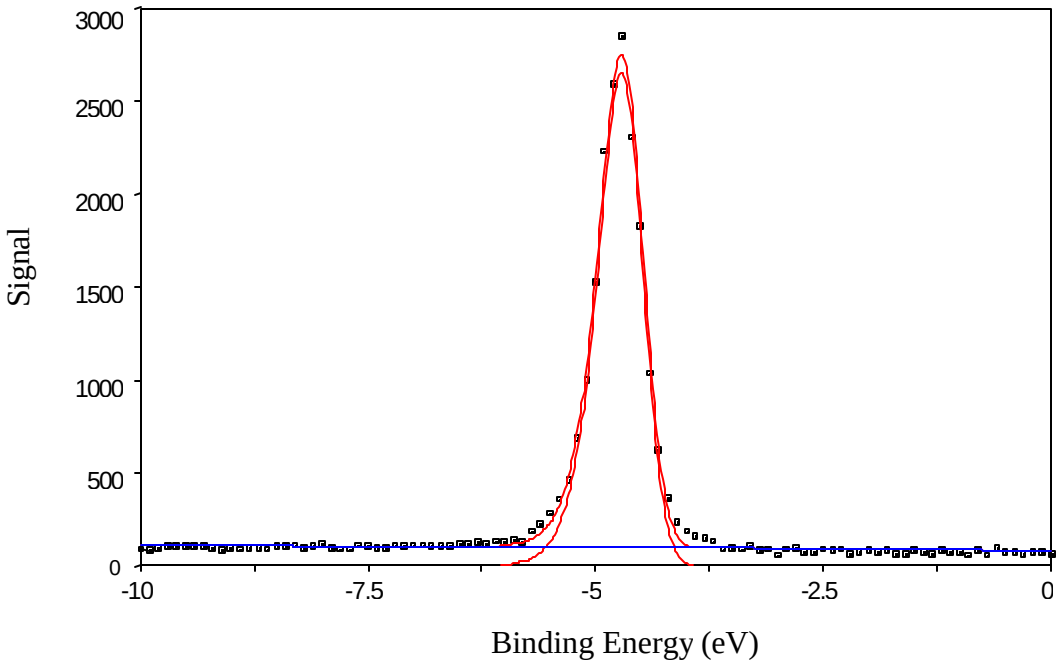

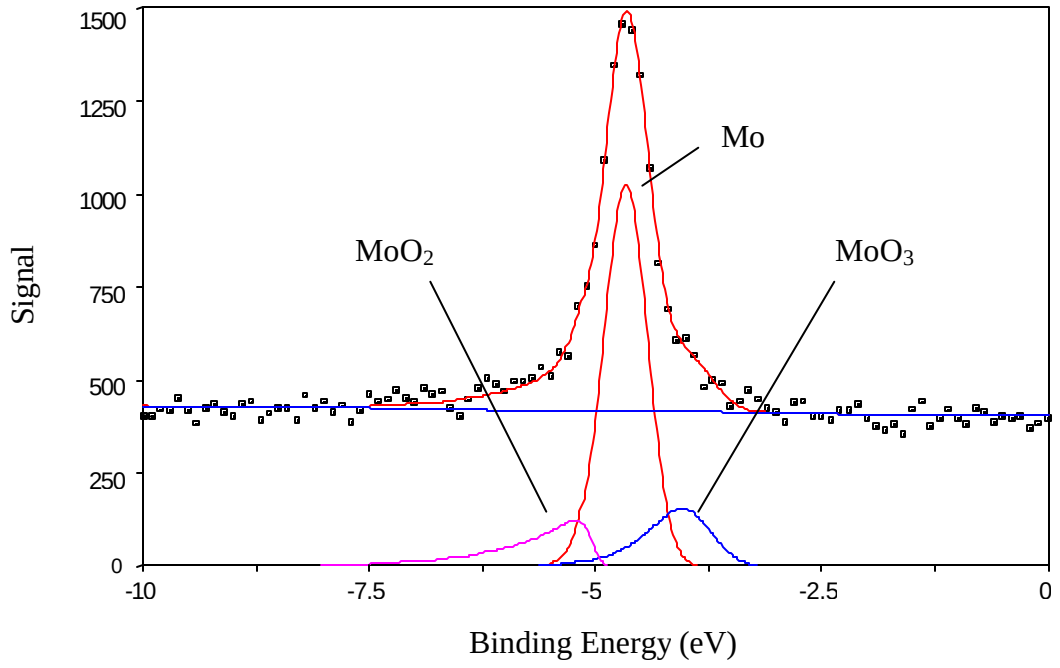

Figure 4.14 Peak fits of Mo tip exposed to O_2 at 1pA emission current for dosages of 0 and 1000 Langmuirs.

Current (nA)	Exposure (L)	FN slope	Intercept	Work Function (eV)	Percent Area of FEED	Average Work Function	% diff. in Work Function	% diff. in FN slope
1	0	-15914	-17.644	-4.63	100	-4.63		
	1	-16934	-18.126	-4.61	100	-4.61	-0.02	+6.41
	10	-17129	-17.933	-4.59	100	-4.59	-0.02	+1.15
	100	-16196	-19.010	-4.61	100	-4.61	+0.02	-5.61
	500	-15932	-19.237	-4.61	100	-4.61	0.00	-1.47
	1000	-15599	-19.105	-4.60	100	-4.60	-0.01	-2.09
1	0	-16280	-18.026	-4.67	100	-4.67		
	1	-16920	-18.431	-4.61	100	-4.61	-0.05	+3.93
	10	-15987	-19.874	-4.59	89.9			-5.51
				-4.08	10.1	-4.53	-0.08	
	100	-15479	-20.198	-4.51	96.6			-1.49
				-3.82	3.4	-4.49	-0.04	
	500	-17506	-19.003	-4.56	96.7			+11.2
				-3.90	3.3	-4.54	+0.05	
	1000	-16142	-20.116	-4.55	100	-4.55	+0.01	-7.79
5	0	-13711	-19.637	-4.61	100	-4.61		
	1	-9613.9	-22.513	-4.63	100	-4.63	+0.02	-35.1
	10	-11646	-19.471	-4.85	100	-4.85	+0.12	-16.3
	100	-8513.1	-21.677	no peak	-	-		-46.8
	500	-31461	-3.1490	no peak	-	-		+78.6
	1000	-	-	no peak	-	-		
0.01	0	-8823.1	-20.597	-4.64	100	-4.64		-
	1	-8997.2	-20.781	-4.60	100	-4.60	-0.04	+.197
	10	-9036.1	-20.696	-4.60	100	-4.60	0.00	+0.44
	100	-8934.3	-20.733	-4.60	100	-4.60	0.00	-1.13
	500	-8798.1	-20.352	-4.60	100	-4.60	0.00	-1.52
	1000	-8784.3	-20.530	-4.67	100	-4.60	0.00	-1.57
0.01	0	-9510.1	-19.556	-4.55	100	-4.55		
	1	-8718.0	-20.638	-4.55	100	-4.55	0.00	-8.31
	10	-8803.0	-20.272	-4.55	100	-4.55	0.00	+0.97
	100	-7964.0	-21.228	-4.57	100	-4.57	+0.02	-10.1
	500	-7883.7	-21.329	-4.64	85.1	-4.54	+0.03	-0.28
				-3.95	14.90			
	1000	-7733.1	-21.040	-4.64	100	-4.64	+0.10	-1.91
0.001	0	-7657.4	-22.270	-4.53	100	-4.53		
	1	-8241.6	-21.577	-4.55	100	-4.55	+0.02	+7.63
	10	-7553.6	-22.019	-4.46	100	-4.46	-0.09	-8.35
	100	-6333.9	-23.630	-4.27	100	-4.27	-0.19	-16.1
	500	-7140.5	-21.423	-4.47	79.6			+12.7
				-3.83	20.4	-4.34	+0.07	
	1000	-5943.3	-22.823	-4.39	62.8			-13.4
				-3.76	37.2	-4.16	+0.18	
0.001	0	-9191.8	-21.099	-4.59	100	-4.59		
	1	-8478.6	-22.214	-4.58	100	-4.58	-0.01	-7.76
	10	-11319	-18.143	-4.59	90.6		-0.03	+33.5
				-4.19	9.4	-4.55		
	100	-8983.7	-21.210	-4.55	86.0	-4.51	-0.04	-20.6
				-4.25	14.0			
	500	-9766.2	-19.989	-4.50	86.4	-4.43	-0.08	+8.71
				-3.98	13.5			
	1000	-8210.5	-21.902	-5.05	14.2	-4.52	-0.09	-15.9
				-4.58	69.5			
				-3.83	16.27			

Table 4.1 Effects of O_2 on the field emission behavior of clean Mo tips while operated at various emission currents ranging from 1pA to 5nA during the O_2 exposure. Here percent difference is between current exposure and prior.

emitter.

Emission experiments conducted on clean single Mo emitter tips in the presence of oxygen over a current range of 1pA – 5nA show three distinct regions. The first region occurs for emission currents below 10pA, where oxidation of the emitter tips is the primary source of emission instability. In the third region, for an emission current of 5nA or more, the emission instability is the result of sputter induced damage. In the second region, for currents between 10pA and 1nA, the emission shows stability. In this region the stability is most likely due to a counter effect of oxidation and ion bombardment. That is, as an oxide forms it is immediately removed by ion bombardment resulting in emitter stability.

4.5 Oxygen Exposure on Oxidized Mo Emitter Tips at Various Emission Currents

Since thermal experiments indicated that temperatures above 500 °C are required to achieve a clean emitter, oxygen exposures were preformed on oxidized Mo tips to achieve a clean emitter, oxygen exposures were performed on oxidized Mo tips to determine if results similar to the prior section could be observed. New tips were etched and rinsed with HF to remove the thick oxide platelets generally produced in the etching process. Tips were flashed at 900 °C if the FEED showed heavy oxidation, but were not completely cleaned. Once the energy distribution was located in the vicinity of the Mo work function, exposure experiments were initiated. All parameters such as step size, pass energy, etc. as used in the prior experiments were incorporated. The exposures were done for emission currents of 10pA, 1nA and 5nA.

Energy distributions and FN plots for an oxidized Mo tip operated at 1 nA while

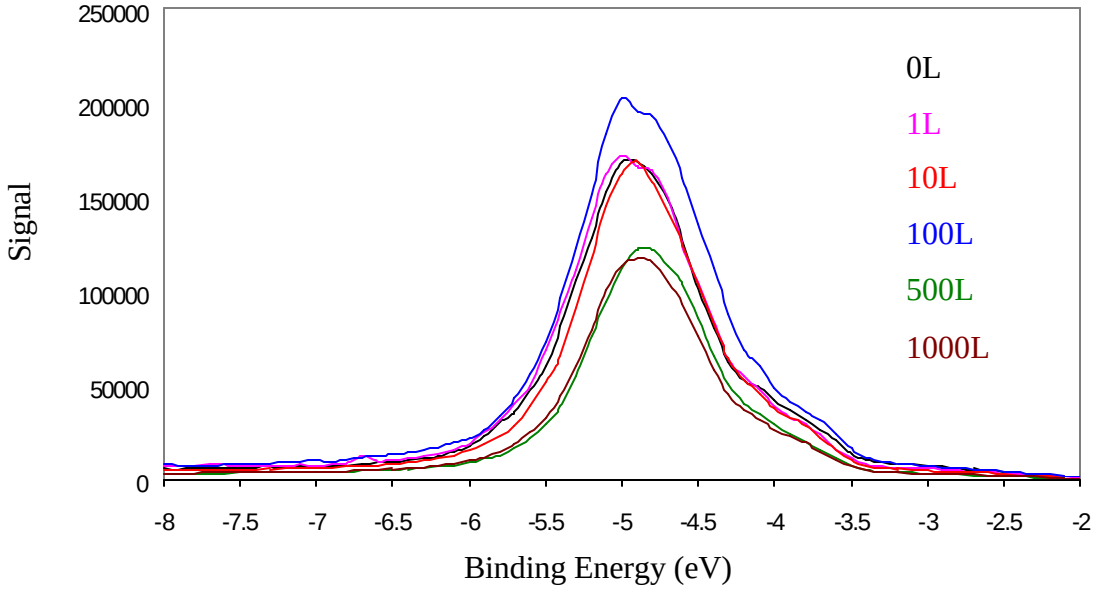

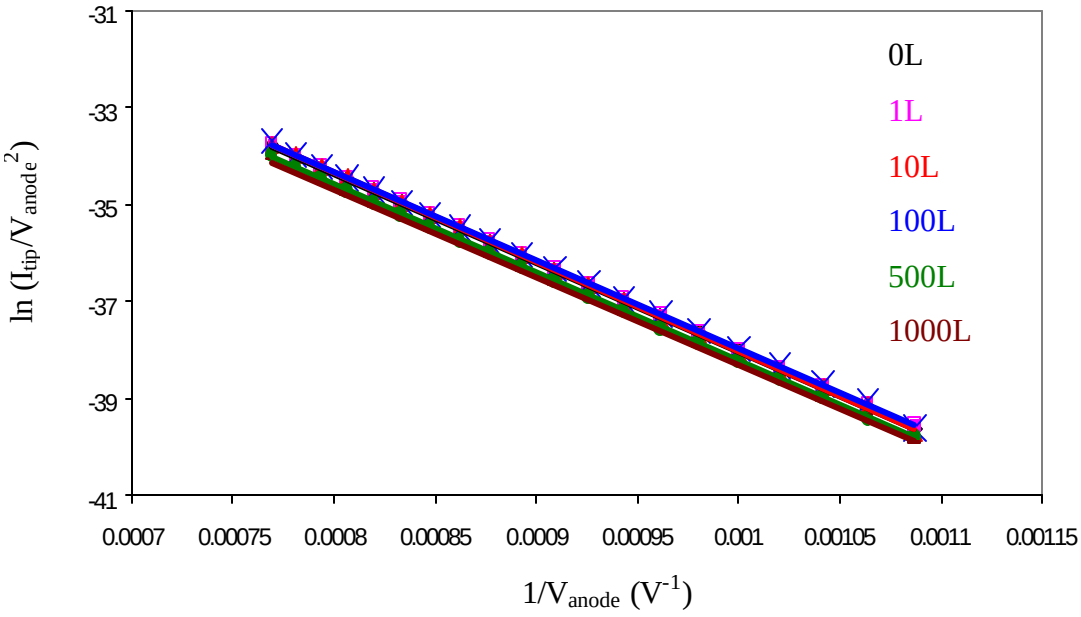

Figure 4.15 FEED and Fowler-Nordheim plots of an oxidized Mo tip exposed to O_2 at 1nA emission current.

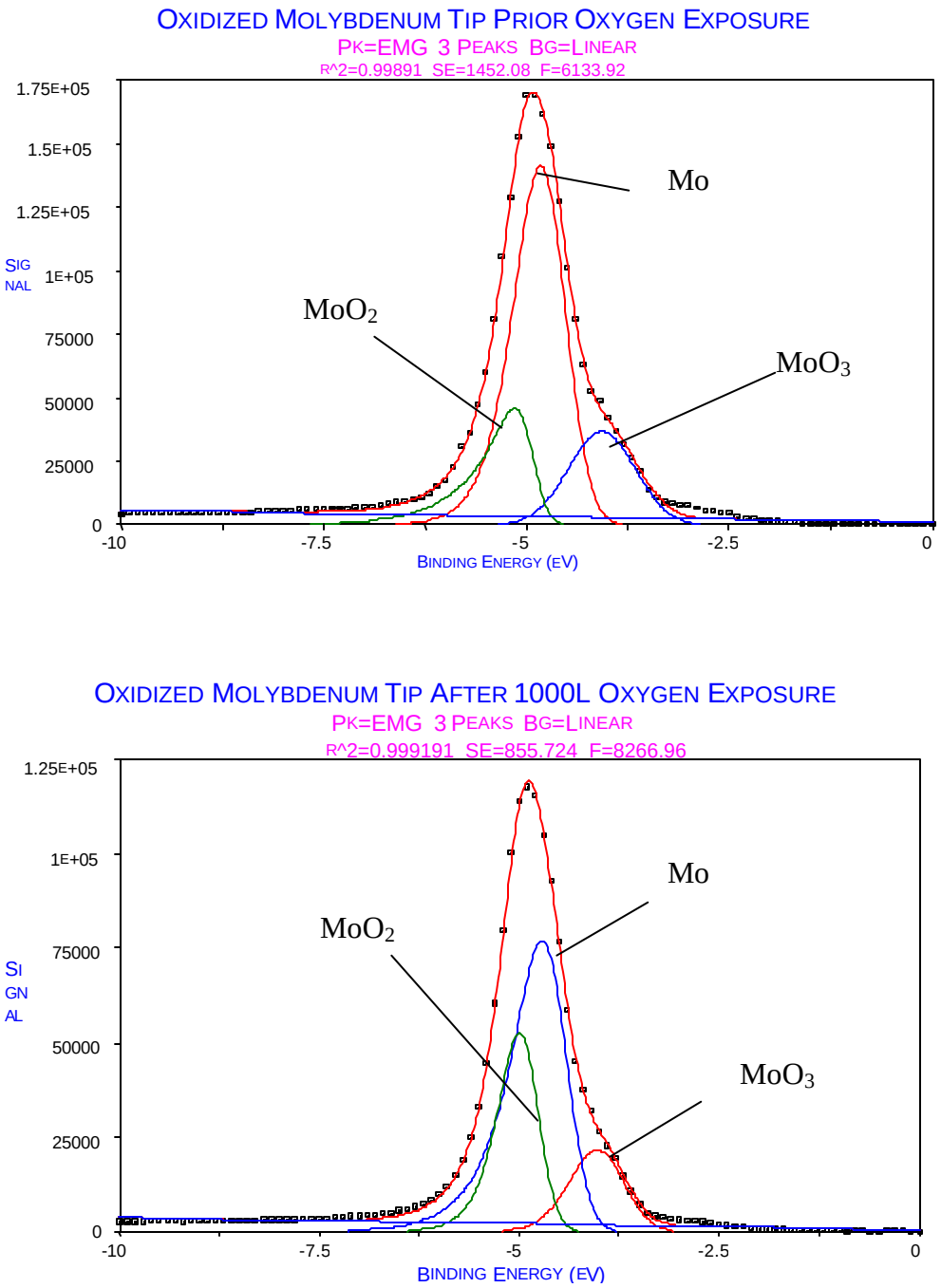

Figure 4.16 Peak fits of oxidized Mo tip exposed to O_2 at 1nA emission current for 0 and 1000 Langmuirs.

Current (nA)	Exposure (L)	FN slope	Intercept	Work Function (eV)	Percent Area of FEED	Average Work Function	% diff. in Work Function	% diff. in FN slope
0.01	0	-19195	-18.587	-5.42	52.9	-4.96	-	-
				-4.57	28.8			
				-3.83	8.3			
	1	-20074	-17.992	-5.39	64.1	-5.08	2.39	+4.58
				-4.65	29.3			
				-3.99	6.6			
	10	-18934	-19.207	-5.35	59.8	-5.03	1.00	-5.68
				-4.64	33.8			
				-3.98	6.4			
	100	-18898	-19.446	-5.52	48.0	-5.01	0.40	+.019
				-4.59	46.8			
				-4.09	5.2			
	500	-19948	-19.823	-5.52	60.3	-5.23	4.30	+5.56
				-4.84	37.5			
				-4.03	2.2			
	1000	-19780	-19.173	-5.49	47.5	-5.03	3.90	-0.84
				-4.63	48.0			
				-4.28	4.4			
1	0	-18318	-199.719	-4.97	20.3	-4.58	-	-
				-4.65	60.6			
				-3.97	19.1			
	1	-18276	-19.727	-4.92	33.5	-4.56	0.44	-0.23
				-4.55	48.7			
				-3.90	17.8			
	10	-18470	-19.566	-4.88	23.8	-4.51	1.10	+1.06
				-4.54	61.8			
				-3.76	14.4			
	100	-18152	-19.816	-4.88	30.3	-4.48	0.67	-0.68
				-4.57	52.1			
				-3.82	17.6			
	500	-18191	-20.042	-4.84	25.1	-4.46	0.45	+0.21
				-4.46	59.5			
				-3.85	15.5			
	1000	-18636	-20.258	-4.85	28.0	-4.50	0.89	-0.85
				-4.49	57.1			
				-3.88	14.9			
5	0	-18078	-22.045	-5.27	51.6	-5.15	-	-
				-5.08	43.0			
				-4.53	5.4			
	1	-17590	-22.724	-5.22	32.5	-5.05	1.96	-2.70
				-5.02	57.3			
				-4.68	10.2			
	10	-19983	-21.311	-5.15	59.6	-4.96	1.78	+13.6
				-4.94	40.4			
	100	-18810	-24.125	-5.45	40.5	-5.31	6.82	-5.87
				-5.22	59.5			
	500	-19618	-24.315	-6.19	49.0	-5.83	9.33	+4.30
				-5.50	51.0			
	1000	9935.7	-35.052	no peak	no peak	-	-	-49.35

Table 4.2 Effects of O_2 on the field emission behavior of oxidized Mo tips while operated at various emission currents ranging from 1pA to 5nA during the O_2 exposure.

under the influence of O_2 is shown are figure 4.15. All FEED curves were fitted using 3 EMG curves, which can be assigned to Mo, Mo_2 and MoO_3, those for 0L and 1000L O_2 exposure are shown in figure 4.16. The values for work functions of the individual curves and their contributions are listed in table 4.2. The Fowler-Nordheim plots indicated that the emission is highly stable as the slopes almost perfectly overlap with a deviation of only 1%. The average work function given as the sum of the individual contributions(i.e. $\sum \phi_i x_i$), can be taken as the overall work function over an integrated surface. The FEED results also indicate stability since the average work function shows a maximum change of only 2%. Both results therefore indicated that at 1nA the emission characteristics of an oxidized Mo tip remain unaltered during operation in oxygen.

A similar experiment was conducted with an emission current of 10pA on a different oxidized tip. Both the FEED and Fowler-Nordheim data are presented in figure 4.17 and the fitting values are again listed in table 4.2. Under this condition the average work function deviates by at most 5%, and the slopes of the FN plots by ~ 6%. Again this can be interpreted as stable emission, and is identical to the results at this current for a clean emitter surface. On the other end of the stability region a current greater than 1nA showed degradation for a clean Mo tip. Therefore exposure on an unclean Mo tip was executed on a different tip. Figure 4.18 shows the FEED and FN results for exposure conducted at 5nA emission current while individual data is listed in table 4.2. Exposure at this particular current produces some interesting results. First the slopes of the FN plots exhibit a large deviation after 1000 L of O_2 dosing. Secondly, the FEED curves show an initial cleaning of the tip by a shifting to lower binding energies,

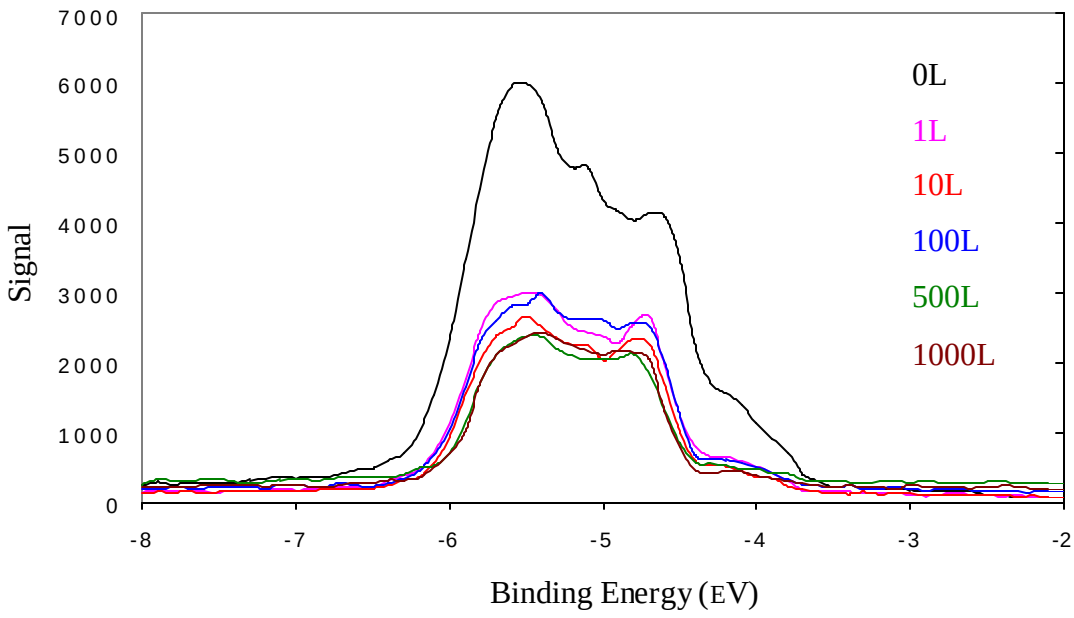

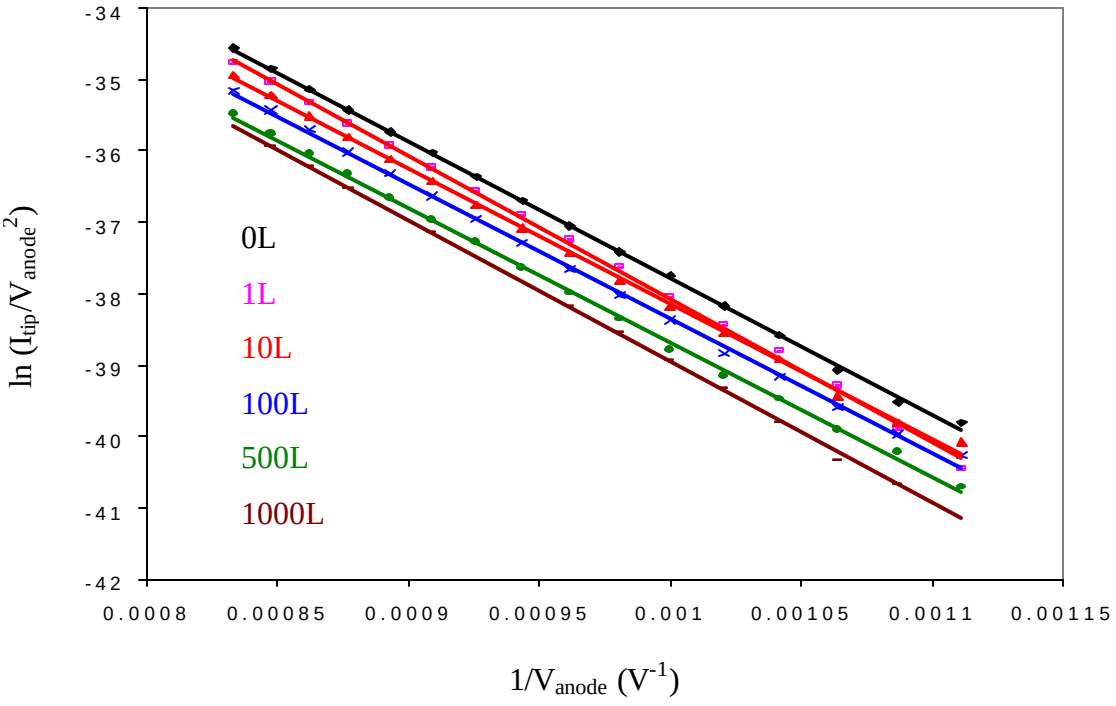

Figure 4.17 FEED and FN plots of oxidized Mo tip exposed to O_2 at 10 pA emission current

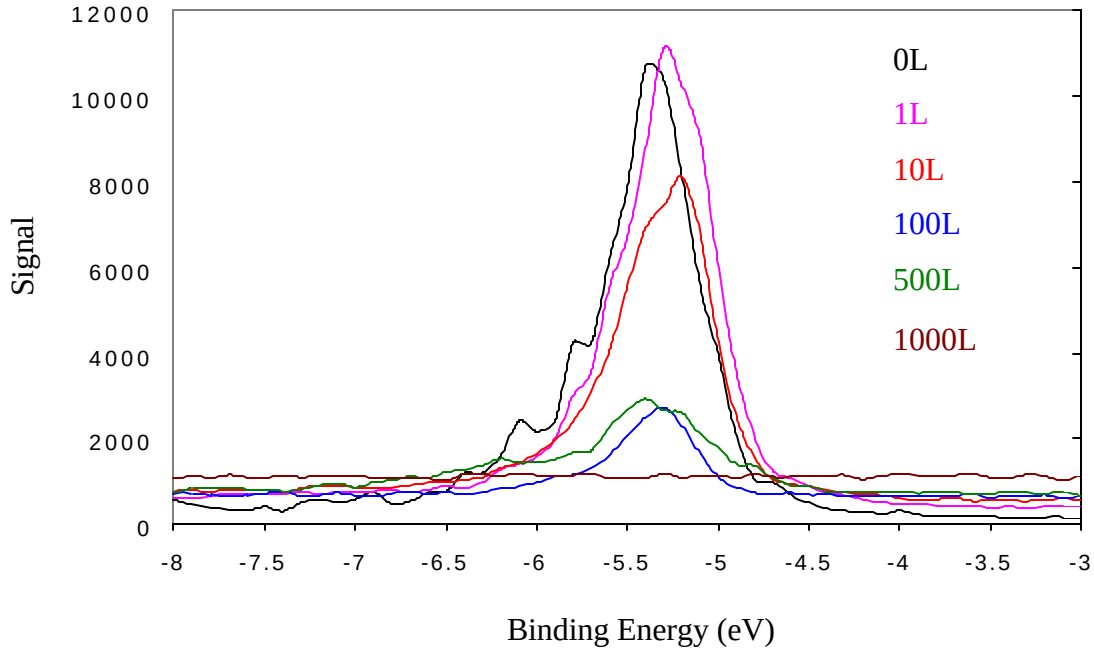

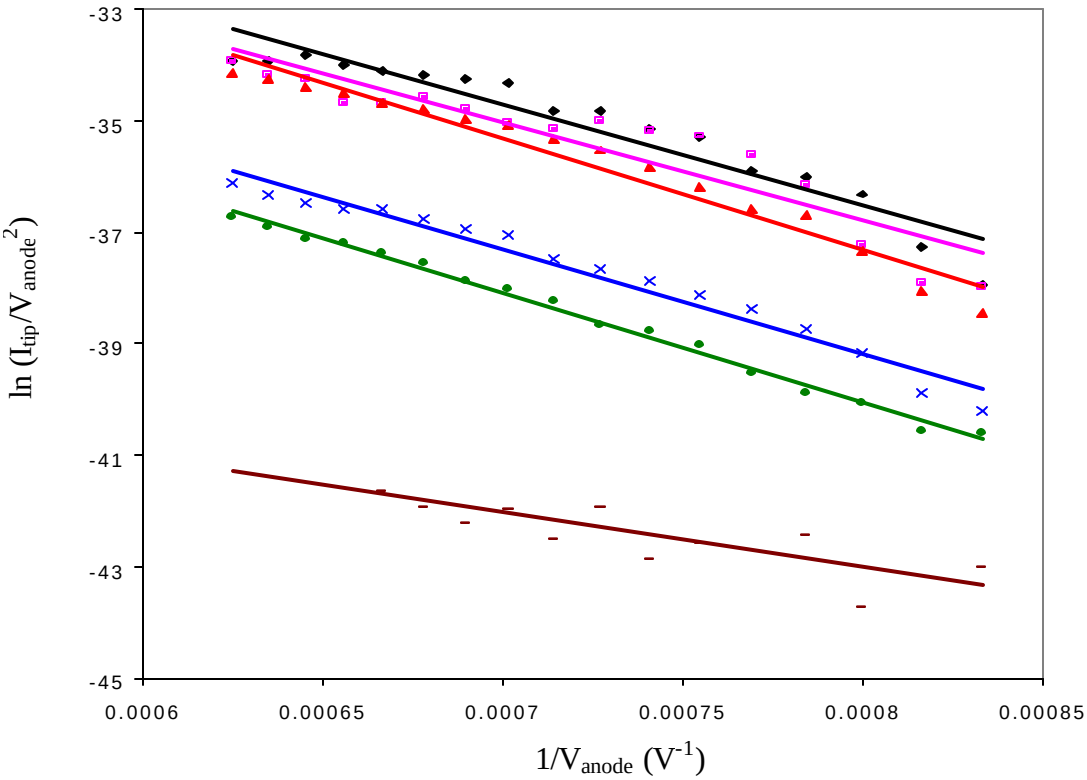

Figure 4.18 FEED and FN plots of oxidized Mo tip exposed to O_2 at 5nA emission current (colors correspond with above dosages in the FN plot).

followed by a rapid deterioration in the signal intensity. In addition, the voltage on the extraction anode had to be increased in the later dosages to obtain 5nA emission. Finally the lower energy peaks disappear with only the higher energy peaks being retained, resulting in a higher average work function. These effects can also be explained by a sputtering mechanism similar to that seen for a clean Mo tip. Initially the tip is cleaned by ion bombardment; however, further sputtering appears to reduce MoO_3 to MoO_2, which would explain the increase in the average work function. Eventually the tip becomes blunt at the apex and emission may be due to protrusions along the shank of the wire.

Oxidized Mo tips exhibit similar behavior to clean emitter tips indicating that field emitters can be operated within a specific current regime under which stable emission may be achieved. However, clean Mo tips show less instantaneous current fluctuations due to the absence of the oxide.

4.6 Effect of Oxygen Exposure on Mo Arrays

Molybdenum arrays used in this study were fabricated by LETI (LETI-CEA Technologies Advances, Grenoble, France) [22]. Arrays were fabricated on a $1cm^2$ soda lime glass substrate 1mm in thickness. The dimension of the emitting area was 20 mm^2 and confined to the center of the substrate. Spindt type tips are arranged in a 4x4 mesh array, with each square mesh measuring 50µm x 50µm, thus containing $\approx 2.8x10^6$ individual emitters over the entire emission area [23]. Arrays were operated in a triode mode with a fixed voltage on the emitter (cathode) and on the anode. The gate voltage is swept or varied in order to obtain an IV curve. To obtain FEED curves the cathode was biased with –90V. The array was mounted in Vespel block, which was electrically

isolated, and connection to the cathode and gate were made with insulated wire via two feedthroughs. Prior to oxygen introduction, emitter arrays were seasoned [24] by operating at 1.5mA for a period of 12-15 hours. Once the emission current showed little fluctuation (< 5%) and the FEED remained unchanged, the exposure to oxygen was initiated. Oxygen exposures were conducted under two modes of operation. In the first mode the cathode was negatively biased, as was the gate. In the other mode the cathode was grounded while the gate was positively biased.

The first set of oxygen exposures on Mo arrays was done in the negatively biased mode. The array was set at a total emission current of 400μA as measured at the cathode. This current was acquired by setting the voltage on the cathode to –90V and adjusting the gate voltage between –10 and –13V. The array was set at this particular current prior to O_2 introduction and no adjustments were made during exposure. Figure 4.19 shows the energy distribution of field emitted electrons, along with the corresponding FN plots, exposed up to 1000L O_2 under the negative mode of operation. Three different trials were conducted under this mode of operation, but only the results of the data with the largest deviations are depicted. The appearance of a high energy tail that extends beyond 10eV indicates that the array is under going oxidation. however, The slopes of the FN plots decrease, which would contradict an increase in the work function of the emitter. The continuous increase in the intercepts of the FN plots indicates that the emission density is increasing. Activation of new emission sites by field desorption or sputter cleaning would explain the intercept values and the extending energy tail, but not the decrease in slopes. Oxidation sharpening [26] of the emitter tips could also cause similar

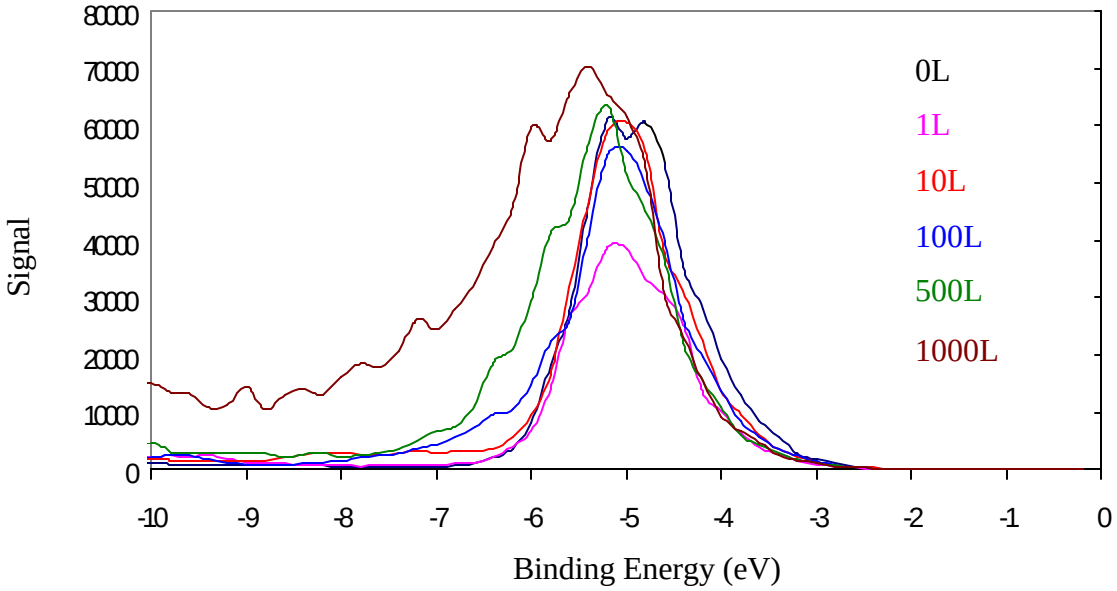

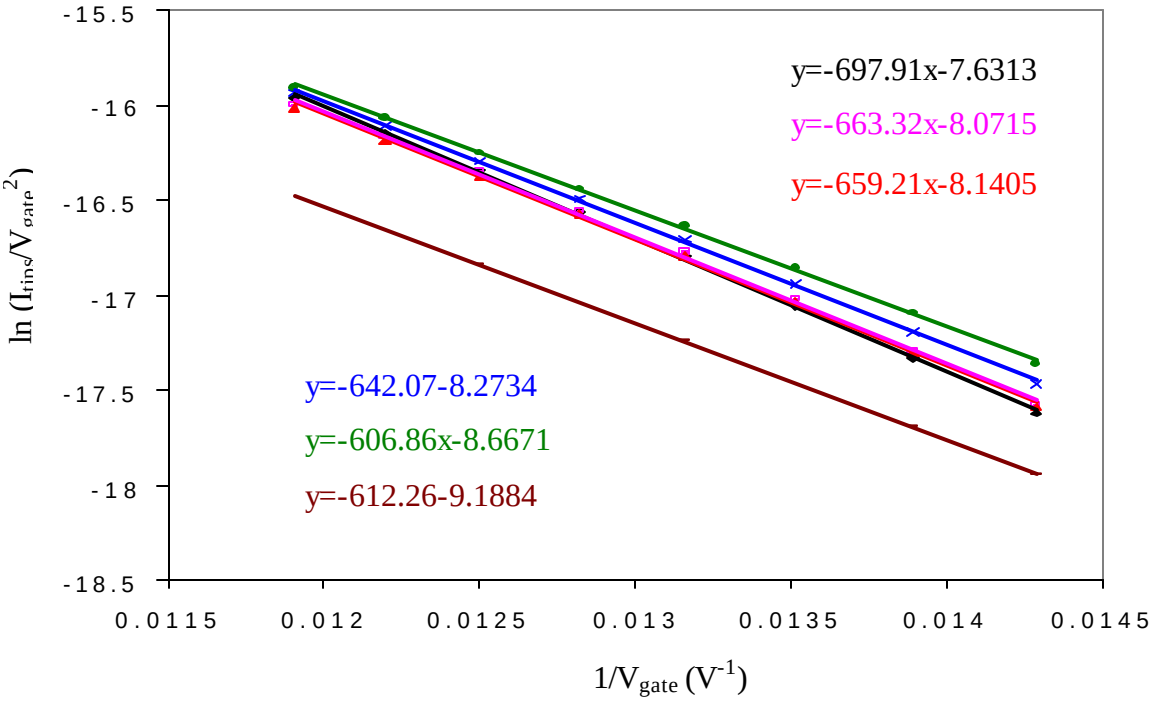

Figure 4.19 FEED and FN plots of Mo array operated at 400µA emission current with –90V on cathode while being exposed to O_2. (Colors in F-N plot correspond to those in the energy distribution plot.)

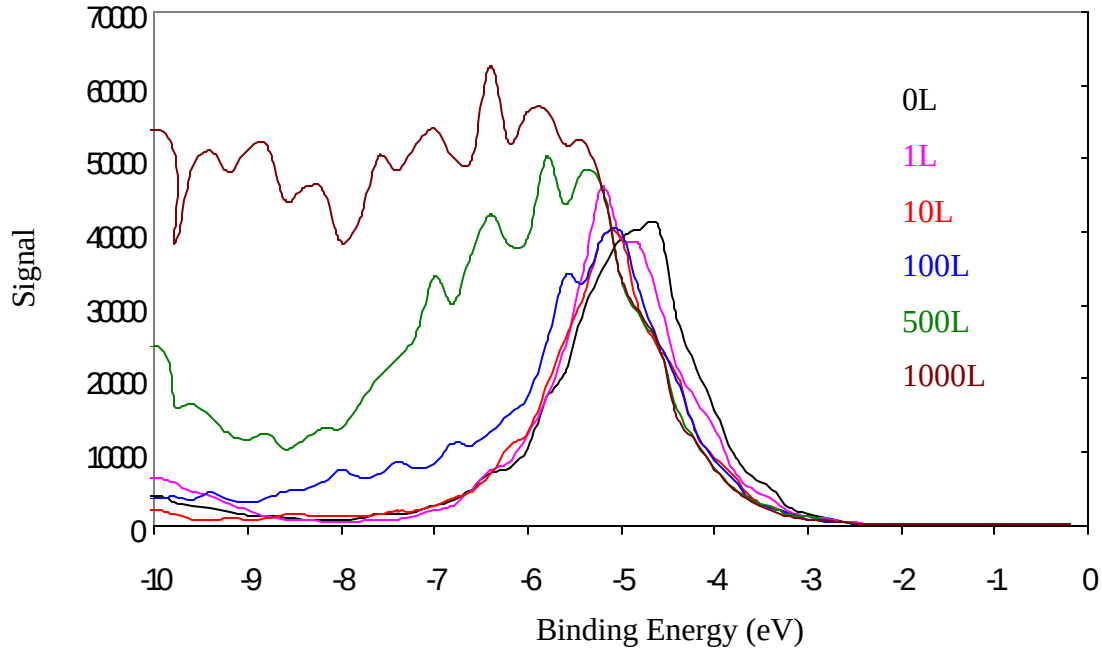

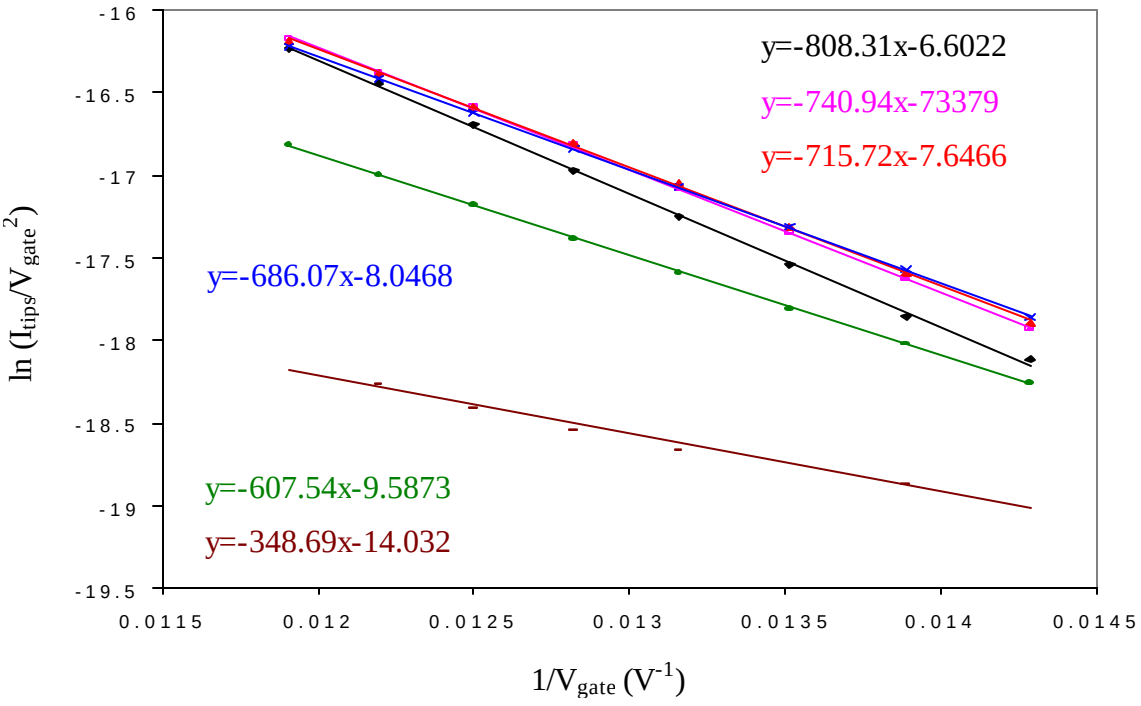

Figure 4.20 FEED and FN plots of Mo array operated at 400μA emission current with cathode grounded while exposed to O_2. (Colors in F-N plot correspond to those in the energy distribution plot).

behavior in the emission data, but would not explain the disappearance of the low energy oxide. A more likely explanation is that the tips are ion bombarded causing the reduction of MoO_3 protrusions to MoO_2 protrusions along with sputtering of Mo and MoO_2 sites, which results in sharpened tips. Ion bombardment may also result in the formation of new nano-protrusion sites, which as the exposure time increases, become oxidized. These new sites explain the increase in the FN intercepts. The sharper oxide protrusions would account for the lower slopes as well as the extended tail. Even though the emission sites are oxidized, their sharpness dominates over the work function increase resulting in a smaller slope value.

Arrays operated with grounded tips show much larger effects in both the FEED and FN plots. Figure 4.20 show both FEED and FN plots for an array operated under this condition. Under this condition both the cathode and anode were grounded while a positive voltage was placed on the gate during O_2 exposure. As in the prior experiments the array emission current was set at a total of 400μA emission during the exposure experiment. FEED and IV data were obtained in a similar fashion as those when the cathode was negatively biased. Two distinct differences are evident. In the FEED curves, a higher extent of oxidation is seen throughout the exposure. The FN plots also show much larger deviations in both the slopes and intercepts. The slopes vary by as much as 57% compared to only 13% when the array is operated in the negative bias mode. In both cases, however, an apparent initial cleaning of the array can be observed in the low binding energy shoulder. A sputtering-oxidation mechanism may also help explain these results and is described below.

At this particular current, the current per tip can be calculated between two extremes, that in which all emitters are active and that in which only 10% of them are active. For these extremes the emission per tip can range from as low as 1.33×10^{-10}A to as high as 8×10^{-10}A. For Mo single tips emission stability was observed at this current range when tips were exposed to oxygen; however, certain differences exist. First the inter-cavity between the gate and the cathode limits the pumping speed by which O_2 can be evacuated from the local region of the emitter. Second the emission is over a larger area such that probability of electron impact ionization of a gas molecules is different. Finally the emitter tip geometry is smaller such that it is more sensitive to ion bombardment. Taking these facts into account the following sputtering-oxidation mechanism may justify the emission data. Ion bombardment is consistently occurring under both conditions as is seen by the initial cleaning of the tip (disappearance of the low work function oxide). This bombardment causes existing emitting protrusions to be sharpened, as well as new protrusions, to be formed. This results in the decrease of the slopes and the increase in the intercepts. When the cathode is negatively biased the bombardment is enhanced. As the existing tips are sharpened, they are also being oxidized by surrounding O_2 or O_2^+; however, this oxide is at the same time being ablated. Over time the oxidation rate exceeds the ablation rate, thus resulting in the high binding energy tail that develops at higher dosages. In addition, as new protrusions are being formed they are being ablated away by bombardment, which accounts for the smaller gradual increase in the intercepts. When the cathode is grounded on the other hand, the oxidation rate more greatly exceeds the sputtering rate, which in turn produces a more

rapid increase in the high binding energy tail. Furthermore the rate of ablation of new protrusions is slower resulting in an increase of emission sites, which is indicated by the more rapid increase in the intercepts. These new sites are sharper than the existing sites, but become oxidized, yet are more likely to contribute to the overall emission. That is, as oxidation proceeds, the old sites become deactivated and the new sharper oxidized sites dominate the emission behavior. If this were indeed the case, it would be expected that increasing the emission current would result in higher stability; unfortunately, due to a limited supply of arrays this hypothesis could not be completely examined.

4.7 Conclusions

XPS and UPS was performed on Mo flat samples comprised of 1 cm^2 Mo foil, while tips were formed from Mo wire. Thermal experiments on both flat and tip samples showed that the heating of the Mo surface to 450 °C is not sufficient to reduce the oxide layer to clean Mo metal. In fact, at this particular temperature, the predominant oxide is MoO_2 which is a higher work function oxide. Therefore, heating an array to this temperature would not be beneficial. Only when the Mo surface is heated above 750 °C can it be reduced to the pure metal.

FEED experiments on both clean and oxidized tips showed that these tips could be operated in the presence of O_2 without any substantial degradation when operated at currents between 10pA and 1nA. For clean tips degradation in the field emission was observed for emission currents of 1pA and 5nA. For the 1pA emission current, the tip is oxidized when operated in the presence of O_2. For both clean and oxidized tips exposed to O_2 while operated at 5nA emission current, degradation was also observed. In this

case the degradation in the field emission is the result of the tip being continuously sputtered away. It was thus suggested that in the regime between 10pA and 1nA, the effect of oxidation is countered by the effect of sputtering, thereby producing stable emission.

FEED experiments were also conducted on a Mo array operated in the presence of oxygen. The experiments showed that when the cathode was operated with a negative applied voltage the array emission was less effected by O_2. When operated in this mode the sputtering effect is more enhanced, in which case oxidation occurred at a slower rate. Here again the results indicated that the array could probably be successfully operated in O_2 if the emission current per tip could be regulated. It was not determined at what total emission current for this particular array successful emission behavior could be accomplished.

References:

1. J.M. Bernhard, Ph.D. Thesis, University of North Texas 1999.
2. Handbook of X-ray Photoelectron Spectroscopy. Perkin-Elmer Corporation. Physical Electronics Division, Eden Prairie, MN 55344.
3. D. Briggs and M.P. Seah, *Practical Surface Analysis*, John Wiley & Sons, Ltd., New York 1983.
4. G.H. Smudde, Jr., P.C. Stair, Surf. Sci., **317**, 65 (1994).

5. C.A. Spindt, I. Brodie, L. Humphrey, E.R. Westerberg, J. Appl. Phys. **47**, 5248 (1976).
6. C.A. Spindt, C.E. Holland, I. Brodie, IEEE Trans. Electron Devices **38**, 2355 (1991).
7. F.A. Cotton, G. Wilkinson, *Advanced Inorganic Chemistry, 4th ed.*, John Wiley & Sons Inc., New York 1980.
8. P. Arnoldy, J.C.M. de Jonge, J.A. Moulijn, J. Phys. Chem. **89**, 4517 (1985).
9. H.M. Kennet, A.E. Lee Surf. Sci. **48**, 591 (1975).
10. Ambrosio A. Rouse, Thesis (PhD.), University of North Texas 1999.
11. Shang Lin Wang, Phys. Rev. Lett. **38**, 434 (1977).
12. R.C. Cinti, E. Al Khoury, B.K. Chakraverty, N.E. Christensen, Phys. Rev. **B14**, 3296 (1976).
13. J.W. Rabalais, Richard J. Cotton, Chemical Phys. Lett., **29**, 131 (1974).
14. J.M. Bernhard, A.A. Rouse, E.D. Sosa, B.E. Gnade, D.E. Golden, Rev. Sci. Instrum. **70**, 3299 (1999).
15. R. Riwan, C. Guillot, J. Paigne, Surf. Sci. **47**, 183 (1975).
16. E. Bauer and H. Poppa, Surf. Sci. **88**, 31 (1979).
17. J. Muller, Surf. Sci. **69**, 708 (1977).
18. P.A. Spevack, N.S. McIntyre, J. Phys. Chem. **96**, 9029 (1992).
19. CRC Handbook of Chemistry and Physics 73rd edition, CRC Press Inc., 2000 Corporate Blvd., N.W., Boca Raton, FL 33431.

20. B.R Chalamala, R.M. Wallace, B.E.Gnade, J. Vac. Sci. Technol. B. **16**, 2859 (1998).

21. Y. Gotoh, K. Utsumi, M. Nagao, H. Tsuji, J. Ishikawa, T. Nakatani, T. Sakashita, K. Betsui, J.Vac. Sci. Techol. B **17**, 604 (1999).

22. T. Utsumi, J. Soc. Infor. Disp. **1/3**, 313, (1993).

23. B. R. Chalamala, Thesis (PhD.), University of Noth Texas 1996.

24. V.T. Binh, N. Garcia, S.T. Purcell, Advances in Imaging and Electron Physics, **95**, 74 (1996).

25. T.S. Ravi, R.B. Marcus, D. Liu, J. Vac. Sci. Technol. B, **9**, 2733 (1991).

CHAPTER 5

EMISSION CHARACTERISTICS OF CARBON NANOTUBES

5.1 Introduction

Carbon nanotubes have prompted large interest as a field emitter candidate due to their unique geometry. The radius of curvature for carbon nanotubes varies from ~2nm for single-walled nanotubes (SWNT) and up to 50nm for multi-walled nanotubes MWNT). Nanotubes have also been reported to have lower work functions than that of graphite, and vary depending on the type and degree of purity. In this chapter the characterization and emission properties of both single-walled and multi-walled nanotubes will be presented. The nanotubes were characterized using scanning electron microscopy (SEM), X-ray photoelectron spectroscopy (XPS) and X-ray diffraction (XRD). The work functions were obtained from ultra-violet photelectron spectroscopy (UPS) and field emission.

5.2 Sample Preparation and Characterization

In this study both MWNT and SWNT were investigated. Both flat samples and tips were prepared by pressing nanotube mats onto Mo foils or wires. Electron micrographs were used to view surface morphology and determine which tips would be used for field emission experiments. Figure 5.1 displays SEM micrographs taken of flat and tip MWNT and SWNT samples. SEM is not of high enough resolution to observe individual tubes; however, ropes or bundles of tubes are evident. Isolated ropes are more

clearly seen in the MWNT samples, most likely due to their reported larger diameters. In any case, these carbon tubes provide much sharper geometry's than could be obtained from chemical etching of Mo tip.

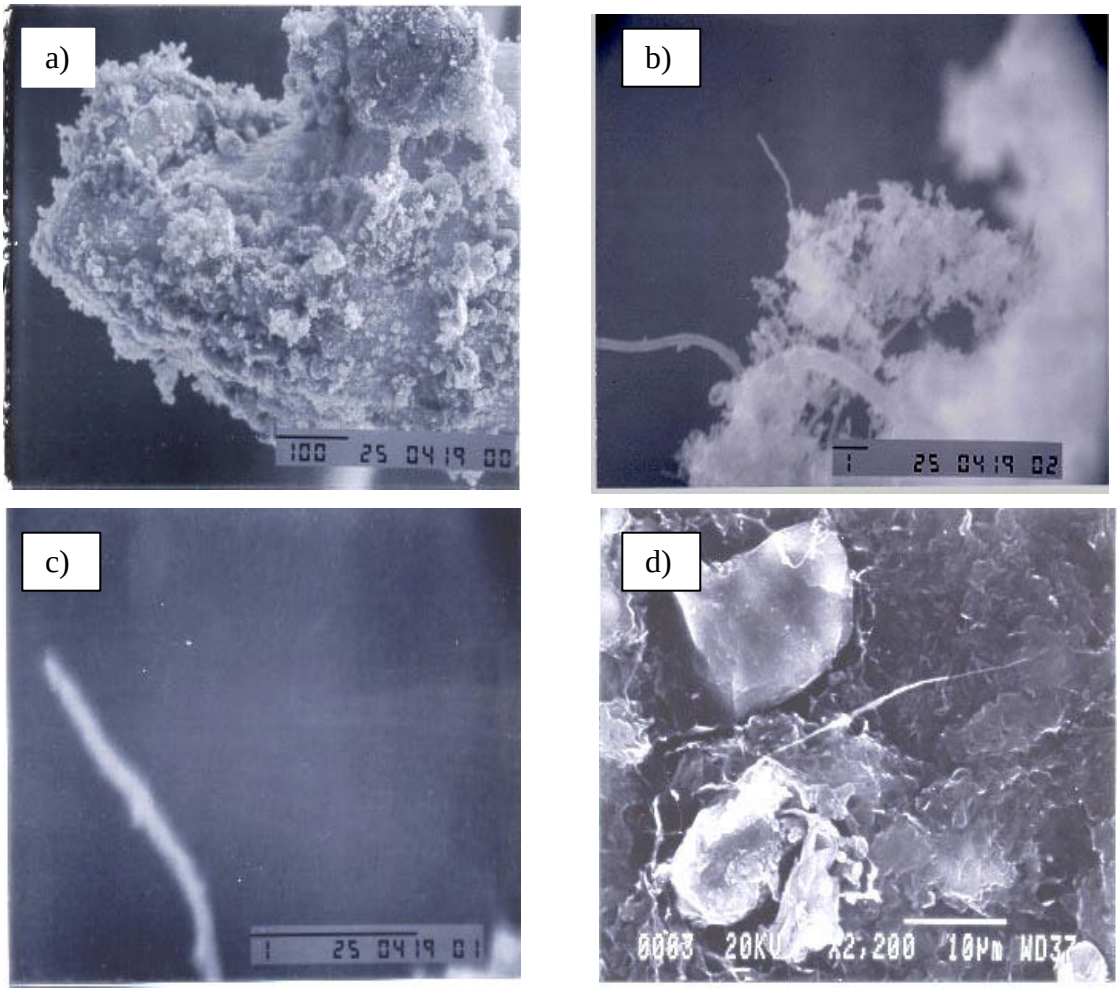

Figure 4.1 Scanning electron micrographs of MWNT and SWNT deposited on Mo tips: a) MWNT on Mo wire, b) magnified cluster of MWNT, c) single rope of MWNT and d) a SWNT rope on Mo foil. (Images a-c are taken with 25kV electrons and the bar scale corresponds to microns).

XRD was performed only on a SWNT sample that was obtained from Materials and Electrochemical Research Corporation (MREC) [1]. The sample was prepared by pressing several nanotube mats onto a Mo foil measuring $1cm^2$. The sample was placed on a XRD sample holder and held in place with a small amount of clay. The XRD pattern is shown in figure 5.2. All the diffraction peaks above 40° are attributed to the Mo foil. The predominate feature however is the broad peak ranging from ~6° to 17°. XRD data files PDF#79-1715 and PDF#74-2328 list a variety of 2-Theta reflections within this region for graphite and C_{60}. The carbon samples were known to consist of approximately 5% SWNT, carbon coated nanoparticles and amorphous carbon as they were grown in a carbon arc deposition system [2]. This broad peak was therefore attributed to various type of amorphous carbon present. The small diffraction peak located at ~ 26.5° can be assigned to the (0 0 2) reflection of the nanotube graphene sheet [3,4]. XRD thus was able to detect the presence of some nanotube structure.

In addition, XPS was also preformed on SWNT nanotube samples obtained from both MREC and Rice. XPS was done using the Mg anode on a dual anode system. The X-ray source is non-monochromatic whose primary line is the Mg K_α with energy of 1248.8eV. A survey scan was run for both samples with a pass energy of 10eV and a step size of 0.5eV. In both samples, carbon and oxygen appear to be the predominant elements. Previous reports have shown that the carbon 1s photoelectron peak is broadened by the degree of oxygen contaminants [5]. The XPS spectra of the C1s peak of both sets of nanotubes are shown in figure 5.3a and corresponding peak fits are depicted in figure 5.3b,c. The intensity of the higher energy shoulder is greater for the

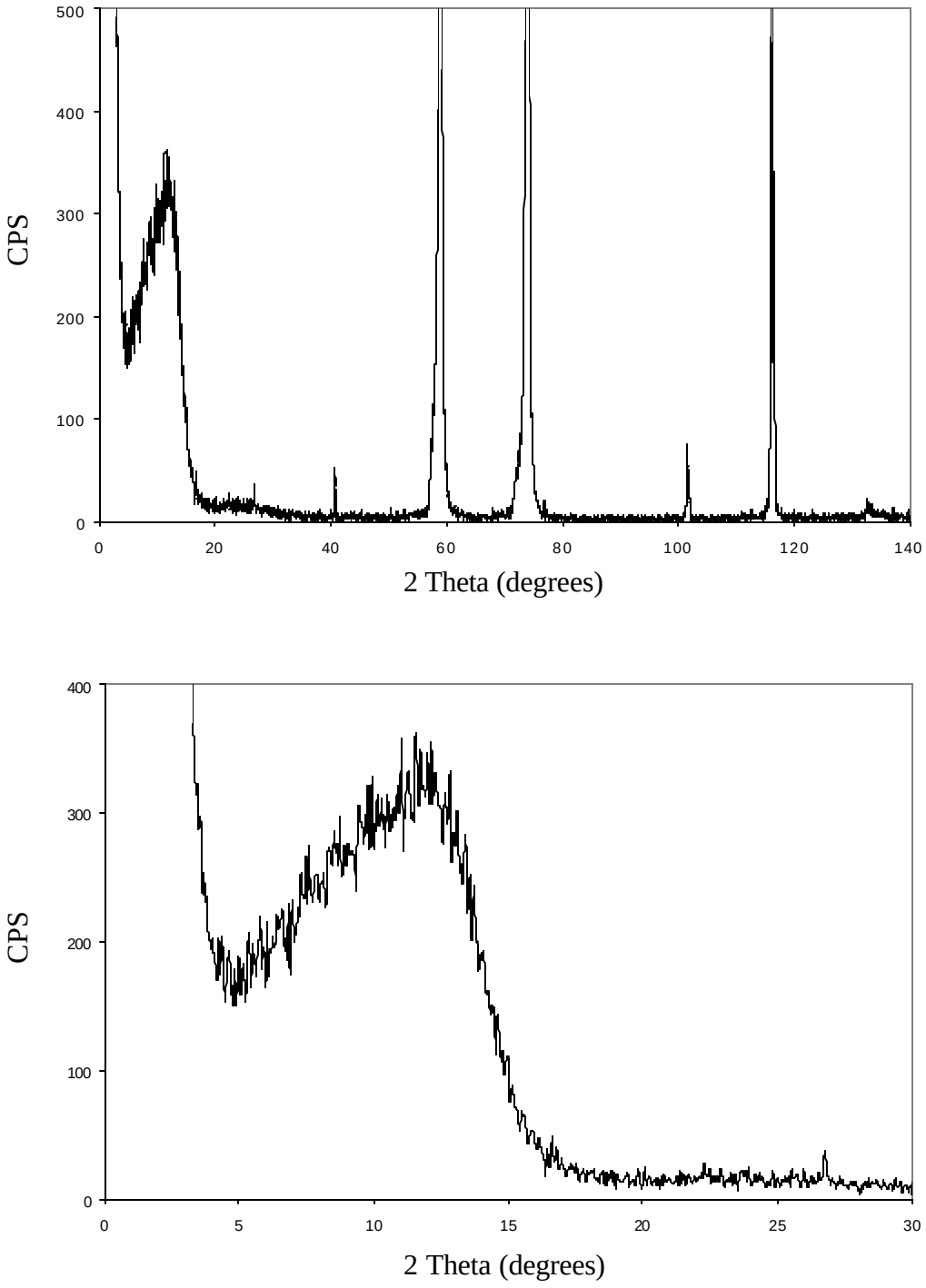

Figure 5.2 XRD pattern of single-walled nanotubes obtained from MREC.

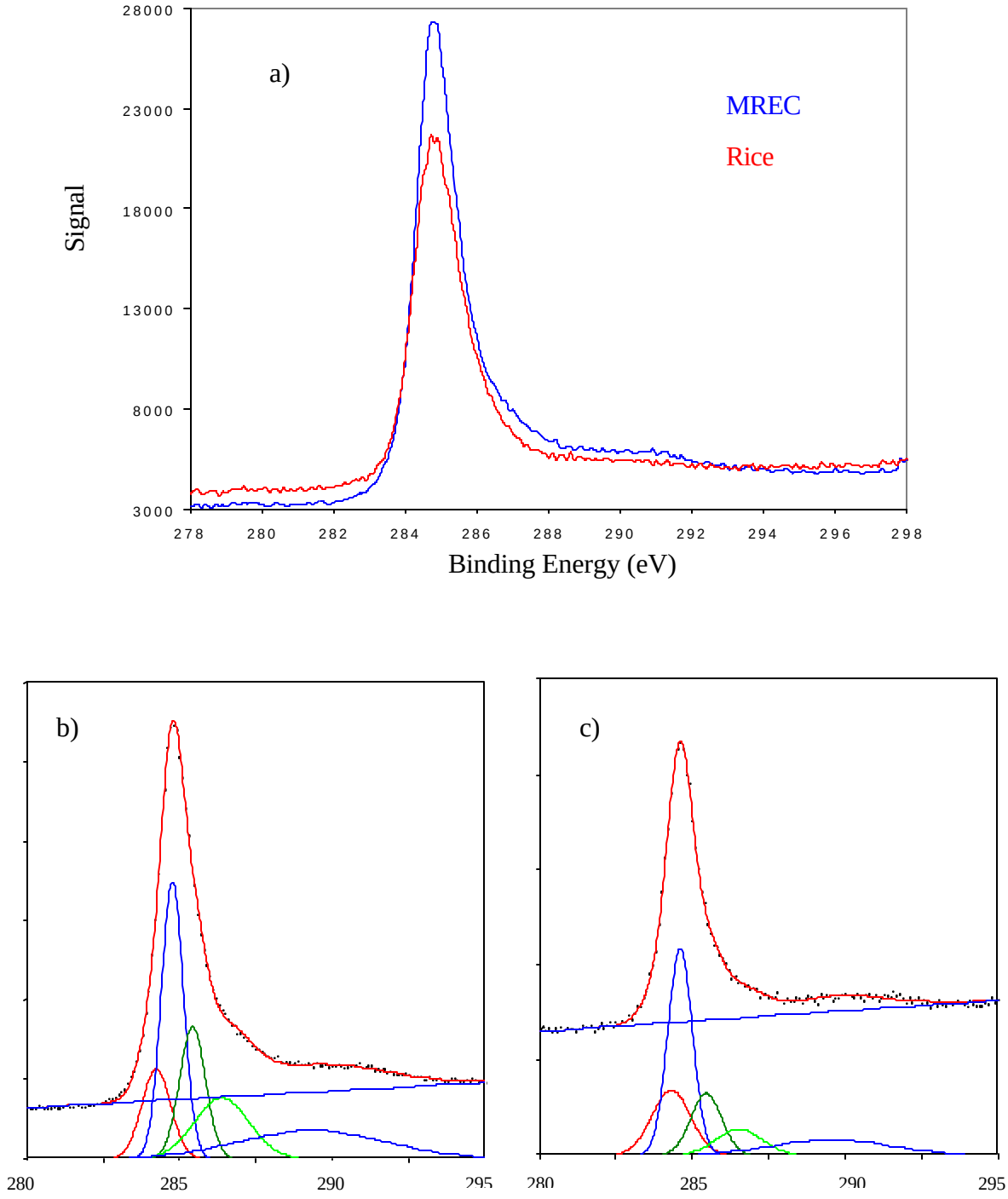

Figure 5.3 XPS spectra of C1s peaks of nanotubes from MREC and Rice, b) peakfit of MREC tubes and c) peakfit of Rice tubes.

the MREC nanotubes. Both carbon peaks can be fitted with five Gaussian curves, and in addition have all peaks in common. Peak fitted curves at 284.3, 284.8, 285.4, 286.5 and 289.4eV are common to both sets of nanotubes. The first three peaks can be attributed to graphite, polyethylene, and aromatic type carbons, which would be likely present in carbon soot [6]. The difference in the two samples arises in the higher energy shoulder, which for Rice nanotubes have a lower contribution to the overall composition than do the MREC nanotubes. These peaks with corresponding energies of 286.5 and 289.4eV can be assigned to CO and CO_2 type carbon in agreement with previous reported energies [7,8,9]. From the carbon XPS data the Rice tubes are more purified than those from MREC. To ascertain more information on the possibilities of the types of oxygen present, localized scans of the oxygen 1s peak were also performed. Figure 5.4a shows the XPS oxygen spectra of both samples and their peakfits are shown in 5.4 b,c. The oxygen peak of oxidized carbon nanotubes has been shown to extend between 531-535eV [10] as is the case here. In addition the oxygen peak of both samples can be fitted more precisely with two gaussian peaks with corresponding energies of 531.5 and 533.0eV. These two energies are in agreement with the carbon bound oxygen of C=O and O-C=O whose energies have been documented at 531.1 and 533.3eV [11] and furthermore support the carbon XPS results.

5.3 Effects of Temperature on the Emission Properties of Single-Walled Nanotubes.

The field emission characteristics of SWNTs' have been shown to have a temperature dependence at which the nanotubes are subjected [2]. In addition, the exposure of SWNTs' to air or oxygen has been shown to decrease the nanotubes'

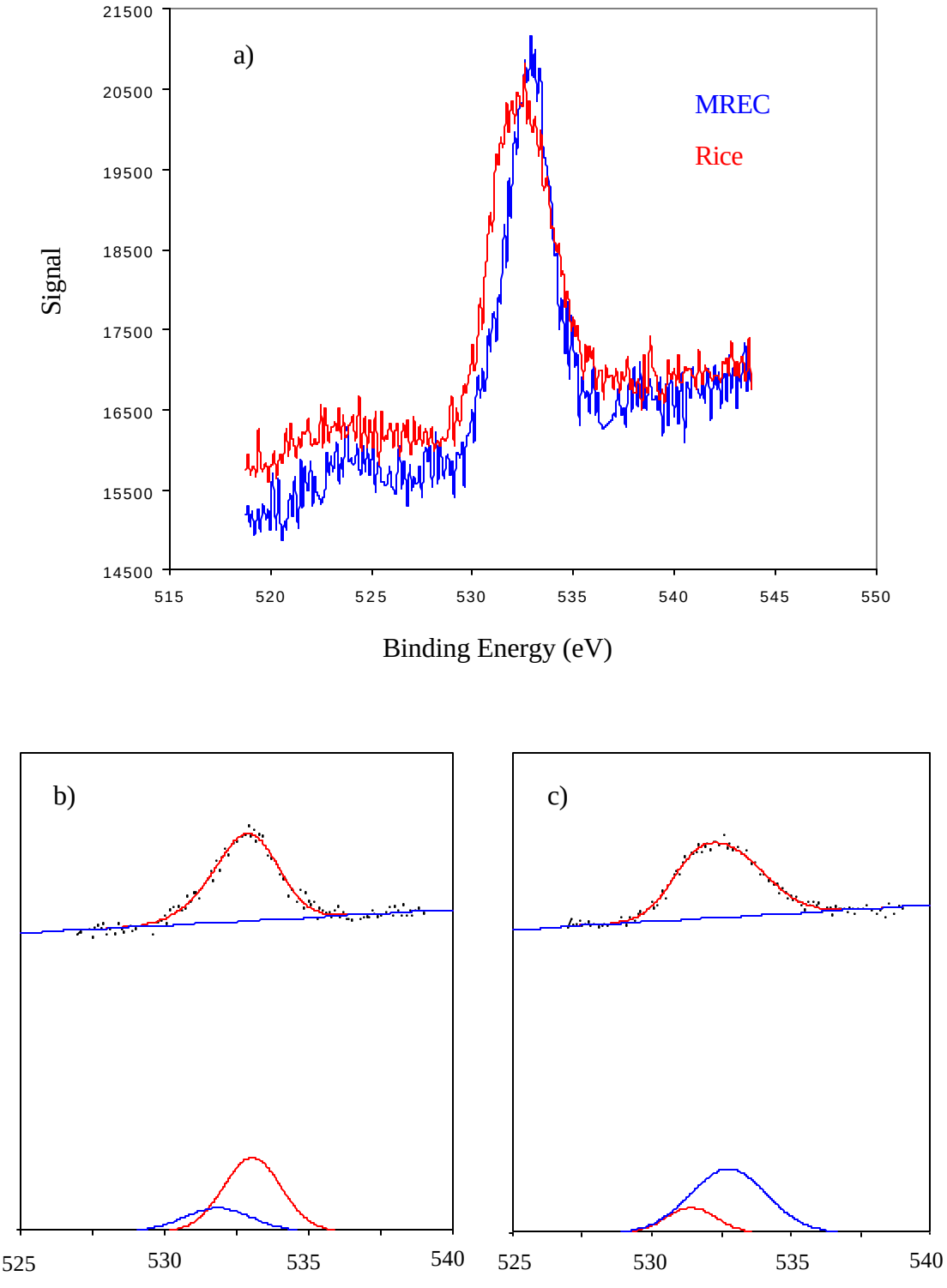

Figure 5.4 XPS spectra of O1s peaks of nanotubes from MREC and Rice, b) peakfit of MREC tubes and c) peakfit of Rice tubes.

electrical resistance [12]. However, the exposure to oxygen has been reported to increase the work function [10] and decrease the field emission current [2]. Enhancement in field emission behavior has been attributed to absorbates, but as stated by Dean *et.al*, electron energy distributions as a function of processing temperature are required. For these reasons, the work function of SWNT processed flat and tip samples were monitored as a function of processing temperature by both field and photoemission. The work function of MWNT processed tips was only monitored by field emission due to the limited supply of MWNT available. A residual gas analyzer (RGA) mass spectrometer was coupled to both systems to detect the level of particular gasses evolved during heating cycles. For flat samples, XPS was preformed monitoring the carbon and oxygen (1s) peaks. From the resulting data, the determination of the work functions of both MWNT and SWNT was achieved and the effects of processing temperature on the field emission was deduced.

Field emission from nanotube coated blunt Mo tips showed that as the tip was heated the field emission energy distribution (FEED) curve shifts to lower binding energy. Once heated above 700 ºC the FEED curve appeared to be unaffected by additional heating. The shifting in the FEED curves is most likely due to the removal of the oxides from the Mo tip, as was indicated in the previous chapter. Figure 5.5 shows FEED curves and Fowler-Nordheim (FN) plots of SWNT coated tips subjected to temperatures of ~ 150, 250, 400, and 750 ºC. Curve fitting results of the following FEED spectra are presented in table 5.1. Unfortunately, the field emission spectra does not give a direct indication as to whether the nanotube contaminants or the Mo contaminants,

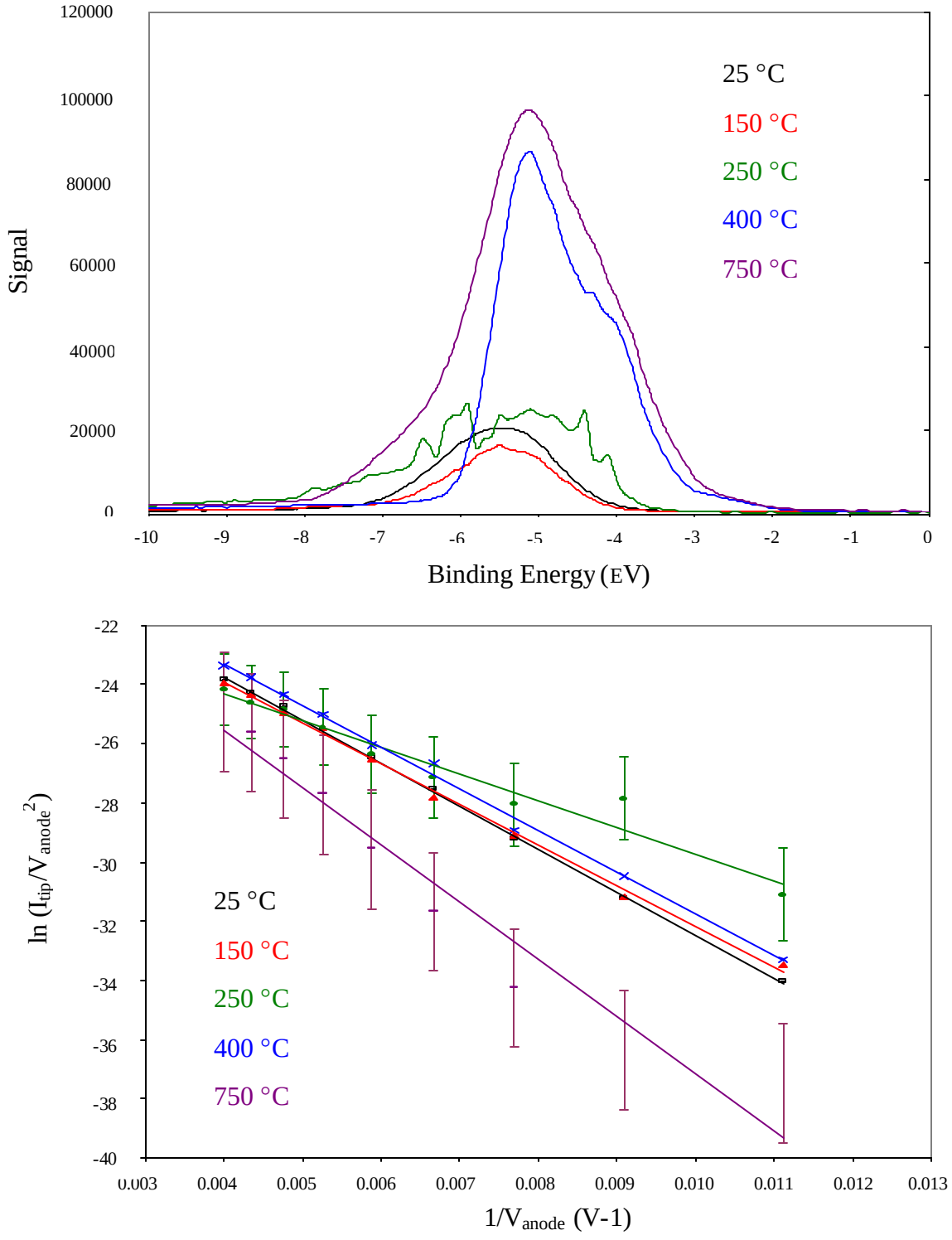

Figure 5.5 FEED and FN plots of SWNT coated Mo tips heated at various temperatures. (Error bar indicate 5% error).

or both, are responsible for the apparent shifting in the FEED spectra. Simultaneous XPS and UPS data as a function of temperature can provide a better explanation of the field emission behavior, and any effects of surface contaminants on the emission.

XPS was performed on Rice SWNT's that were placed on a Mo foil and mounted on a Mo holder. The sample was heated at the specified temperature, then allowed to cool to room temperature before XPS and UPS analysis. The carbon and oxygen 1s XPS data are shown in figure 5.6 while the UPS data are shown in figure 5.8. All data were peak fit and the results are listed in table 5.1. The XPS data show that oxygen continues to exist even at elevated temperatures. As the temperature is increased to 750 ºC the contribution of CO_2 diminishes in both the C1s and O1s peaks of the XPS spectra. In the C1s spectra, the CO contribution increases slightly while in the O1s spectra an additional structure at a binding energy of 536eV is observed. This peak may be present at other temperatures, but its intensity may be so low that it is obscured by the background noise. To show this more clearly, the peak fitted curves of the O1s structure are provided in figure 5.7. This additional peak is attributed to the oxygen atom of H_2O [11]. Furthermore the percentage of graphite and polyethylene carbon is decreased as the temperature is increased. The RGA spectra shown in figure 5.9 shows that CO_2 is the primary gas desorbed, followed by water. The UPS data indicate that the contribution from the nanotubes does not change while that from the non-nanotube carbon (-4.8eV) decreases. The FEED data are also consistent in that the nanotube contribution changes only by 9.8%. The slope of the FN plot however does increase drastically. These results can be explained by following mechanism. As the nanotubes are heated to higher

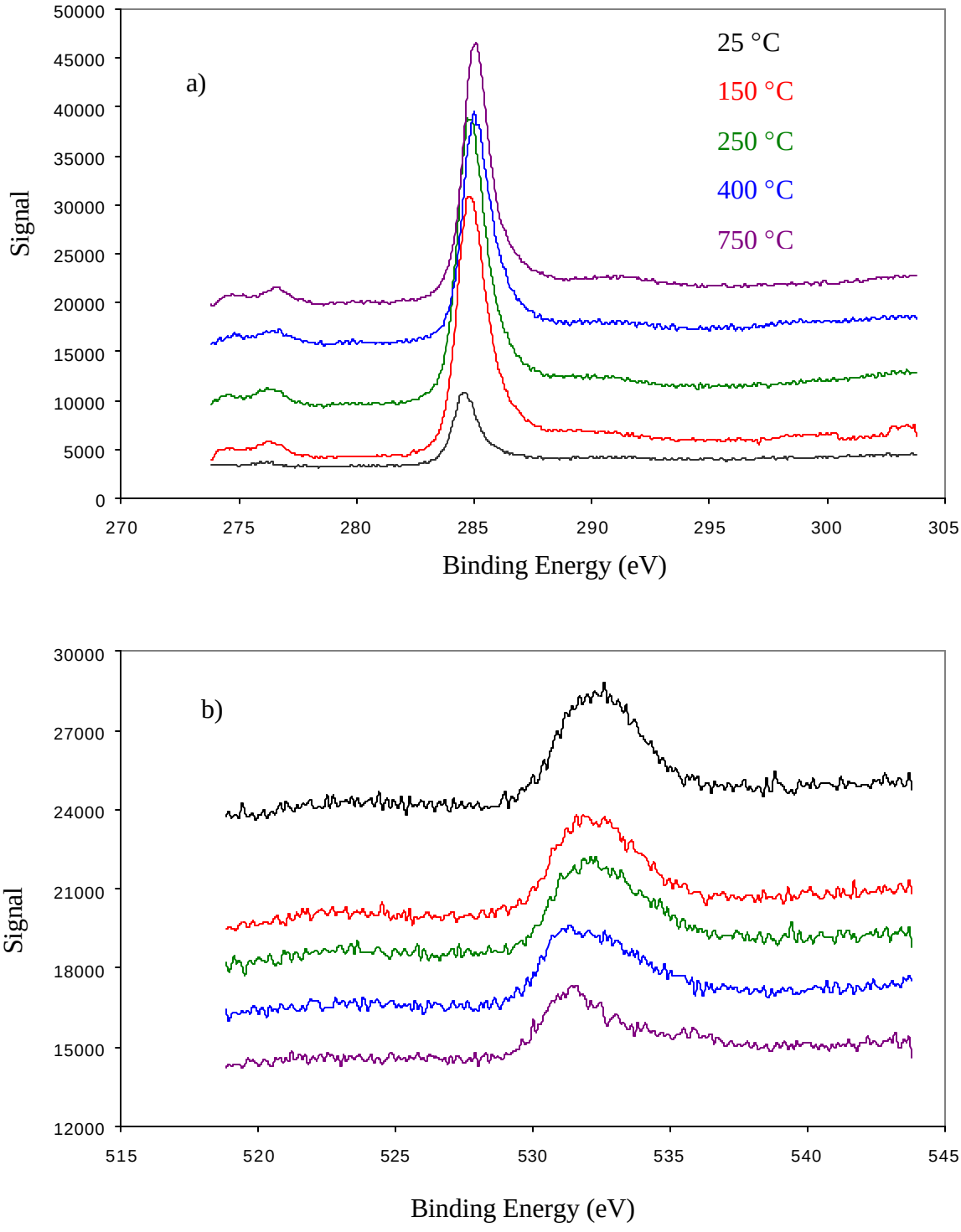

Figure 5.6 XPS of SWNT's heated at various temperatures showing the variation in the a) C 1s and b) O 1s peaks. (Color of plot in (b) correspond to the temperature above).

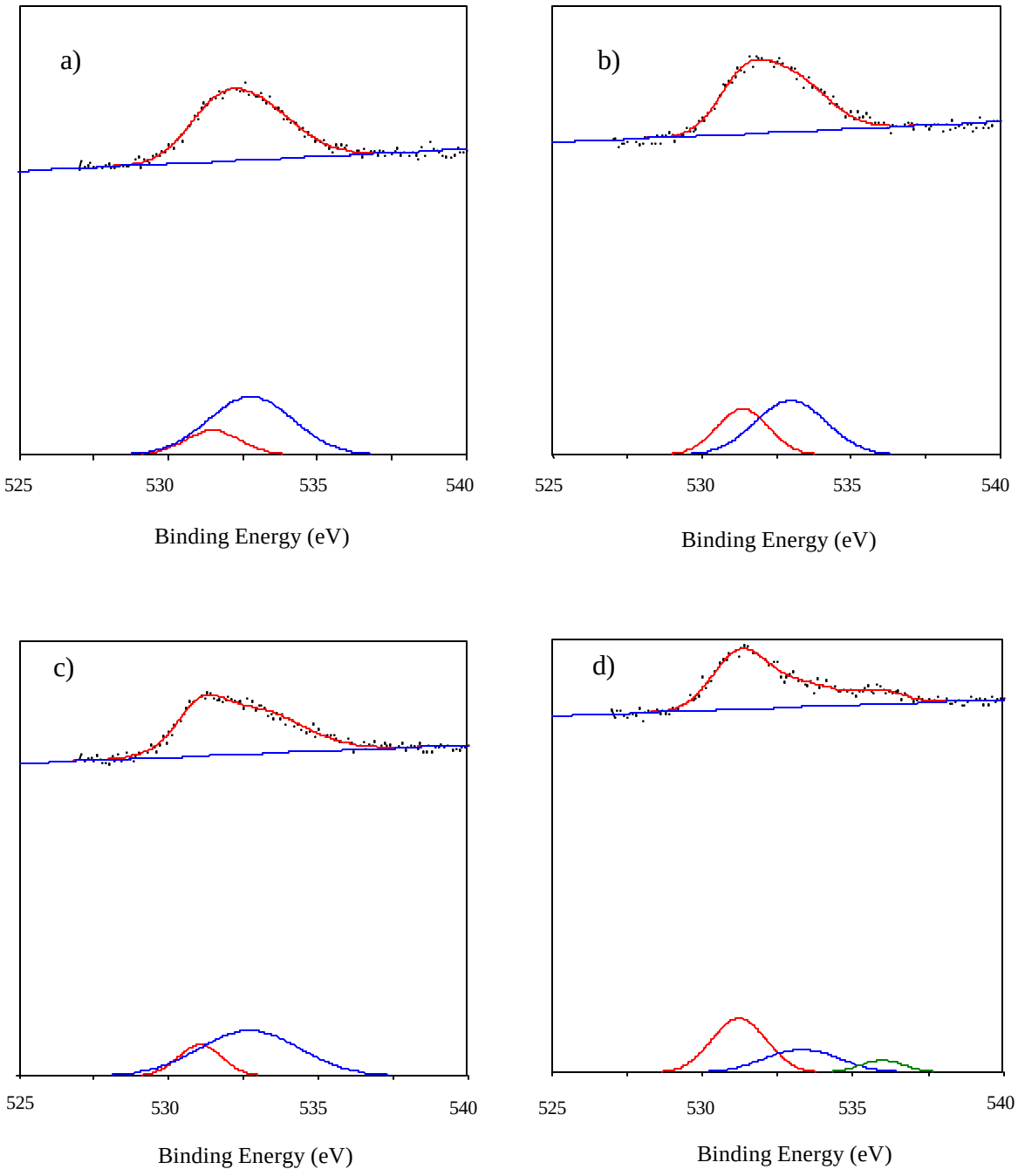

Figure 5.7 Peak Fit curves of the O1s XPS peak for temperatures of a) 25 ºC b) 150 ºC c) 400 ºC and d) 750 ºC. (Fit for 250 ºC was similar to 150 ºC and is therefore excluded)

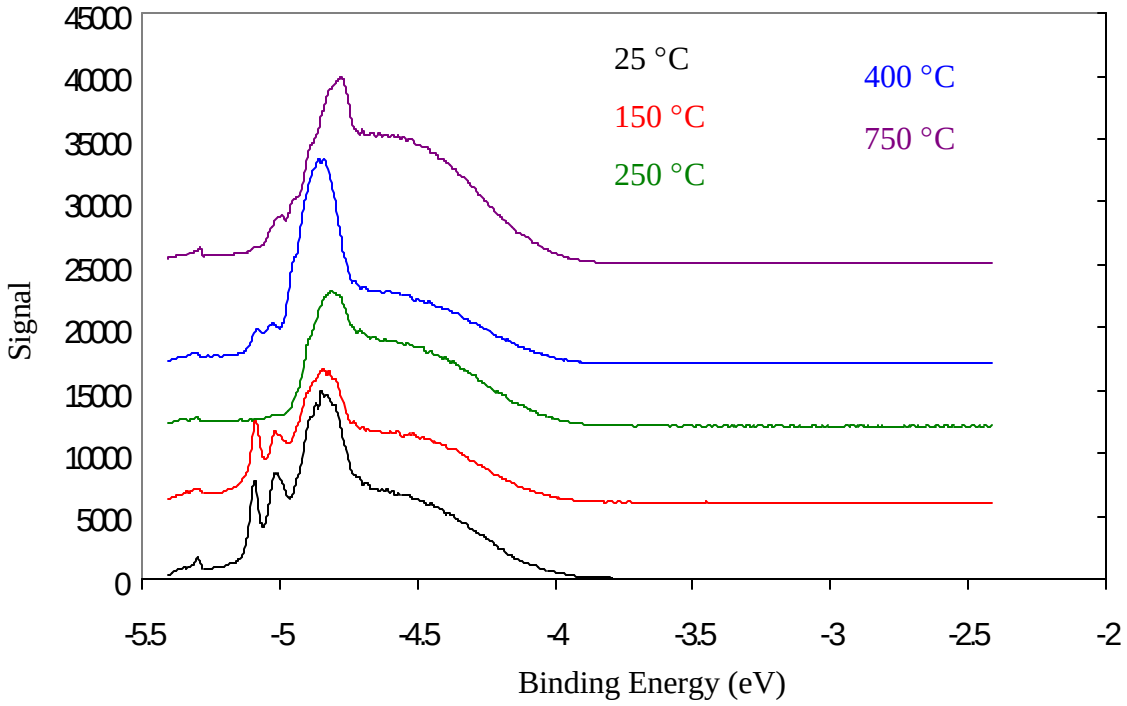

Figure 5.8 UPS of single-walled nanotubes heated at various temperatures.

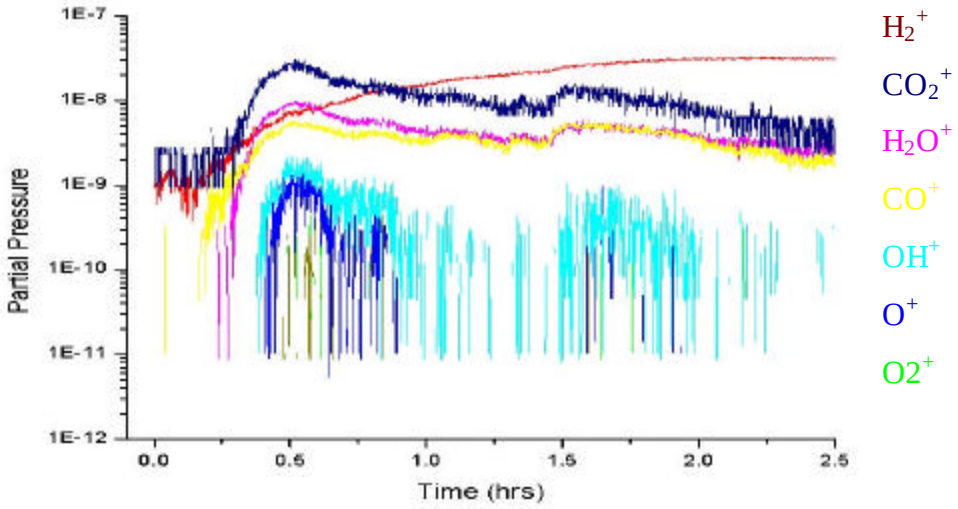

Figure 5.9 RGA of single-walled nanotubes heated to 750 ºC for 2 hours.

temperatures the nanotubes become oxidized. The oxidation occurs such that oxygen (H_2O in this case) penetrates deeper into the tubes while CO_2 escapes [13]. This results in the decrease of the CO_2 peaks and the rise of the H_2O peak in the XPS data. The H_2O present in the RGA spectrum results from the desorption of water from the chamber walls as the sample is being heated. CO and CO_2 may be what contributes to the two small peaks in the high binding energy side of the UPS spectra. In any case, the presence of the H_2O does not appear to effect the work function of the single-walled nanotubes as is evident in both the FEED and UPS data. The increase in the Fowler-Nordheim slope results from the oxidation of the nanotubes. The smaller diameter tubes are opened by the oxidation while the larger diameter tubes remain closed [13], thereby increasing the average emitter radius. An increase in the average tip radius would result in a decrease in the emission current with increasing temperature and is what is observed in this study as well as that reported by Dean [2]. Thus it appears that SWNT's do have a temperature dependence which is related to their structure and not a change in the work function.

5.4 Field Emission Characteristics of Single-walled Nanotubes Exposed to Oxygen

Nanotube coated Mo tips were operated at several emission currents while being exposed to research grade (99.999%) oxygen. Energy distribution curves and Fowler-Nordheim plots were used to determine the susceptibility of carbon nanotubes to oxygen. The main interest is to observe if their exceptional strength allows them to be operated at higher emission currents than corresponding Mo tips (that is less prone to sputtering), and to determine their emission behavior under the influence of oxygen.

Prior to exposing the nanotubes to oxygen the coated tips were heated to 700 ºC to

Peak Position of FEED Curve

Temp.	Peak 1	Peak 2
25	-5.75	-4.96
150	-5.36	-4.76
250	-5.31	-4.31
400	-5.05	-3.86
750	-4.93	-4.08

Percent Contribution

Peak 1	Peak 2
28.2	71.8
38.0	72.0
53.1	46.9
50.4	49.6
34.9	65.1

Carbon 1s Peak Position

Temp.	Peak 1	Peak 2	Peak 3	Peak4	Peak 5
25	284.3	284.6	285.4	286.5	289.5
150	284.3	284.8	285.6	286.5	288.8
250	284.4	284.8	285.6	286.7	289.3
400	284.5	284.9	285.6	286.7	289.6
750	284.4	284.9	285.6	286.7	290.3

Percent Concentration

Peak 1	Peak 2	Peak 3	Peak 4	Peak5
20.1	40.9	15.2	9.4	14.4
18.8	36.4	18.8	8.9	17.1
19.2	35.4	23.1	7.5	14.6
14.3	34.9	27.9	9.2	13.7
13.5	34.5	26.0	15.8	10.3

Oxygen 1s Peak Position

Temp.	Peak 1	Peak 2	Peak 3
25	531.5	532.8	
150	531.5	532.8	
250	531.6	532.3	
400	531.0	532.7	
750	531.2	533.3	536.0

Percent Concentration

Peak 1	Peak 2	Peak 3
21.6	78.4	
21.6	78.4	
39.6	60.4	
23.1	76.9	
56.2	33.3	10.5

UPS Peak Position

Temp.	Peak 1	Peak 2	Peak 3	Peak4	Peak 5.
25	-5.09	-5.01	-4.85	-4.66	-4.34
150	-5.09	-5.02	-4.86	-4.60	-4.33
250	-	-	-4.83	-4.63	-4.32
400	-	-5.06	-4.86	-4.62	-4.33
750	-	-4.97	-4.81	-4.60	-4.29

Percent Contribution

Peak 1	Peak 2	Peak 3	Peak4	Peak 5
3.9	5.8	26.1	42.7	17.2
4.2	3.4	29.3	38.4	17.0
		25.2	50.3	24.5
	5.3	44.0	29.5	19.8
	5.6	18.7	57.6	17.3

Table 5.1 FEED, UPS and XPS data of single-walled nanotubes subjected to various temperatures.

remove any oxide on the Mo tip on which the tubes were placed. This was done to eliminate any shifting in the FEED curve due to the oxide formation. Tips were moved into position over the extraction anode, and the distribution signal was maximized in a similar manner as was performed for the Mo tips in the previous chapter. Once an energy distribution curve of a clean tip was obtained, oxygen was introduced. All data were acquired with a pass energy of 5eV, a step size of 0.1eV, and swept 10 times over an energy range of 10eV. All current-voltage curves were obtained over the same voltage sweep, and all FEED curves were obtained with the same extraction voltage on the anode. Oxygen exposure experiments were first performed on MREC nanotubes at emission currents of 2pA, 1nA and 5nA. With RICE nanotubes only 1 and 5nA emission currents were used. The previous section indicated that the work function of both types of nanotubes are the same the only difference being the amount of other forms of carbon present; therefore, similar results are to be expected. From the FEED and FN plots the effects of field emission in the presence of oxygen were deduced.

Field emission spectra and Fowler-Nordheim plots for the two extremes in current are presented in figures 5.10 and 5.11. The numerical values of all field emission data are listed in table 5.2 for MREC nanotubes and in table 5.3 for Rice nanotubes. For O_2 exposure at 2pA, the slope in the FN plot increased by 7% over the 1000L exposure, while the average work function remained relatively unchanged. The percent contribution of the nanotube peak did however show a 24.8% difference from its maximum to its minimum values. For the 1nA exposure both sets of samples showed a consistent variation in the slope and work function. That is, whenever the slope

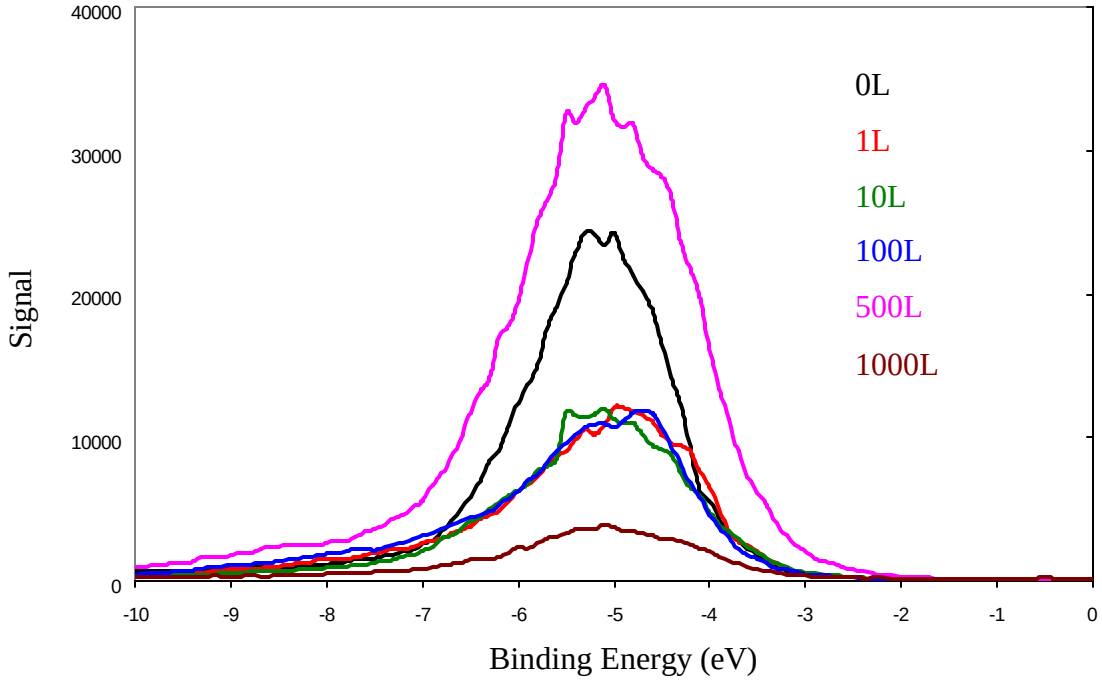

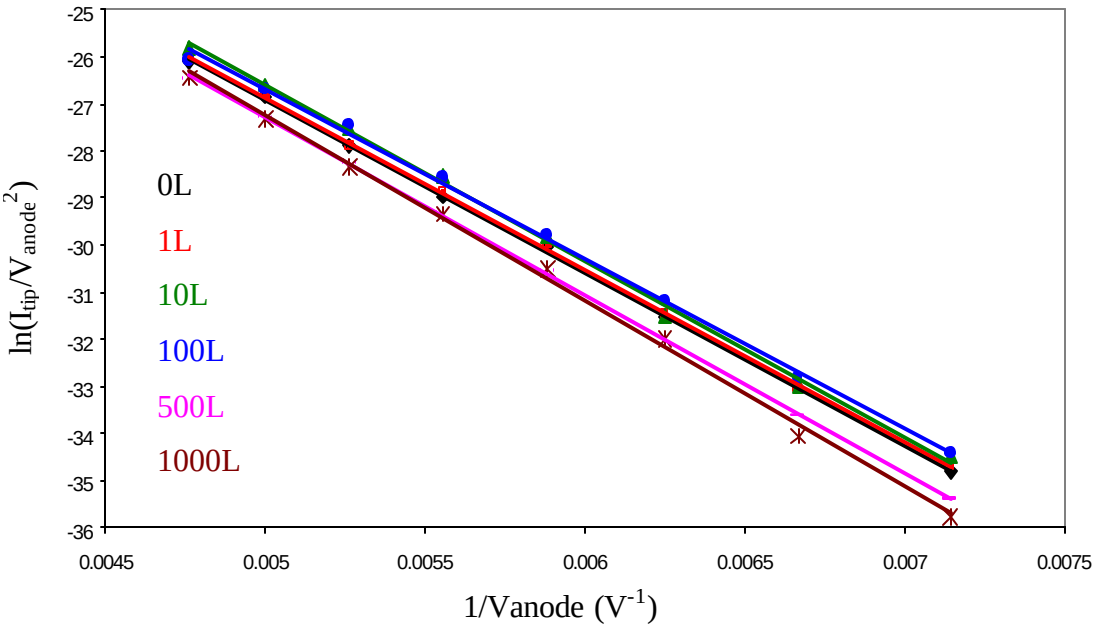

Figure 5.10 FEED and FN plot of MREC SWNT's exposed to O_2 with a tip emission of 2pA.

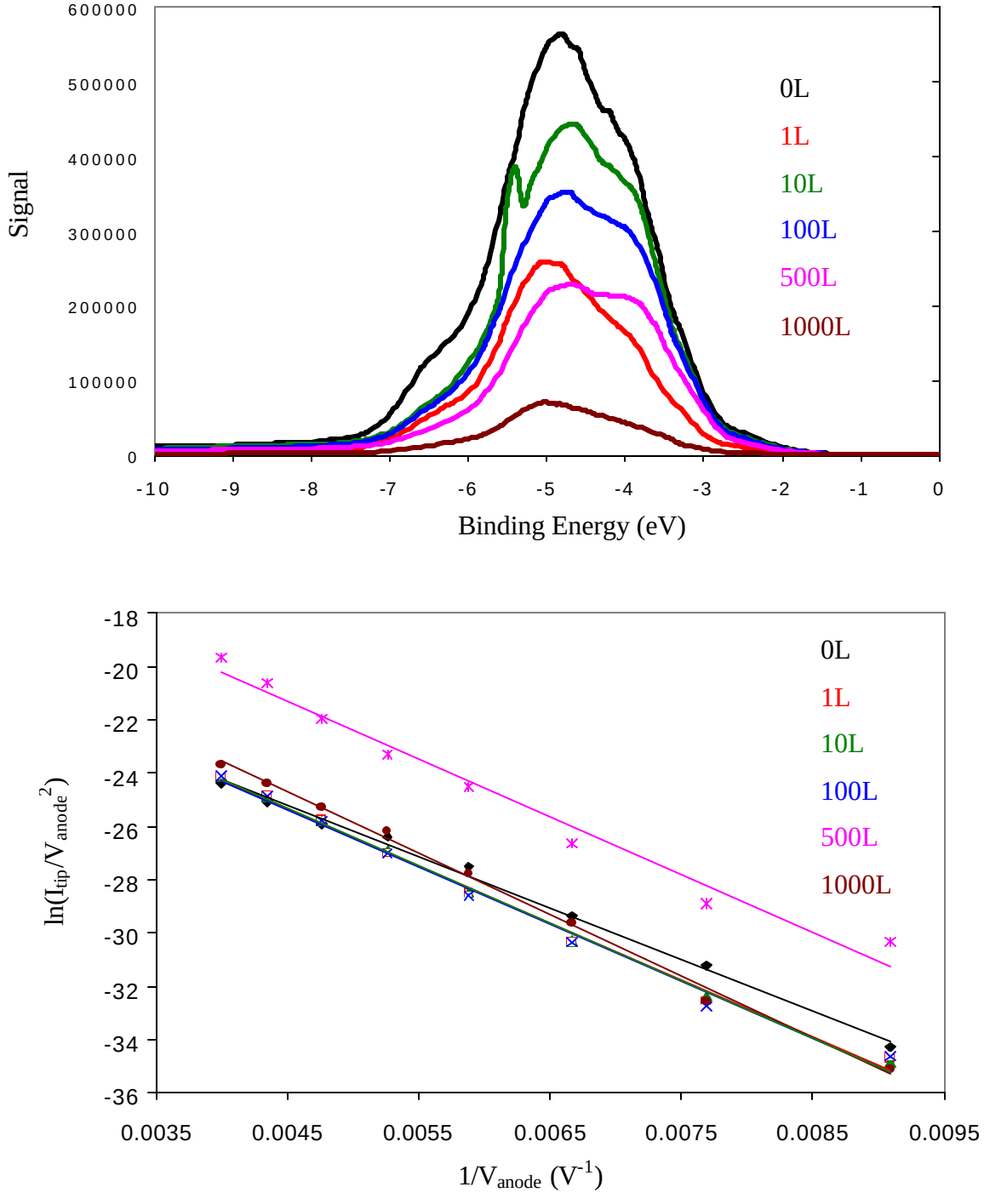

Figure 5.11 FEED and FN plot of Rice SWNT's exposed to O_2 with a tip emission current of 5nA.

Current (nA)	Exposure (L)	FN slope	Intercept	Work Function (eV)	Percent Area	Average Work Function	% diff. in work function	% diff. in FN slope
0.002	0	-3672.4	-8.5492	-4.96	42.5	-4.52	-	-
				-4.21	57.2			
	1	-3654.0	-8.6060	-4.96	38.7	-4.52	0.00	-0.50
				-4.25	61.3			
	10	-3743.8	-7.8899	-4.97	34.8	-4.49	0.66	+2.43
				-4.24	65.2			
	100	-3600.0	-8.6857	-4.87	31.7	-4.35	3.17	-3.92
				-4.11	68.3			
	500	-3775.7	-8.4076	-4.96	43.6	-4.46	2.50	+4.76
				-4.07	56.4			
	1000	-3944.1	-7.5359	-4.96	46.8	-4.49	0.67	+4.36
				-4.07	53.2			
1	0	-3317.6	-10.367	-5.05	39.5	-4.44	-	-
				-4.04	60.5			
	1	-3716.5	-8.5663	-4.92	45.1	-4.50	1.34	+11.3
				-4.16	54.9			
	10	-3707.0	-8.7174	-4.95	43.4	-4.50	0.00	-0.26
				-4.16	56.6			
	100	-3816.7	-8.4782	-5.13	47.7	-4.60	2.20	+2.92
				-4.12	52.3			
	500	-3798.6	-8.5267	-5.06	42.0	-4.68	1.72	+0.48
				-4.40	48.0			
5	0	-1552.5	-17.156	-5.00	38.9	-4.61	-	-
				-4.56	42.7			
				-4.07	18.4			
	1	-1512.0	-17.664	-5.61	30.2	-4.91	6.30	-0.69
				-4.85	48.4			
				-4.32	21.4			
	10	-1481.1	-17.526	-5.69	41.4	-5.00	1.82	-2.04
				-4.69	39.0			
				-4.17	19.6			
	100	-1505.0	-17.069	-5.78	35.5	-4.99	0.20	+1.67
				-4.76	41.0			
				-4.20	23.5			
	500	-1266.1	-18.244	-5.48	39.6	-4.89	2.02	-17.24
				-4.66	41.8			
				-4.14	18.6			
	1000	-1070.1	-19.420	-5.87	40.2	-5.21	6.34	-16.78
				-4.97	37.7			
				-4.43	22.1			

Table 5.2 Field emission data of MREC SWNT's exposed to O_2 while operated at various tip emission currents.

Current (nA)	Exposure (L)	FN slope	Intercept	Work Function (eV)	Percent Area	Average Work Function	% diff. in work function	% diff. in FN slope
1	0	-2427.6	-14.581	-6.33	4.00	-4.53	-	-
				-4.87	47.2			
				-4.06	48.8			
	1	-2327.5	-14.640	-6.72	3.00	-4.42	2.46	-4.21
				-4.86	44.5			
				-4.30	52.5			
	10	-2395.8	-14.164	-6.68	4.8	-4.74	6.99	+2.89
				-5.13	44.8			
				-4.21	50.4			
	100	-2105.1	-15.581	-6.49	4.1	-4.50	5.19	-12.92
				-4.85	41.3			
				-4.09	54.6			
	500	-2230.7	-15.077	-6.20	6.9	-4.42	1.79	+5.79
				-4.84	42.8			
				-3.82	50.3			
	1000	-2241.2	-15.150	-6.32	5.9	-4.62	4.42	+0.47
				-4.98	40.5			
				-4.16	53.6			
5	0	-1926.0	-16.533	-5.97	4.6	-4.27	-	-
				-4.81	23.8			
				-3.98	71.6			
	1	-2143.9	-15.693	-5.95	7.1	-4.41	3.22	+10.71
				-4.83	25.9			
				-4.08	67.0			
	10	-2152.2	-15.642	-5.55	6.3	-4.32	2.06	+0.39
				-4.70	31.3			
				-4.01	62.4			
	100	-2151.3	-15.682	-5.95	4.7	-4.05	6.45	-0.04
				-4.78	29.8			
				-3.58	65.5			
	500	-2168.7	-11.552	-5.60	7.1	-4.54	11.4	+0.80
				-4.77	30.8			
				-4.31	62.1			
	1000	-2311.3	-14.301	-6.07	5.3	-4.41	2.90	+6.37
				-4.88	34.8			
				-4.00	59.8			

Table 5.3 Field emission data of Rice SWNT's exposed to O_2 while operated at various tip emission currents.

decreased the work function also decreased. In this case, as in the 2pA case, the average work function varies by ~6%, but the percent contribution of the nanotubes differs by as much as 23% for the MREC tubes and 11.2% for those from Rice. The largest variations in the slope and work function occur for the 5nA emission current. At this current the average work function for both samples show a difference of ~11.7% and the slope changes overall by 18% for the Rice tubes and 37% for the MREC tubes. The percent difference in the nanotube contribution is 24.3% (MREC) and 18% (Rice). These results indicate that the nanotubes are being sputtered at all currents, with the largest degree of sputtering occurring at the greater current. Structural changes in SWNTs due to sputtering [14] can lead to a decrease in the tube height, opening of the nanotube cap, disruption of electronic states in the cap [15] or complete etching of the nanotubes [16]. Unlike the Mo tips, the nanotubes are not oxidized in the presence of O_2 and therefore the nanotubes are continuously being ablated. The apparent increase in work function is due to the removal of the nanotubes resulting in a larger contribution of field emission from the higher binding energy carbon. The variation in the slope shows a decrease in the MREC tubes and an increase in the Rice tubes. This may be the result of the degree of purity in the samples, where the Rice tubes have a larger concentration of nanotubes compared to the MREC tubes. In the case of the Rice tubes sputtering occurs at the same rate, but because there is a larger concentration of nanotubes, the tubes away from the apex contribute more resulting in an apparent increase in the tip shape. Thus it appears that carbon nanotubes may be susceptible to long term sputter degradation [14].

5.5 Field Emission from Multi-Walled Carbon Nanotubes.

Multi-walled carbon nanotubes have been reported to have a higher work function than single-walled nanotubes. The value of their work function however, varies dramatically from 1.3eV to as high as 12eV [10, 17-21]. MWNTs are also known to be more resistant to radiation damage [14] and thus maybe more resistant to sputter damage. In this section, field emission was performed on MWNTs from which the work function was obtained and compared to the SWNT work function.

The MWNTs were purchased from NANOCs Corporation. The MWNT coated Mo tips were spot welded onto a tungsten filament, through which resistive heating could be accomplished. The tip was heated to 1000 °C and the FEED curves obtained (after tips cooled to room temperature) were used to determine the work function of the MWNTs. A larger anode voltage was required to obtain the same current as SWNTs. This is attributed to the larger diameter of the MWNT as compared to SWNT. The FEED curves obtained at different temperatures are shown in figure 5.12. With the exception of the tip heated to 1000 °C, all curves could be fitted with two exponentially modified gaussians (EMG's). The FEED and FN data are listed in table 5.3. It is clearly seen that up to these temperatures the effective work function is significantly larger than that of SWNTs. The two peaks of the FEED curves at lower temperatures are assigned to nanotube carbon and graphitic carbon. The separation of the two peaks is on the order of the separation of the peaks in SWNT samples. At 800 °C any oxides on the Mo tip will be removed thereby not contributing to any peak shifting (due to any resistance at the Mo-nanotube interface) as was seen for Mo tips. The effective work function of 7.38eV

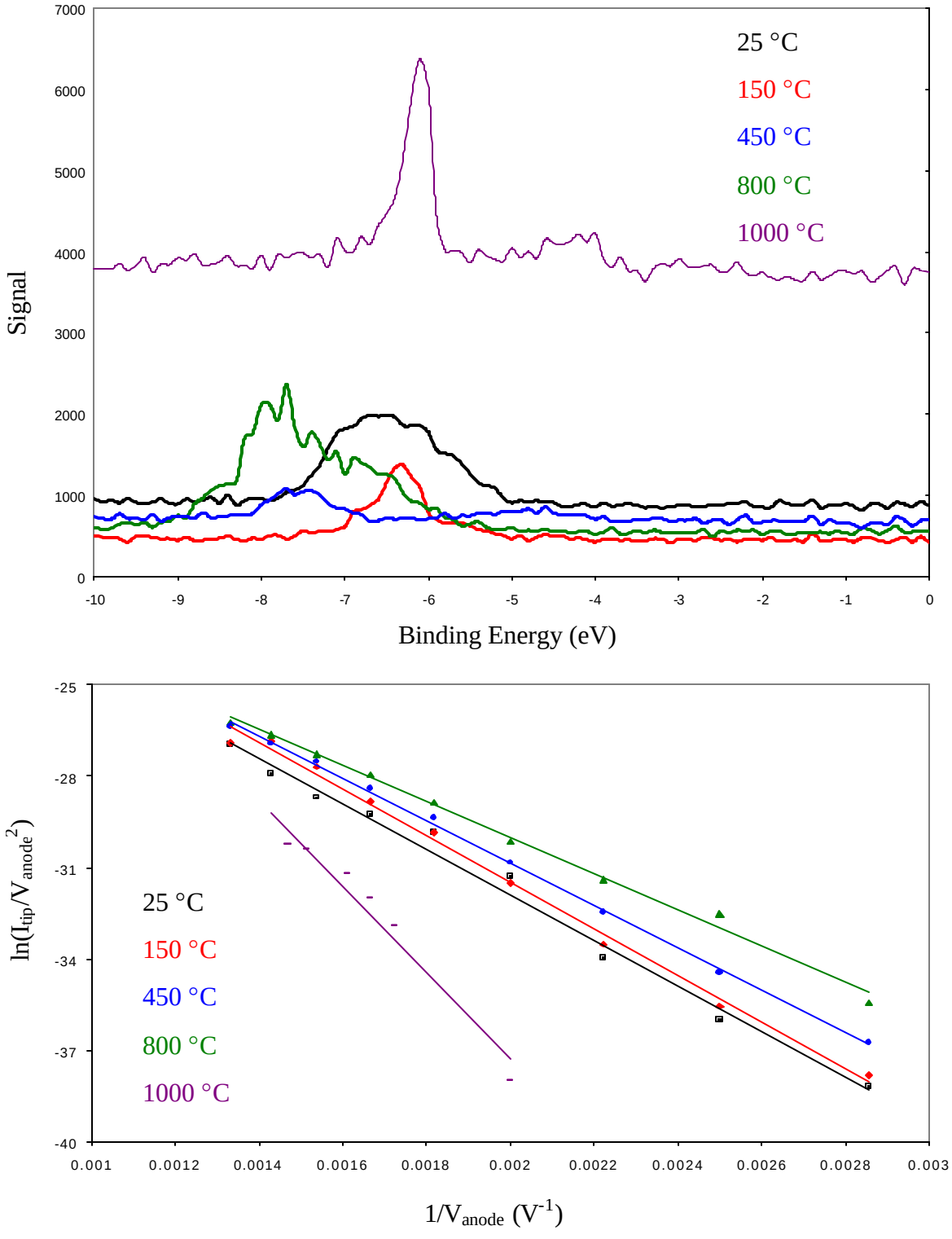

Figure 5.12 FEED and FN plots of MWNT heated at various temperatures.

Temp. (°C)	FN slope	Intercept	FEED peak1	Position peak 2	Percent peak 1	Comp. peak2
25	-7487.6	-16.905	-6.00	-6.83	55.8	44.2
150	-7640.8	-16.208	-5.52	-6.14	21.0	79.0
450	-5928.3	-18.176	-6.65	-7.61	44.0	56.0
800	-6962.2	-16.911	-7.38	-7.68	60.0	40.0
1000	-14082.0	9.1089	-5.97		100.0	

Table 5.4 FEED and FN data of MWNTs heated at various temperatures. Larger emission currents were required to obtained FEED spectra, with currents ranging from 20-50nA.

for MWNT agrees with that reported by Fransen [20]. Above this temperature, i.e 1000 °C, the FEED reduces to one peak with a work function of 5.97 eV. With increasing temperature the percent contribution from the lower FEED peak increases. This may suggest that the emission above annealing at 1000 °C is strictly from nanotube carbon. The shifting to lower binding energy is likely the result of enhanced conductivity with increasing temperature due to the removal of impurities or other defects [22]. It is believed that the work function of MWNTs is the same as SWNTs but the greater resistance shifts the energy distribution (as in the case of heavily oxided Mo) in such a way as to make the work function appear to be higher.

5.6 Conclusions

In conclusion, MWNTs have a higher turn on voltage than SWNTs and may be due to their larger tube diameters. The work function of MWNTs is likely to be the same (reported at 4.3 eV [10]) as that of SWNTs but appears larger due to higher defect concentrations which is probably the reason for the wide range of reported work function values. To confirm this, UPS measurements would have to be performed. However, due to the quantity available this was not done in this study. Thus MWNTs are not as desirable a field emitter candidate as are SWNTs.

The XPS and UPS results from SWNT flat samples showed that at elevated temperatures, these nanotubes can be oxidized. The likely mechanism is the opening of the nanotube cap, followed by the uptake of water. This results in the destruction of the cap but does not effect the work function.

Oxygen exposure experiments showed that the single-walled nanotubes are not oxidized when operated in the presence of oxygen. They are however, sputtered to some extent at all emission currents ranging from 2pA to 5nA. The largest extent of sputtering occurs at the 5nA current, resulting in a as much as a 24% difference in the work function after 1000L O_2 exposure. Unlike the Mo tips in the previous chapter, an energy distribution could still be obtained after this exposure time. This would suggest that the SWNTs are tougher, resulting in a slower ablation rate. To determine whether these nanotubes are a viable field emitter candidate, long term oxygen exposures would need to be performed.

References:

1. Materials and Electrochemical Research Corporation, Tuscon, AZ.
2. K.E. Dean, P. von Allmen, B.R. Chalamala, J. Vac. Sci. Technol. B **17**, 1959 (1999).
3. L. Ci, B. Wei, C. Xu, J. Liang, D. Wu, S. Xie, W. Zhou, Y. Li, Z. Liu, D. Tang, J. Cryst. Growth, **233**, 823 (2001).
4. A. Cao, C. Xu, J. Liang, D. Wu, B. Wei, Chem. Phys. Lett. **344**, 13 (2001).
5. W.H. Lee, S.J. Kim, W.J. Lee, R.C. Haddon, P.J. Reucroft, Appl. Surf. Sci. **181**, 121 (2001).
6. Handbook of X-ray Photoelectron Spectroscopy, Perkin-Elmer Corporation. Physical Electronics Division, Eden Prairie, MN 55344.
7. N. Kovtyukhova, E. Buzaneva, A. Senkevich, Carbon **36**, 549 (1997).
8. W.H. Lee, P.J. Reucroft, Carbon **37**, 7 (1999).
9. W.H. Lee, J.Y. Kim, Y.K Ko, P.J. Reucroft J.W. Zondlo, Appl. Surf. Sci. **141**, 107 (1999).
10. H. Ago, Th. Kugler, F. Cacialli, K. Petritsch, R.H. Friend, W.R. Salaneck, Y. Ono, T. Yamabe, K. Tanaka, Synthetic Metals, **103**, 2494 (1999).
11. U. Zielke, K.J. Hüttinger, W.P. Hoffman, Carbon, **34**, 983 (1996).
12. P.G. Collins, K. Bradley, M. Ishigami, A. Zettl, Science, **287**, 1801 (2000).
13. N. Yao, V. Lordi and S.X.C. Ma, E. Dujardin, A. Krishnan, M.M.J. Treacy, T.W.

Ebbesen, J. Mater. Res., **13**, 2432 (1998).

14. O.R. Monteiro, V.P. Mammana, M.C.Salvadori, J.W Ager III, S. Dimitrijevic, Appl. Phys. A, **71**, 121 (2000).
15. J.M. Bonard, J.P. Salvetat, T. Stockli, W.A. de Heer, L. Forro, A. Chatelain. Appl. Phys. A, **69**, 245 (1999).
16. K.A. Dean, B.R. Chalamala, Appl. Phys. Lett., **75**, 3017 (1999).
17. Yu.V. Gulyaev, N.I. Sinitsyn, G.V. Torgashov, Sh.T. Mevlyut, A.I. Zhbanov, Yu.F. Zakharchenko, Z.Ya. Kosakovskaya, L.A. Chernozatonskii, O.E. Glukhova, I.G. Torgashov, J. Vac. Sci. Technol. B, **15**, 422 (1997).
18. O. Gröning, O.M. Khttel. Ch. Emmenegger, P. Gröning, L. Schlapbach, J. Vac. Sci. Technol. B, **18**, 665 (2000).
19. O.M. Küttel, O. Groening, C. Emmenegger, L. Schlapbach, Appl. Phys. Lett., **73**, 2113 (1998).
20. M.J. Fransen, Th.L van Rooy, P. Kruit, Appl. Surf. Sci., **146**, 312 (1999).
21. P.G. Collins, A. Zettl, Phys. Rev. B, **55**, 9391 (1997).
22. T.W Ebbesen, H.J. Lezec, H. Hiura, J.W. Bennet, H.F. Ghaemi, T. Thio, Nature, **382**, 54 (1996).

CHAPTER 6

EMISSION CHARACTERISTICS OF ALUMINUM

6.1 Introduction

Very few studies have focused on aluminum as a possible field emission candidate, most likely due to high reactivity towards oxygen. Most field emission studies have focus on nitrides of aluminum. Aluminum metal has a lower work function than does molybdenum metal or carbon [1]. Another interesting feature of aluminum is that its oxide layer creates a diffusion barrier, which prevents any further oxidation. Furthermore, the oxidation of the aluminum surface has been reported to lower the work of clean aluminum [2,3,4]. The above facts suggest that aluminum maybe a excellent candidate for a field emitting material. In this chapter both field and photoemission studies on aluminum samples will be presented.

6.2 Sample Preparation and Characterization

The aluminum used in these studies was 0.02in. diameter wire of 99.9998% purity purchased from Alfa Aesar. Flat samples for XPS and UPS measurements were prepared by coiling the aluminum wire in a circular manner on top of the XPS sample peg. For XRD analysis a flat sample was prepared by wrapping the Al wire around a $1cm^2$ Mo foil. Aluminum tips for field emission studies were prepared by cutting wire strips of approximately 2 inches in length. The wire strips were then spot welded onto a tungsten filament after which they were chemically etched. The etching solution consisted of an aqueous solution of 5% HF and 25% HNO_3. Complete etching of a single

tip occurred over a time period of 7-8 hours. Once etched, the tip was submerged in concentrated HF to remove the oxide or hydroxide layer formed in solution. The tips were then viewed in a scanning electron microscope to determine the quality of the etch process. Figure 6.1 shows the image of an etched aluminum wire. This indicates that Al tips can be prepared using a HNO_3 and HF solution.

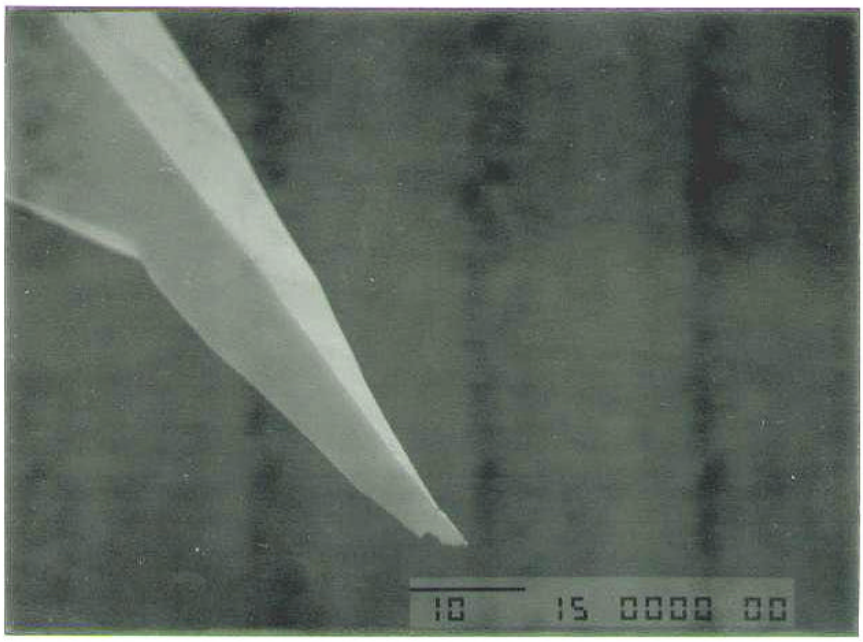

Figure 6.1 Scanning electron microscope image of an aluminum tip chemically etched in a solution of 5% HF and 25% HNO_3. (Image taken with 15kV electrons and magnification bar corresponds to microns)

X-ray diffraction (XRD) was done on flat samples to determine which crystal planes were predominately present. Figure 6.2 is the diffraction pattern of a flat sample irradiated with the Cu $K_{\alpha 1}$ line. All peaks are reference to PDF file # 04-0787. The dominant peak at the 2 value of 44.9° is associated with the (2 0 0) crystal plane of aluminum. The peaks at 38.6° and 65.2°are from the (1 1 1) and (2 2 0) planes of Al while the doublets at 78.4°, 82.6° and 99.2° are from the (3 1 1), (2 2 2) and (4 0 0) crystal planes of Al. The peaks at 58.5° and 73.5° are associated with the (2 0 0) and (2 1 1) crystal planes of Mo. Unfortunately XRD is not sensitive enough to observe the presence of the thin oxide that would be present on the Al surface. Therefore, X-ray photoelectron spectroscopy (XPS) was done on the same Al samples.

Since XPS is a more surface sensitive technique than XRD, it was used on both flat and etched Al samples in order to detect the presence of any oxide present. The flat sample consisted of a coil of Al wire. For the tip samples, XPS was preformed on a tip that was etched in solution and rinsed with HF after the etch process. For the XPS measurements, the Mg K_{α} X-ray was used along with a pass energy of 10eV. The XPS spectrum of a flat sample is shown in figure 6.3. The data for the Al 2p peak can be fitted with three Gaussian curves with centers at 73.6, 75.8 and 76.7eV. These peaks can be attributed to metallic aluminum and two of its oxides, Al_2O_3 and AlO_x, even though they are slightly shifted from their documented values. For clean evaporated aluminum, the reported binding energy of the 2p peak is 72.6eV [5]. On the hand the binding energy of the 2p peak for the oxide of aluminum varies depending on its structure and

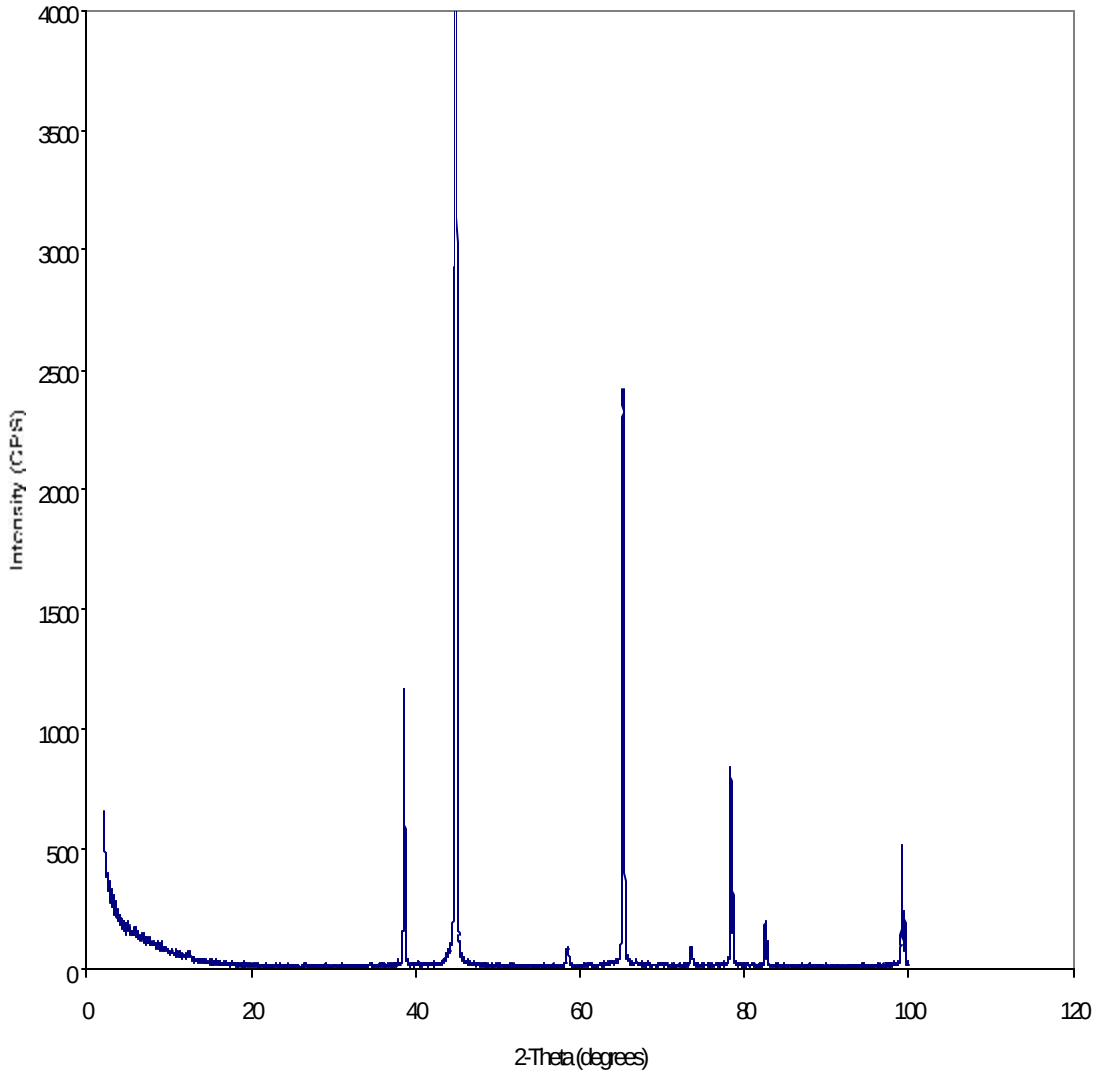

Figure 6.2 XRD pattern of Aluminum wire sample coiled around a Mo foil.

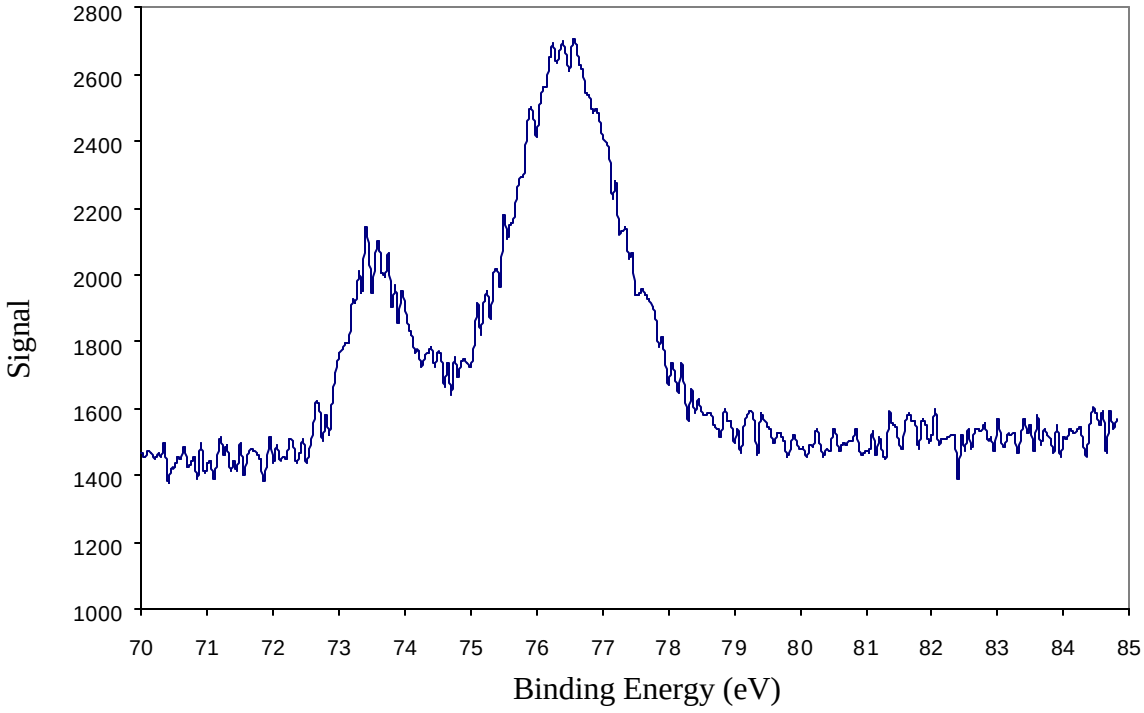

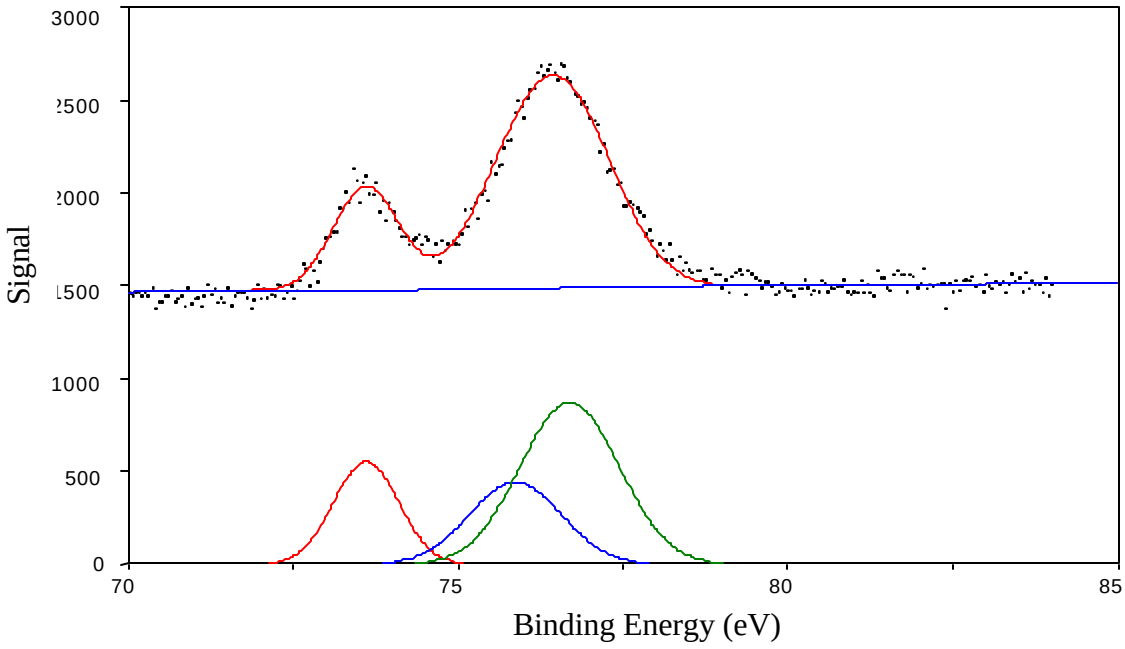

Figure 6.3 XPS spectrum of Al 2p peak with corresponding peak fit. The peaks are assigned to Al, Al_2O_3 and AlO_x.

stoichiometry [5,6,7]. The reported values of the binding energies for the shifting from the elemental Al position are 1.25-3.0eV [5,6,7]. Classification of the AlO_x has been limited to an intermediate oxidation state. In this case the peaks are all shifted by ~1eV. This is due to the nonconductive nature of the oxide film resulting in the charge build up at the surface. The Al peak results from the metal underlying the oxide film. Since this native oxide film is at most 30 Å thick, the X-rays are able to penetrate through the film and excite Al atoms, whose electrons must have escape depths greater than 30Å. The assignment of the peak at 73.6eV to the Al^0 state is justified by the shift in the position when the sample is sputtered with Ar^+ ions. The spectrum of the sputtered sample overlapped with the previous result, showing the shift to lower binding energy (see in figure 6.3). The peak centers all shift by 0.6eV and are located at 73.0, 75.2 and 76.1eV. In addition the lower energy peak becomes larger and the oxide peaks become smaller, indicating the reduction in the oxide film thickness, but not complete removal. XPS of an Al tip also showed the existence of an oxide, as would be expected. However, the spectrum had a low signal to noise ratio such that the two peaks blend together, making it difficult to obtain an accurate peak fit. The XPS data for the Al tip subjected to the etching solution is shown in figure 6.4. It is evident that there is a low signal to noise ratio. This is attributed to the small area from which electrons are excited. In any case the effect of the presence of this oxide on the work function of Al would be of interest to field emission device technology.

Both UPS and FEED were used to examine the work function of Al flat samples and tips. UPS was performed on flat samples for both sputtered and non-sputtered

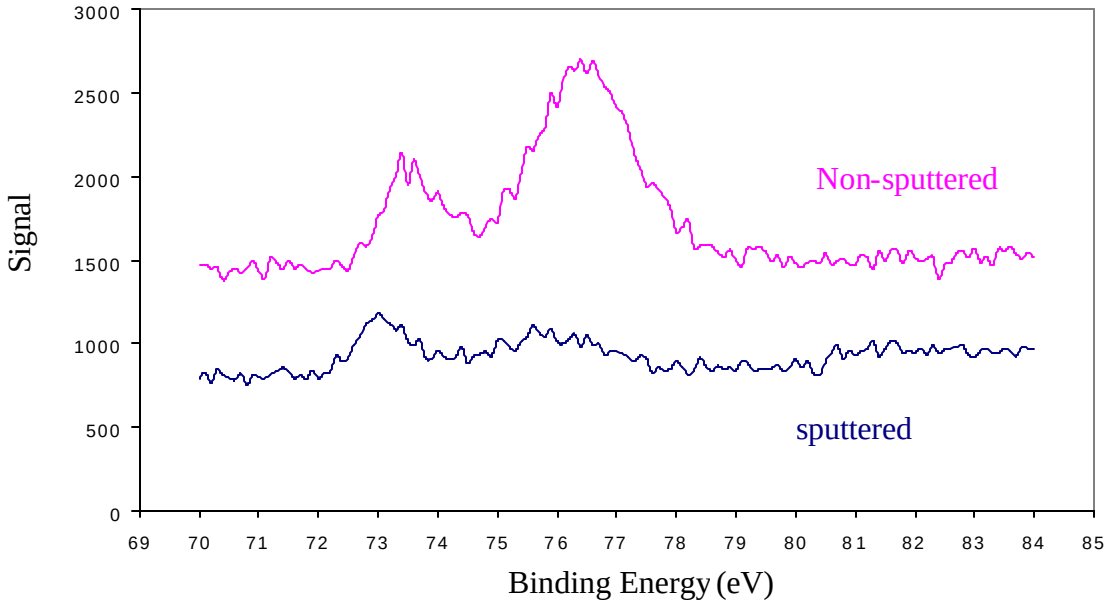

Figure 6.4 XPS of an aluminum sample that was sputtered for 30 minutes. The spectra shows the shift of 0.6 eV and a reduction in the oxide intensity.

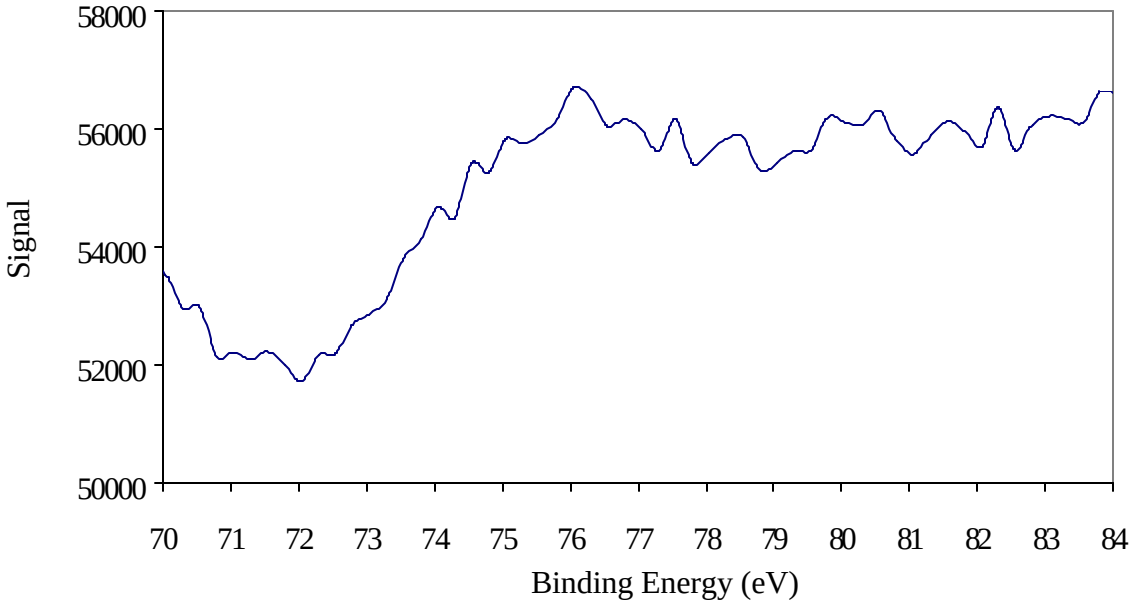

Figure 6.5 XPS of an aluminum wire tip after etching in solution of HNO_3 and HF.

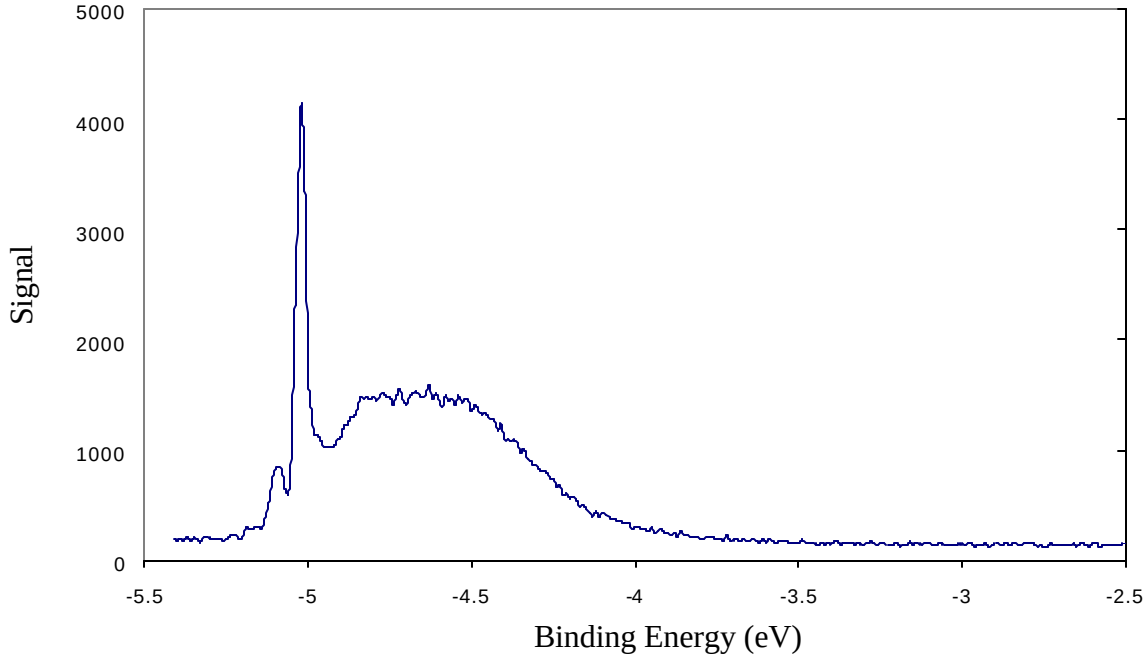

Figure 6.6 Low energy UPS on an Al sample prior to sputter cleaning.

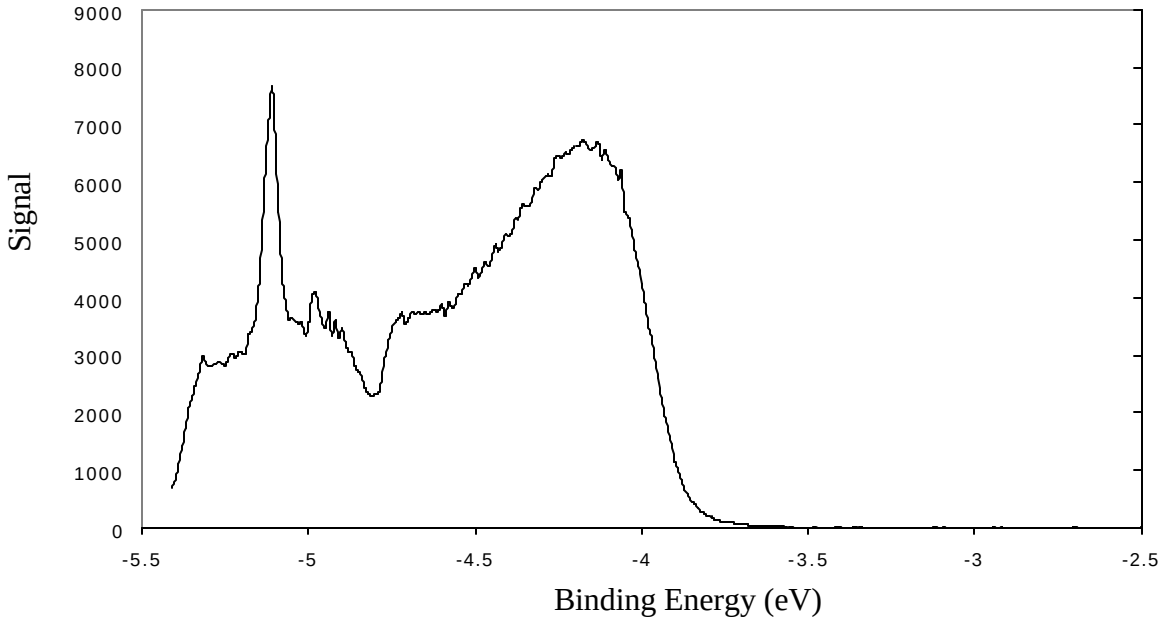

Figure 6.7 Low energy UPS on the same Al sample after 30 minutes of sputtering. The spectra shows a larger intensity at the low energy regime and an additional peak at ~4.0eV.

samples while FEED was only conducted on etched samples. Both samples were heated and the results will be compared in the next section. The UPS spectrum for Al flat sample is shown in figure 6.5. The spectra can be fitted with five Gaussian curves with energies of –4.33, -4.57, -4.83, -5.02 and –5.09eV. The data of both sets of UPS data are presented in table 6.1. The first two peaks are assigned to Al and Fe [1], where the Fe arises from the sample peg. The other three peaks are difficult to assign, since there are no reportedly agreed upon work function values for the oxides of aluminum. Most studies indicate that upon oxidation the work function of Al is decreased initially by as much as 1.4eV [3]. These studies however, examine the work function change for 1-3 monolayer coverage. The change in the work function is also reported to depend on the pressure at which the Al is exposed [8,9]. At higher pressures, the work function of Al actually increases [10]. With this in mind, and the XPS data presented, it is believed that the peak at -4.83eV is due to Al_2O_3 and the peaks at –5.02 and -5.09eV result from sub-stoichiometric AlO_x. When the sample is sputtered with Ar^+ for a period of 30 minutes (etch rate of 0.825nm/min), the intensity of the Al work function peak increases by ~ two. An additional peak required to fit the curve with a corresponding energy of –4.08 eV. This could result from two possibilities. The first is that it is the work function of the (1 1 0) crystal plane of Al whose work function is 4.06eV [1]. The second possibility is that the reduction of the oxide thickness contributes to the lowering of the work function as described in the previously stated studies. Another interesting feature in the UPS data is the structure of the higher energy regime. The peak associated with Al_2O_3 decreases by approximately a factor of two. The two other peaks, which have been associated in

this work with the sub-oxides, are shifted but their contributions remain relatively unchanged. It is believed that these peaks could be oxides of Al in the form of hydrates or hydroxides, which readily form on the surface. Field emission from a tip sample also gives similar values. The FEED curve from a tip sample is shown in figure 6.7 and the corresponding peak fit data is listed in table 6.1. FEED from a single tip also shows the

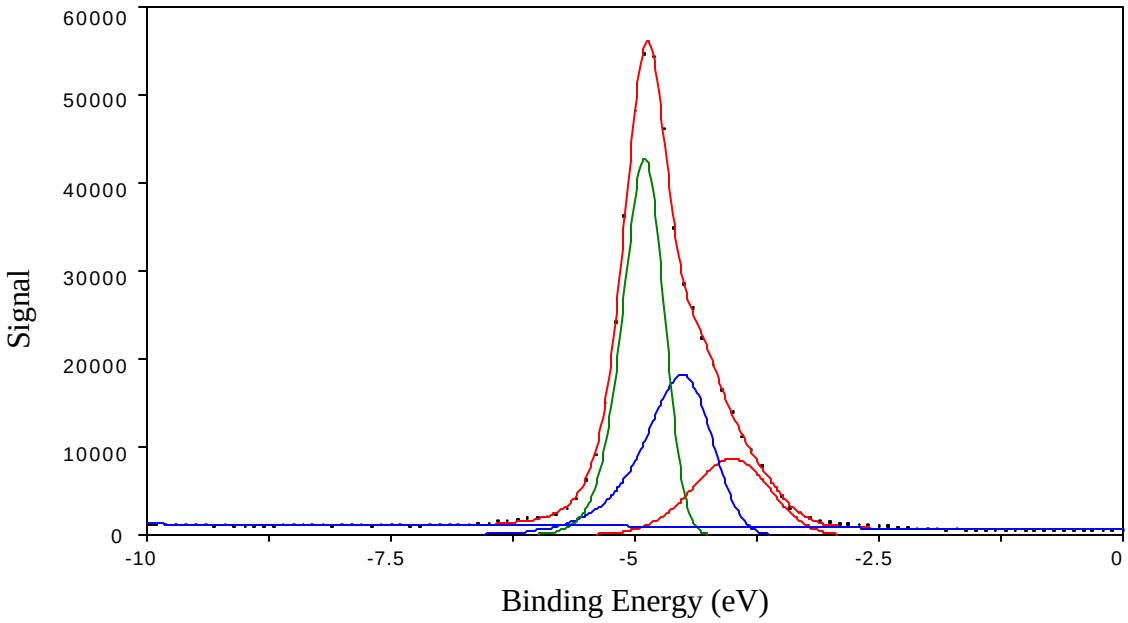

Figure 6.8 Field emission energy distribution curve of an etched Al tip showing the presence of a lower work function oxide with a value of 3.8 eV.

XPS data of sputtered and non-sputtered Aluminum

Sample	Peak Position			Percent Composition		
	Peak 1	Peak 2	Peak 3	Peak 1	Peak2	Peak3
non-sputtered	73.6	75.8	76.7	22.1	25.0	52.9
sputtered	73.0	75.2	76.1	47.9	25.0	27.1

UPS data of sputtered and non-sputtered Aluminum

Sample	Peak Position						Percent Composition					
	Peak						**Peak**					
	1	2	3	4	5	6	1	2	3	4	5	6
non-sputtered	-	-4.3	-4.6	-4.8	-5.0	-5.1	-	19.7	28.9	35.4	12.8	3.2
sputtered	-4.0	-4.3	-4.7	-5.0	-5.1	-5.2	16.6	37.4	15.8	13.0	4.2	13.0

FEED data of an etched Aluminum tip

Peak Position (eV)			Percent Contribution		
peak 1	peak 2	peak 3	peak 1	peak 2	peak 3
-4.78	-4.29	-3.81	47.6	34.3	18.1

Table 6.1 XPS and UPS data of Al sample before and after sputtering. FEED data of an etched Al tip showing a comparison in work function values obtained from field emission.

occurrence of a lower work function contributor. The FEED and UPS results indicate that the existence a of a very thin oxide layer can reduce the work function of aluminum as previously observed.

6.3 Variation in the Work Function of Aluminum Heated to 125 °C as Measure by FEED and UPS

In the previous section, UPS results indicated that the valence band spectrum affected by the oxidation of aluminum. Sputtering of aluminum appears to clean the surface thereby reducing the photoelectric threshold. Since thermal heating is another method by which metal surfaces can be cleaned, the heating of Al was investigated. In this section the effect of heating aluminum on the FEED and UPS energy distributions will be presented.

The electron energy distributions from an etched Al tip were monitored as the Al tip was heated. One fact to be noted is that a much larger anode voltage was required to obtain field emission as compared to Mo or carbon nanotube samples. The initial tip was heated to a temperature of 200 °C, resulting in the degradation of the tip, as interpreted by the lower emission current at the same anode voltage, as well as, the disappearance of the FEED signal. It was believed that the low melting temperature of Al and the orientation (tip directed in the downward position) causes the tip to become blunted . For this reason a lower temperature was used with a new tip. FEED curves for an Al tip heated to 125°C over various time intervals is shown in figure 6.8. As the tip is heated for longer times, the distribution curve shifts to lower energy. Even more interesting is that the distribution becomes separated into two distinct curves. All curves were peak fit and the

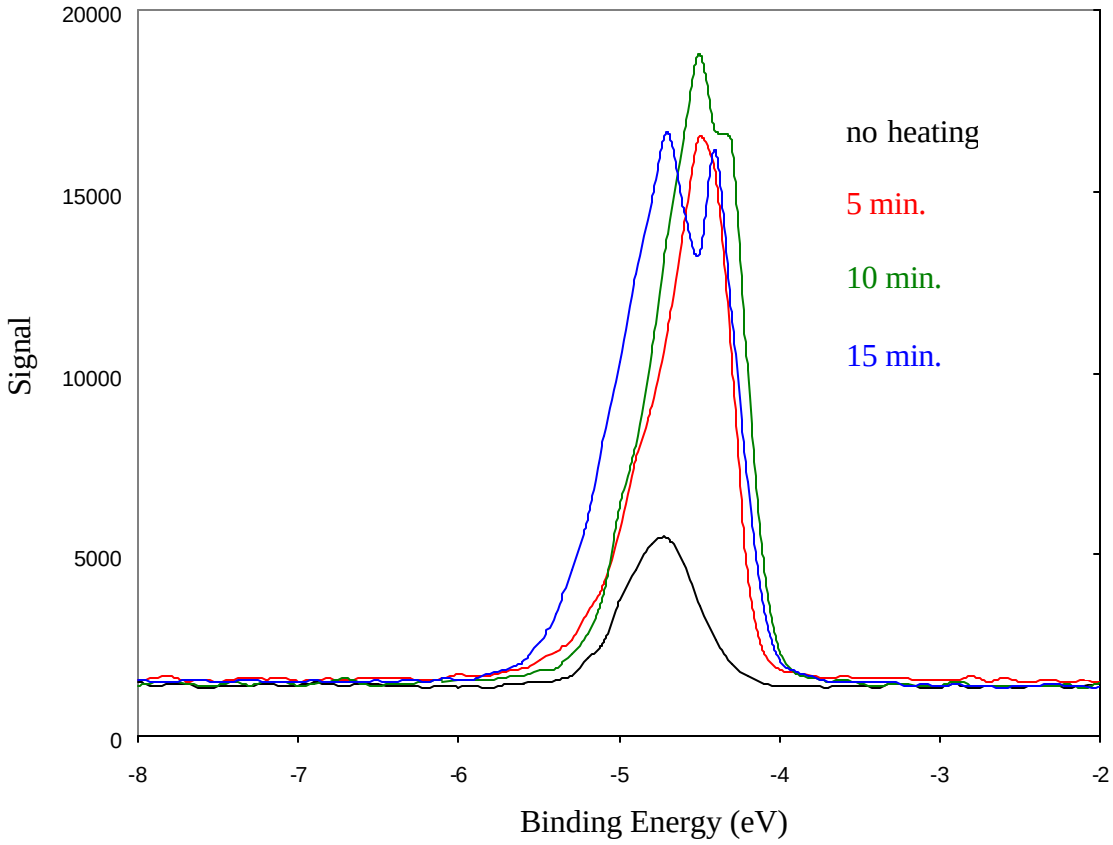

Figure 6.9 FEED curves on an Al tip heated to 125 °C for various time intervals. The separation of the energy distribution into two distinct peaks indicates the thermal cleaning of the tip.

resulting data are listed in table 6.2. The data suggests that this temperature is enough to thermally clean the Al tip. However, the data did not show the presence of the low work oxide as was observed in the previous section. In any case it is clear that aluminum can be somewhat cleaned at much lower temperature.

Low energy UPS was run on an Al flat sample at a temperature of 125 °C. The sample was heated at this temperature for a time period of 1 hour. XPS and UPS were done on the same sample before and after heating. The spectra are presented in figures 6.9 and 6.10 for both the UPS and XPS analysis and the fitting results are presented in table 6.2. The XPS results indicate that the sample becomes oxidized (p_{H2O} increases from $8x10^{-10}$ to ~ $8x10^{-9}$ torr) slightly by the apparent shift in the spectra. The UPS data on the other hand supports the FEED data in that the percent contribution of the Al peak increases, thereby lowering the work function. The percentage of Al_2O_3 decreases while the peak at 5.02eV slightly increases. The FEED data indicates that the tip was initially cleaned and then re-oxidizes with continued heating. Taking this into account, along with the XPS and UPS results for the flat sample, it appears to suggest that Al may diffuse toward the surface. As the Al is initially heated the Al diffuse outward resulting in the single peak in the FEED data after 5 minutes of heating. The Al then re-oxidizes with continued heating, resulting in the increases of the oxide peaks in the FEED, XPS and UPS data. These heating experiments therefore indicate that Al can be cleaned with a low temperature anneal. However, its extreme reactivity towards oxygen causes it to be readily oxidized thereby never allowing a purely clean surface.

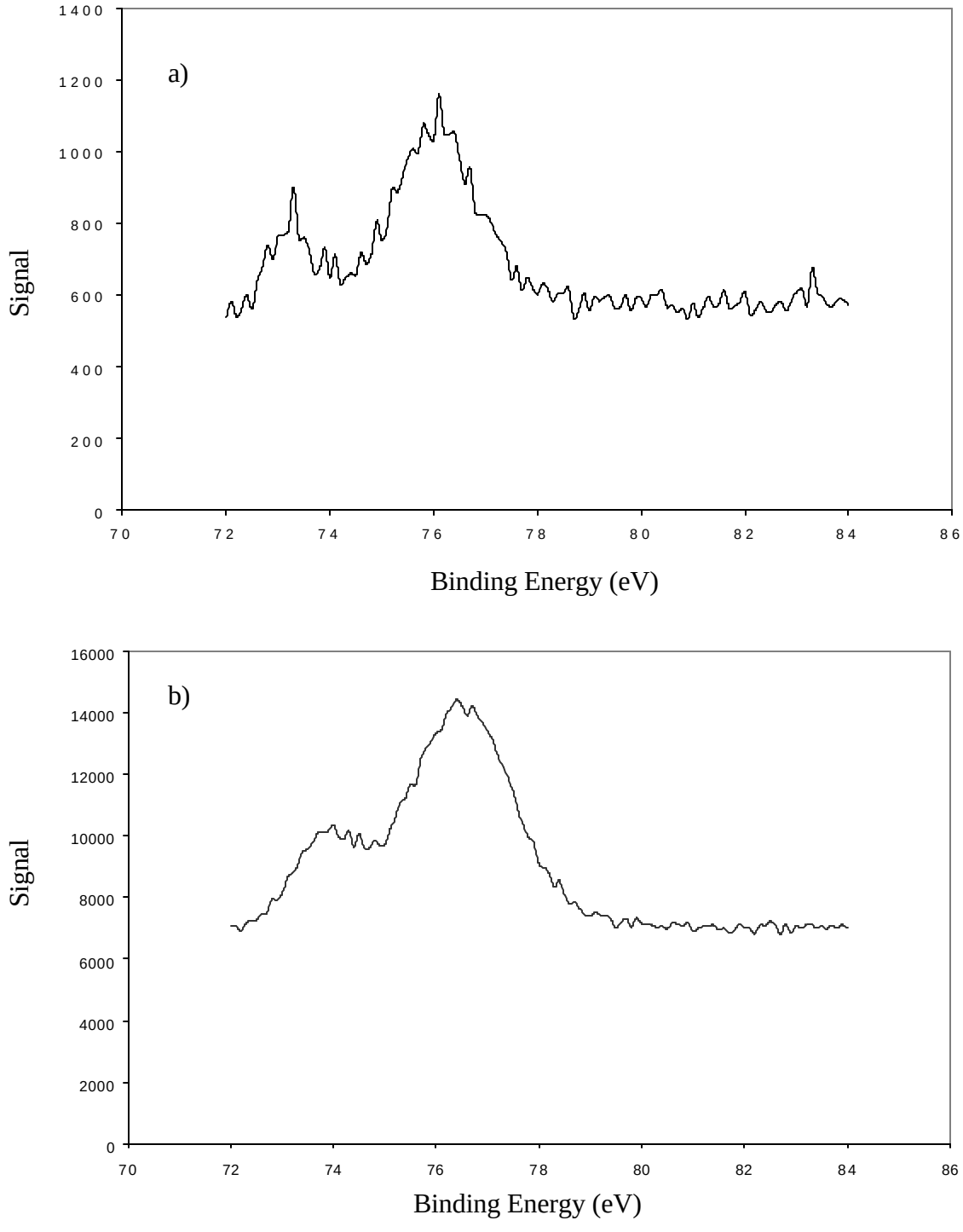

Figure 6.10 XPS of aluminum flat sample a) prior to heating and b) after heating in vacuum to 125 °C for 1 hour.

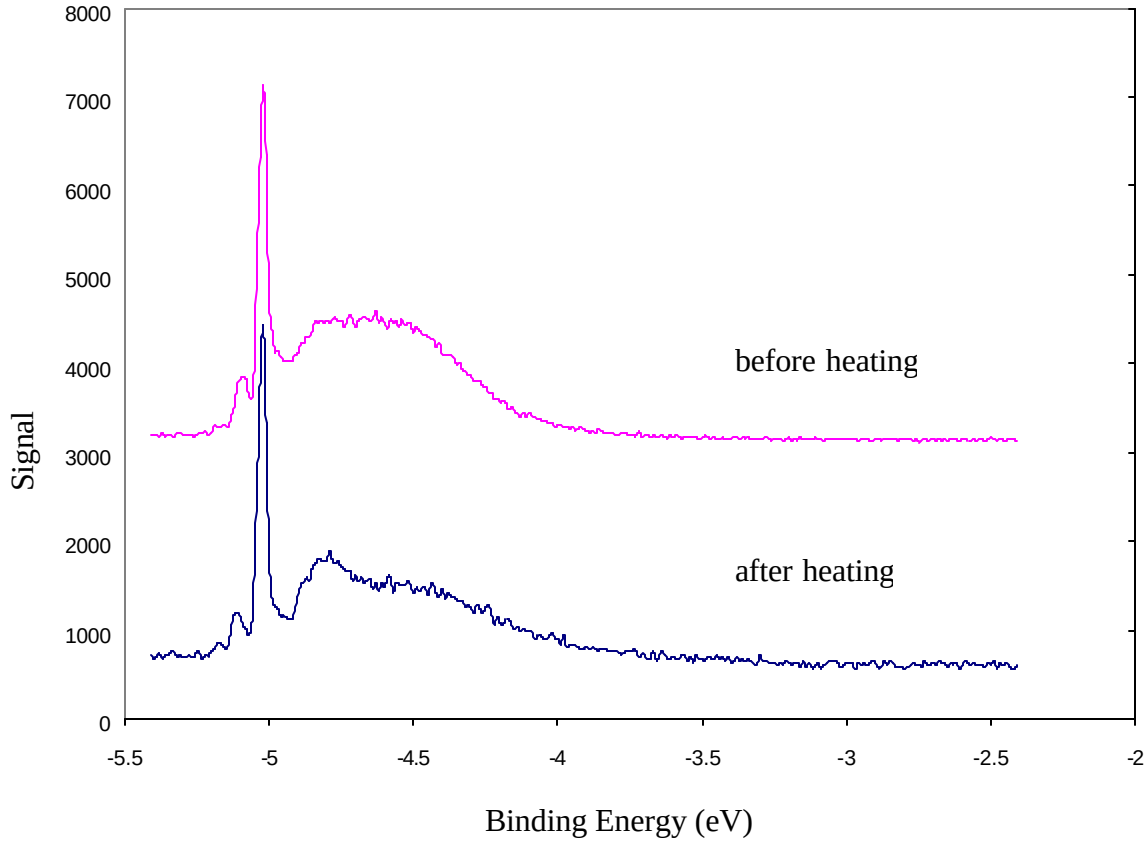

Figure 6.11 Low energy UPS of aluminum flat sample before and after heating to 125 °C for 1 hour.

FEED data of an Al tip heated to 125 °C

Time Duration	Peak Position (eV)		Percent Contribution	
(minutes)	peak 1	peak 2	peak 1	peak 2
0	-4.65	-	100	
5	-4.33	-	100	
10	-4.21	-4.48	55.2	44.8
15	-4.27	-4.66	43.8	56.2

XPS data of an Al flat sample heated to 125 °C

Condition	Peak Position (eV)			Percent Composition		
	peak 1	peak 2	peak 3	peak 1	peak 2	peak 3
prior to heating	73.3	75.5	76.2	20.7	26.8	52.5
heated 1 hour	73.8	76.2	76.7	19.9	31.6	48.5

UPS data of an Al flat sample heated to 125 °C

Condition	Peak Position (eV)					Percent Contribution				
	peak1	peak2	peak3	peak4	peak5	peak1	peak2	peak3	peak4	peak5
un-heated	-4.33	-4.57	-4.83	-5.02	-5.09	19.7	28.9	35.5	12.8	3.2
heated	-4.24	-4.55	-4.81	-5.02	-5.09	23.7	30.1	26.6	16.3	3.2

Table 6.2 FEED, XPS and UPS peak fit results for aluminum tip and flat samples heat to 125°C.

6.4 Conclusions

Field and photoemission studies have shown that aluminum is not a viable candidate for a field emitter material. Unlike Mo and carbon nanotubes a much larger anode voltage is required to achieve field emission most likely due to less effective etching. Even though aluminum readily oxidizes, field emission can still be achieved (it is however very erratic). Photoemission studies of sputtered and unsputtered aluminum samples have shown the possible existence of suboxides of aluminum with both higher and lower work functions. From the sputtering experiments the work function of these oxides appears to be coverage dependent. When the oxide film is thin (2-3 monolayers) the work function of aluminum is lowered as has been reported [2-4]. As for the assignment of the work functions to hydroxide or hydrate forms of oxides, more elaborate studies are required. The thermal experiments conducted indicate that aluminum can be cleaned by a low temperature anneal that most likely results from the diffusion of aluminum atoms to the surface. The aluminum atoms, however, readily re-oxidize. Unlike the Mo and carbon nanotube tips, the aluminum tips were not exposed to oxygen while in operation so their resiliency to oxygen was not determined.

References:

1. CRC Handbook of Chemistry and Physics 73rd edition, CRC Press Inc., 2000 Corporate Blvd., N.W., Boca Raton, FL 33431.
2. V.K. Agararwala, T. Fort Jr., Surf. Sci., **45**, 470 (1974).
3. T. Fort Jr., R.L.Wells, Surf. Sci., **32**, 543 (1972).
4. P. Vinet, T. Lemogne, H. Montes, NASA technical memorandum, **87079**, E-2657 (1985).
5. A. Barrie, Chem. Phys. Lett., **19**, 109 (1973).
6. J.A. Taylor, J. Vac. Sci. Technol., **20**, 751 (1982).
7. G. Faraci, S. La Rosa, A.R. Pennisi,Y. Hwu, G. Margaritondo, Phys. Rev. B, **47**, 4052 (1993).
8. V. Kottler, M.F. Gillies, A.E.T. Kuiper, J. Appl. Phys., **89**, 3301 (2001).
9. V.K. Agarwala, T. Fort Jr., Surface Sci., **48**, 527 (1975).
10. E.E. Huber Jr., C.T. Kirk Jr., Surf. Sci., **5**, 447 (1966).

CHAPTER 7

SUMMARY AND CONCLUSIONS

The field and photoemission characteristics of molybdenum, carbon nanotubes and aluminum have been studied using field emission electron spectroscopy, X-ray photoelectron spectroscopy and ultra-violet photoelectron spectroscopy. The studies presented showed that thermal annealing can change work function of these materials by changing the chemistry of the surface. The field emission stability of molybdenum and carbon nanotubes operated under the presence of O_2 was also investigated. FEED results showed that the stability of these emitter materials is strongly dependent on the current at which they are operated while exposed to O_2. Short term successful operation of the emitter in an oxygen environment can be accomplished only when the current is regulated.

XPS and UPS experiments conducted on molybdenum samples demonstrate that the oxides of molybdenum can only be removed when heated above 750 °C as stated in chapter 3. The limiting temperature at which an array device can be baked is not sufficient to accomplish cleaning of Mo microtips. In fact, at a temperature of 450 °C, the lower work function oxide, MoO_3, is reduced to MoO_2, which has a work function higher than Mo itself. FEED experiments show that even when these oxides are present the average work function of a single tip is close to that of Mo, whose work function

value is 4.6eV. FEED experiments were carried out for both clean and oxidized single microtips while operated in the presence of O_2. These experiments suggest that Mo emitter tips can be operated in O_2 without any substantial degradation in the field emission. This could only be accomplished when the Mo emitter tip was operated in the current range of 10pA to 1nA. Below this current range, the emitter tip was degraded due to oxidation of the tip. Above 1nA the degradation of the emission was the result of sputter ablation of the Mo tip. Between the currents of 10pA and 1nA the effects of sputtering counter the effects of oxidation. This was also apparent in an array when exposed to oxygen. When the array was operated with –90V on the cathode, as opposed to having the cathode grounded, the enhanced sputtering resulted in a lower amount of oxidation. Therefore, experiments conducted on Mo indicate that Mo emitters can be successfully operated even in the presence of oxygen in a narrow operating regime. Similar experiments were performed on carbon nanotubes. A comparison was made between single-walled nanotubes (SWNTs) purchased from two different vendors. In addition, a comparison between the field emission characteristics of multi-walled (MWNTs) and single-walled nanotubes was done. The XPS and UPS results on flat samples showed that at elevated temperatures the SWNTs become oxidized by the absorption of water into the nanotube cavity. It is believed that nanotube caps become opened at elevated temperatures allowing the uptake of H_2O. This uptake of water however, does not have an effect on the work function. FEED experiments suggested that SWNTs are not oxidized when field emitting in the presence on O_2. They do

however appear to be sputtered to some extent over the entire range of currents (2pA-5nA) at which they were operated. At 5nA the work function showed up to a 24% difference after 1000L O_2 exposure. Unlike the Mo tips operated at 5nA the SWNTs were not totally destroyed since emission was still observed. Field emission from MWNTs required a larger turn on voltage, which was likely due to their larger diameters. FEED experiments showed that MWNTs appear to have a larger work function. The work function derived from FEED gave a value of ~ 7.4eV as compared to 4.2eV for the SWNTs. This larger value was attributed to shifting of the FEED peak due to charging of the tip, which is a result of their high resistivity. SWNTs are therefore a better candidate for a field emission material since their geometry provides a low turn on voltage, yet they are susceptible to sputtering.

Field and photoemission experiments done on aluminum suggest that it is not a good candidate as a field emitting material. Thermal experiments showed that heating aluminum to 125 °C is sufficient to change the work function. This is may possibly be due to the diffusion of aluminum atoms through the oxide thereby exposing Al metal. This exposed metal readily re-oxidizes. Even though a thin oxide exists, field emission is still possible. XPS and UPS studies of sputtered and unsputtered aluminum samples have shown the possible existence of suboxides of aluminum with both higher and lower work function than that of pure aluminum. From the sputtering experiments the work function of these oxides appears to be coverage dependent, that is, when the oxide film is thin (2-3 monolayers) the work function is lowered as has been reported by others. We did not

determine these work functions are the result of hydrates or hydroxides of aluminum. Unlike the Mo and SWNTs the aluminum tips used in the field emission experiments were not exposed to oxygen while in operation, so their emission characteristics in the presence of oxygen was not determined.

BIBLIOGRAPHY

V.K. Agarwala, T. Fort Jr., Surf. Sci., **45**, 470 (1974).

V.K. Agarwala, T. Fort Jr., Surf. Sci., **48**, 527 (1975).

H. Ago, Th. Kugler, F. Cacialli, K. Petritsch, R.H. Friend, W.R. Salaneck, Y. Ono, T. Yamabe, K.Tanaka, Synthetic Metals, **103**, 2494 (1999).

I.A. Akwani, E.D. Sosa, J. Bernhard, S.C. Lim, R.E. Stallcup II, J.M. Perez, D.E. Golden, Mat. Res. Soc. Symp. Proc., **509**, (1998).

P. Arnoldy, J.C.M. de Jonge, J.A. Moulijn, J. Phys. Chem., **89,** 4517, (1985).

A. Barrie, Chem. Phys. Lett., **19**, 109 (1973).

E. Bauer, H. Poppa, Surf. Sci., **88**, 31 (1979).

J.M. Bernhard, PhD. Thesis, University of North Texas 1999.

J.M. Bernhard, A.A. Rouse, E.D.Sosa, B.E. Gnade, D.E. Golden, Rev. Sci. Instrum., **70**, 3299 (1999).

J.M. Bernhard, A.A. Rouse, E.D. Sosa, B.E. Gnade, D.E. Golden, B.R. Chalamala, S. Aggarwal, R. Ramesh, Flat Planel Display and Sensors- Principles, Materials and Processes Symposium (MRS Symposium Proceedings) vol. 588, pp. 85 (2000).

V.T. Binh, N. Garcia, S.T. Purcell, Advances in Imaging and Electron Physics, **95**, 74 (1996).

J.M. Bonard, J.P. Salvetat, T. Stockli, W.A. de Heer, L. Forro, A. Chatelain, Appl. Phys. A, **69**, 245 (1999).

D. Briggs, M.P. Seah, *Practical Surface Analysis*, John Wiley & Sons, Ltd., New York 1983.

I. Brodie, R. Schwoebel, Proceedings of the IEEE, **82**, 1006 (1994).

A. Cao, C. Xu. J. Liang, D. Wu, B. Wei, Chem. Phys. Lett., **344**, 13, (2001).

S.I. Castanñeda, I. Montero, J.M. Ripalda, N. Díaz, L. Galán, and F. Rueda, J. Appl. Phys., **85**, 8415 (1999).

B.R. Chalamala, R.M. Wallace, B.E.Gnade, J. Vac. Sci. Technol. B, **16**, 2859 (1998).

B.R. Chalamala, Thesis (PhD.), University of North Texas 1996.

L. Ci, B. Wei, C. Xu, J. Liang, d. Wu, S. Xie, W. Zhou, Y. Li, Z. Liu, D. Tang, J. Cryst. Growth, **233**, 823 (2001).

R.C. Cinti, E. Al. Khoury, B.K. Chakraverty, N.E. Christensen, Phys. Rev. B, **14**, 3296 (1976).

P.G. Collins, A. Zettl, Phys. Rev. B, **55**, 9391 (1997).

P.G. Collins, K. Bradley, M. Ishigami, A. Zettl, Science, **287**, 1801 (2001).

F.A. Cotton, G. Wilkinson, *Advanced Inorganic Chemistry 4th ed.*, John Wiley & Sons Inc., New York 1980.

CRC Handbook of Chemistry and Physics 73rd ed., CRC Press Inc., 2000 Corporate Blvd., N.W., Boca Raton, FL 33431.

K.A. Dean, B.R. Chalamala, Appl. Phys. Lett., **75**, 3017 (1999).

K.E Dean, P. von Allmen, B.R. Chalamala, J. Vac. Sci. Technol. B, **17**, 1959 (1999).

T.W. Ebbesen, H.J. Lezec, H. Hiura, J.W. Bennet, H.F. Ghaemi, T. Thio, Nature, **382**, 54 (1996).

A. Einstein, Annalen der Physik, **17**, 132 (1905).

G. Faraci, S. La Rosa, A.R. Pennisi, Y. Hwu, G. Margaritondo, Phys. Rew. B,**47**, 4052 (1993).

J.E. Fischer, H. Dai, A. Thess, R. Lee, N.M. Hanjani, D.L. Dehaas, R.E. Smalley, Phys. Rev. B, **55**, R4921 (1997).

T. Fort Jr., R.L. Wells, Surf. Sci., **32**, 543 (1972).

R.H. Fowler and L.W. Nordheim, Proc. Roy. Soc. London **A119**, 173 (1928).

M.J. Fransen, Th.L. van Rooy, P. Kruit, Appl. Surf. Sci., **146**, 312 (1999).

J.W. Gadzuk, E.W. Plummer, Rev. Modern Phys., **45**, 487 (1973).

O. Gröning, O.M.Küttel, Ch. Emmenegger, P. Gröning, L. Schlapbach, J. Vac. Sci. Technol. B, **18**, 665 (2000).

Y. Gotoh, K. Utsumi, M. Nagao, H. Tsuji, J. Ishikawa, T. Nakatani, T. Sakashita, K. Betsui, J.Vac. Sci. Technol. B, **17**, 604 (1999).

Yu. V. Gulyaev, N.I. Sinitsyn, G.V. Torgashov, Sh. T. Mevlyut, A.I. Zhbanov, Yu. F. Zakharchenko, Z.Ya. Kosakovskaya, L.A. Chernozatonskii, O.E. Glukhova, I.G. Torgashov, J. Vac. Sci. Technol. B, **15**, 422 (1996).

Handbook of X-ray Photoelectron Spectroscopy, Perkin-Elmer Corporation, Physical Electronics Division, Eden Prairie, MN 55344.

J.E. Henderson, R.E. Badley, Phys. Rev., **38**, 590 (1931).

E.E. Huber Jr., C.T. Kirk Jr., Surf. Sci., **5**, 447 (1966).

S. Itoh, T. Watanabe, K. Ohtsu, M, Taniguchi, S Uzawa, J. Vac. Sci. Technol. B, **13**, 487 (1995).

K. Jost, J. Phys., **E12**, 1006 (1979).

G.L. Kellogg, Colloque de Physique, **C8**, 297 (1989).

H.M. Kennett, A.E. Lee, Surf. Sci., **48**, 591 (1975).

V. Kottler, M.F. Gillies. A.E.T. Kuiper, J. Appl. Phys., **89**, 3301 (2001).

N. Kovtyukhova, E. Buzaneva, A. Senkevich, Carbon, **36**, 549 (1997).

O.M. Küttel, O. Groening, C. Emmenegger, L. Schlapbach, Appl. Phys. Lett., **73**, 2113 (1998).

C.E Kuyatt and J.A. Simpson, Rev. Sci. Instrum., **38**,1 (1967).

C. Lea, R. Gomer, J. Chem. Phys., **54**, 3349 (1979).

W.H. Lee, J.Y. Kim, Y.K. Ko, P.J. Reucroft, J.W. Zondlo, Appl. Surf. Sci., **141**, 107 (1999).

W.H. Lee, P.J. Reucroft, Carbon, **37**, 7 (1999).

W.H. Lee, S.J. Kim, W.J. Lee, R.C. Haddon, P.J. Reucroft, Appl. Surf. Sci., **181**, 121 (2001).

W.A. Mackie, R.L. Hartman, M.A. Anderson, P.R Davis, J. Vac. Sci. Technol. B, **12**, 722 (1994).

Materials and Electrochemical Research Corporation, Tuscon, AZ.

S. Meassick, H. Champaign, J. Vac. Sci. B, **14**, 1914 (1996).

A. Modinos, *Field, Thermionic and Secondary Electron Emission Spectroscopy*, Plenum Press, New York (1984).

O.R. Monteiro, V.P. Mammana, M.C. Salvadori, J.W. Ager III, S. Dimitrijevic, Appl. Phys. A, **71**, 121 (2000).

S. Morgren, R. Reifenberger, Surf. Sci., **254**, 169 (1991).

J. Muller, Surf. Sci., **69**, 708 (1977).

Operators Manuel Innova® 90C FreD™ Ion Laser, Coherent, Inc. Laser Group, 5100 Patrick Henry Drive, Santa Clara, CA 95054.

Peakfit, SPSS, Inc., 444 North Michigan Avenue, Chicago, IL 60611.

E.W. Plummer, J.W. Gadzuk, Phys. Rev. Lett. **25**, 1493 (1970).

E.W. Plummer, R.D. Young, Phys. Rev. B, **1**, 2088 (1970).

J. W Rabalais, R. J. Cotton, Chem. Phys. Lett., **29**, 131 (1974).

T.S. Ravi, R.B. Marcus, D. Liu, J. Vac. Sci. Technol. B, **9**, 2733 (1991).

L. Richter, R. Gomer, Surf. Sci., **83**, 93 (1973).

R. Riwan, C. Guillot, J. Piagne, Surf. Sci., **47**, 183 (1975).

A. A. Rouse, Thesis (PhD.), University of North Texas (1999).

A.A. Rouse, J.M. Bernhard, E.D. Sosa, D.E. Golden, Appl. Phys. Lett., 75, 3417 (1999).

A.A. Rouse, J.M. Bernhard, E.D. Sosa, D.E. Golden, Appl. Phys. Lett., **76**, 2583 (2000).

G.H. Smudde, Jr., P.C. Stair, Surf. Sci., **317**, 65 (1994).

P.A. Spevack, N.S. McIntyre, J. Phys. Chem., **69**, 9029 (1992).

C.A. Spindt, J. Appl. Phys., **39**, 3504 (1968).

C.A. Spindt, I. Brodie, Adv. Electron. Electron Phys., **83**, 1 (1992).

C.A. Spindt, I. Brodie, L. Humphrey, E.R. Westerberg, J. Appl. Phys., **47**, 5248 (1976).

C.A. Spindt, C.E. Holland, I. Brodie, IEEE Trans. Electron Devices, **38**, 2355 (1991).

Standford Research Systems, Inc., 1290-D Reamwood Ave., Sunnyvale, CA 94089.

L.W. Swanson, L.C. Crouser, Phys. Rev. Lett., **16**, 389 (1966).

J.A. Taylor, J. Vac. Sci. Technol., **20**, 751 (1982).

T. Utsumi, J. Soc. Infor. Disp.,**1/3**, 313 (1993).

VG ESCA Lab MK II Operation Manual, VG Scientific Limited, 1995.

P. Vinet, NASA Technical Memorandum, **87079**, E-2657 (1985).

S.L. Wang, Phys. Rev. Lett., **38**, 434 (1977).

N. Yao, V. Lordi, S.X.C Ma, E. Dujardin, A. Krishnan, M.M.J. Treacy, T.W. Ebbesen, J. Mater. Res., **13**, 2432 (1998).

Y.J. Yoon, D.S. Yoon, H.K. Baik, S.M. Lee, K.M. Song, S.J. Lee, J. Vac. Sci. Technol. B, **18**, 972 (2000).

R.D. Young, Phys. Rev., **113**, 110 (1959).

R.D. Young, E.W. Muller, Phys. Rev., **113**, 115 (1959).

U. Zielke, K.J. Küttinger, W.P. Hoffman, Carbon, **34**, 983 (1996).